U. S. ARMY

TRANSPORTATION RESEARCH COMMAND

FORT EUSTIS, VIRGINIA

TRECOM TECHNICAL REPORT 63-16

DETERMINATION OF OPTIMIZED PROPELLERS

FOR GROUND EFFECT MACHINES

Task 1D021701A04813
(Formerly Task 9R99-01-005-13)
Contract DA 44-177-TC-849

August 1963

prepared by:

KELLETT AIRCRAFT CORPORATION
Willow Grove, Pennsylvania

3497-63

DISCLAIMER NOTICE

The propeller will undoubtedly be the simplest means of imparting
energy to air in a GEM lift system. While such a system will be
limited to those vehicles having low base pressures, an increasing
number of military applications of low-base-pressure GEMs appear to
be feasible. The Army, therefore, undertook the development of a
method of predicting the performance of propellers in situations which
might be encountered in an air-cushion-vehicle lift system.

An experimental program was included to verify the analysis and
assumptions.

    FOR THE COMMANDER:

KENNETH B. ABEL
Capt   TC
Adjutant

Approved:

WILLIAM E. SICKLES
USATRECOM Project Engineer

Task 1D021701A04813
(Formerly Task 9R99-01-005-13)
Contract DA 44-177-TC-849
TCRECROM Technical Report 63-16
August 1963

DETERMINATION OF OPTIMIZED
PROPELLERS FOR GROUND EFFECT MACHINES

(Kellett Aircraft Corporation Report No. 208A90-5)

Prepared by

Kellett Aircraft Corporation
Willow Grove, Pennsylvania

for
U.S. ARMY TRANSPORTATION RESEARCH COMMAND
FORT EUSTIS, VIRGINIA

PREFACE

This report presents the results of a research program
to determine the methods of design of propellers for GEMs.
The work was performed under Contract DA 44-177-TC-849 during
the period of May 1962 to November 1962 at the Contractor's
facility located at Willow Grove, Pennsylvania. The assist-
ance of the U. S. Army Transportation Research Command (USATRECOM)
GEM task group in the execution of this program is gratefully
acknowledged. The Kellett Project Engineer was Mr. Nelson
Miller, Aerodynamicist. Notable contributions to the program
were made by Mr. Mario George, Aerodynamicist, and Mr. James
Guba, Test Engineer.

The technical guidance rendered by Mr. Richard Pruyn,
Manager of Research Engineering, led to the successful
completion of the program.

The authors of this report are Mr. N. J. Miller, Mr. M. M.
George, and Mr. R. R. Pruyn.

CONTENTS

ILLUSTRATIONS

x

LIST OF SYMBOLS

a Slope of lift curve, per degree

a_o Coning angle, degrees (see Figure 26)

b Number of propeller blades

C Propeller blade chord, feet

C_d Airfoil section drag coefficient, $C_d = \dfrac{D}{\rho q s}$

C_ℓ Airfoil section lift coefficient, $C_\ell = \dfrac{L}{\rho q s}$

$\dfrac{C_\ell^{3/2}}{C_d}$ Blade element efficiency parameter

$C_{m_{1/4}}$ Airfoil section pitching moment coefficient about the 25-percent chord

C_p Propeller power coefficient, $C_p = \dfrac{P}{S_P \rho (\Omega R)^3}$

C_T Propeller thrust coefficient, $C_T = \dfrac{T_P}{S_P \rho (\Omega R)^2}$

d Planform diameter, feet

D Airfoil drag, pounds

F Volume flow, cubic feet/second

$F_{c.F}$ Centrifugal force, pounds

h Nozzle height above ground, feet

h_y Blade element thickness (see Figure 27)

IHP Input shaft horsepower

k Inlet loss factor

k_2 Duct loss factor

L Total lift, pounds

M	Mach number
M_{oa}	Out of plane bending moment due to aerodynamic loading, foot-pounds
M_{oc}	Out of plane bending moment due to centrifugal loading
M_{IQ}	In-plane moments due to propeller torques, foot-pounds
M_{Ic}	In-plane moments due to centrifugal force, foot-pounds
$M_{T c/4}$	Torsional moment spanwise across the blade about the 25-percent chord, due to aerodynamic pitching moments, foot-pounds
$(M_T)_{THRUST}$	Torsional moment due to aerodynamic lift, foot-pounds
M_{TC}	Torsional moment due to centrifugal force, foot-pounds
P	Power, foot-pounds/second
p	Pressure, pounds/square foot
q	Dynamic pressure, pounds/square foot, $q = \dfrac{\rho V^2}{2}$
Q	Propeller torque, foot-pounds
r	Radial distance from center line of rotation, feet
R	Propeller radius, feet
S	Cross sectional area, square feet
$t_{\bullet}$	Nozzle thickness, feet
T_p	Propeller thrust, pounds
T_s	Inlet ring thrust, pounds

U	Resultant velocity perpendicular to blade-span axis at blade element, feet/second
V	Velocity, feet/second
W	Vehicle weight, pounds
X	Radial distance ratio, $X = r/R$
X_P	Ratio of propeller hub radius to propeller radius $(X_h = X_P)$
$\overline{y}_x$	Lateral distance from blade section centroids to the vertical protection of the root attachment centroid (see Figure 28)
$\overline{y}$	Lateral distance from centroid of the root attachment to the 25-percent chord
Z	Overall power factor - ratio of IHP to horsepower required for a ducted fan out of ground effect
z	Axial distance measured from propeller plane, feet (Positive downstream of propeller.)
$\overline{z}$	Vertical distance from blade section centroids to a reference plane through the root attachment (see Figure 26)
α	Angle of attack of blade element, degrees
$\delta_0, \delta_1, \delta_2$	Coefficients in power series expressing profile drag as a function of angle of attack
η_D	Duct efficiency, percent
η_i	Internal efficiency, percent
η_P	Isolated propeller efficiency, percent
η_x	Propeller blade section efficiency, percent
θ_0	Propeller blade pitch at root, degrees

Θ_p Propeller blade pitch, degrees

ρ Air mass density, slugs/cubic feet

σ Propeller solidity

ϕ Blade element inflow angle, degrees

ϕ_y Angle defined in Figure 27

Ω Propeller rotational speed

Subscript

t   Total pressure

j   Jet in nozzle

b   Base

①   Directly behind propeller plane

i   Inlet (in front of propeller)

p   Propeller plane

r_A Root attachment

x   Radial distance

y   In chord wise direction

NOTE

1.   Pressure terms referring to static pressure contain
     a single subscript, P_b, P_j, etc.

2.   Pressure terms referring to total pressure contain
     a double subscript in which t denotes total fol-
     lowed by the location subscript, P_{tj}, $P_{t①}$ etc.

3.   Terms which pertain to an area weighted average
     value are noted by a bar, $\bar{V}_j$, $\bar{P}_j$, etc.

SUMMARY

A theoretical analysis of the performance of a propeller-duct combination operating in ground effect was extended from the work conducted under Contract DA 44-177-TC-524, which was reported in Reference 1. A propeller was designed for optimum twist and taper and to provide a constant velocity across the GEM nozzle, thus producing a maximum lift-to-power ratio of the GEM in accordance with this reference. The optimum propeller design was of the same propeller solidity as a rectangular, non twisted blade propeller tested previously to obtain a direct comparison of performance. The method of analysis used to determine the performance, loads, and moments produced on a blade of arbitrary planform and twist operating in a duct is presented.

A test program was conducted to determine the effect of the optimized propeller on GEM performance. The duct nozzle area was also varied to determine the effect of this parameter on propeller optimization.

Propeller blade stall, along with large inlet losses which occurred during certain operating test conditions, resulted in performance which could not be accounted for in the analysis.

1

CONCLUSIONS

The thrust produced and power required by a propeller operating in a GEM can be predicted within 15-percent provided that the operating condition does not represent conditions for which the propeller is stalled or the inlet losses become large. The conditions for which the theory does not apply overlap the normal operating conditions of some GEMS, and therefore the development of the analysis should be continued to include these conditions.

The optimized propeller, which produced a uniform nozzle velocity, showed no improvement in GEM performance over the non twisted propeller which produced a triangular nozzle velocity distribution. The straight-bladed propeller tends to give better inlet performance. The internal efficiency of the straight-bladed propeller was 10-percent greater than the optimized propeller, for heights above h/d of 0.10. The optimized propeller produced higher power loadings and internal efficiencies than the non-twisted propeller below h/d of 0.10. This improvement is principally due to the greater resistance to stalling of the optimized propeller.

Duct efficiencies on the order of 75-percent were achieved for the straight duct for jet-to-total-base area ratios from 0.1 to 0.8. The duct efficiency is dependent upon the total pressure of the flow at the GEM nozzle. However, the duct loss factor, which depends upon dynamic pressure, increases with decreasing jet area. The duct losses are attributed to a large inlet loss.

The configuration in which the jet area was equal to 60-percent of the total base area produced the highest power loadings of the configurations tested. This configuration also showed the best performance for h/d greater than 0.1 based on the GEM power factor.

INTRODUCTION

This program was a continuation of the effort being directed toward the improvement of the internal efficiency of GEMs. The development of the GEM has demonstrated a need for simple, lightweight propellers and ducts which have adequate performance. However, there have been insufficient test data or analysis to evaluate duct and propeller designs. The effort presented in this report is directed toward providing a guide for designers in optimizing GEM propellers and duct systems.

Analysis was performed to develop methods of calculating the performance of an arbitrary GEM propeller as well as optimized propeller design. Experiments were conducted for comparison with the analytical treatment. The configuration tested consisted of a axially symmetric straight duct in which the jet area was varied by the addition of centerbodies of various diameters. Two propellers were tested in the duct: one propeller had a constant chord and zero twist, herein called the straight-bladed propeller; the other propeller tested represented the optimized propeller designed with twist and variable chord to produce a uniform axial velocity distribution with a minimum of losses.

This report is divided into four sections and three appendices. In Section 1, the development of propeller performance equations formulated during this program is presented along with the analysis for the determination of the performance of a propeller with an arbitrary planform and twist. Considerations for the design of an optimized propeller are discussed in Section 2. The results of the experimental program are presented in Section 3. A comparison of these results with theory is given in Section 4. The test program and a description of the instrumentation are presented in Appendix I. In Appendix II, an analysis for the determination of loads and moments produced on a twisted and tapered propeller blade operating in a duct is developed. The design of the optimized propeller used in this test program is given in Appendix III.

3

1. PROPELLER DESIGN

1.1 Development of Propeller Performance Equations

The following development represents a method of predicting propeller-in-duct performance for a propeller of arbitrary geometry at any operating condition. The process also results in a predicted axial velocity distribution. The development is a continuation of the work performed in Reference 1. The theory has also been modified to include:

a. An inlet energy loss factor
b. Airfoil section performance data, thereby including the effects of Mach number and a small amount of propeller stall.

It has been noted in the test data that the sum of the static pressure in the inlet and the dynamic pressure in the inlet is not zero. This indicates that there is an inlet energy loss. To account for this loss, an inlet energy loss factor was defined based on the inlet dynamic pressure. Some data are available on an inlet loss factor of this sort in the fan literature.

The modification to the theory which includes airfoil data only partially corrects the performance for stalling of the propeller. When there is a large amount of the propeller stalling, the flow breaks down and can flow back through the propeller plane. The theory can not predict performance for these conditions.

The modified theory is presented in the following sections.

1.1.1 Propeller Induced Velocity

The momentum theory states that the net force acting instantaneously on the fluid within a control volume is equal to the time rate of change of momentum within the control volume plus the excess of outgoing momentum flux over incoming momentum flux. Referring to Figure 1, the

4

control volume is drawn as follows: consider the zero streamline (q = 0) to form one boundary of the control volume. The next boundary follows the contour of the inlet ring and the duct walls. Finally, the remaining boundary is drawn at the exit plane of the GEM. The net forces acting on thes volume are the propeller and inlet ring forces, T_p and T_s, as well as the pressure force acting on the exit plane. The momentum theory gives the following equation:

$$T_s + T_P - \bar{P}_j S_j = \rho \bar{V}_j^2 S_j .$$ (1)

Similarly for an annular area increment,

$$dT_s + dT_P - P_j dS_j = \rho V_j^2 dS_j .$$ (2)

Equation (2) can be rewritten as

$$dT_P \left(1 + \frac{dT_s}{dT_P} \right) = \left(P_j + 2 q_j \right) 2 \pi R_j^2 dx_j x_j .$$ (3)

In order to express Equation (3) in terms of the parameters behind the propeller, denoted by ①, the assumption is made that the mass flow through any percentage area remains constant; that is,

$$V_① 2 \pi R_①^2 dx_① x_① = V_j 2 \pi R_j^2 dx_j x_j$$ (4)

or

$$\frac{x_j dx_j}{x_① dx_①} = \frac{1 - x_j^2}{1 - x_P^2} \quad \text{since} \quad \frac{V_①}{V_j} = \frac{S_j}{S_P} .$$ (5)

Substituting this into Equation (3),

$$\frac{dT_P}{dx} \left(1 + \frac{dT_s}{dT_P} \right) = \left(P_j + 2 q_j \right) \left(\frac{2 x}{1 - x_P^2} \right) S_j .$$ (6)

The continuity equation gives

$$q_j S_j^2 = q_① S_P^2 ,$$ (7)

and Bernoulli's equation gives

$$P_j + q_j = P_① + q_① .$$ (8)

5

Substituting Equations (7) and (8) into Equation (6) and solving for q_0,

$$q_0 = \left[\frac{dT_P}{dx} \frac{\left(1 + \frac{dT_s}{dT_P}\right)\left(1 - x_P^2\right)}{2 \times S_j} - P_0 \right]\left[\frac{1}{1 + \left(\frac{S_P}{S_j}\right)^2} \right] \tag{9}$$

since $q_0 = \frac{1}{2}\rho V_P^2$,

$$V_P = \left[\left(\frac{\frac{2}{\rho}\frac{dT_P}{dx}\left(1 - x_P^2\right)}{2 \times S_j\left[1 + \left(\frac{S_P}{S_j}\right)^2\right]} \right)\left(1 + \frac{dT_s}{dT_P} - \frac{P_0\, 2 \times S_j}{\frac{dT_P}{dx}\left(1 - x_P^2\right)}\right) \right]^{\frac{1}{2}} \tag{10}$$

or in non dimensional form,

$$\frac{V_P}{\Omega R} = \left[\frac{\left(1 - x_P^2\right)\frac{dC_T}{dx}\left(\frac{S_P}{S_j}\right)}{x\left[1 + \left(\frac{S_P}{S_j}\right)^2\right]}\left(1 + \frac{dT_s}{dT_P} - \frac{P_0\, 2 \times \left(\frac{S_j}{S_P}\right)\pi R^2}{\frac{dT_P}{dx}}\right) \right]^{\frac{1}{2}}. \tag{11}$$

The momentum theorem can now be applied to a control volume upstream of the propeller to give

$$dT_s = \left(P_i + 2q_i\right)dS_i \tag{12}$$

or

$$\left(\frac{dT_s}{dT_P}\right)dT_P = \left(P_i + 2q_i\right)\left(\frac{dS_i}{dS_P}\right)dS_P. \tag{13}$$

In order to account for inlet losses, it was found appropriate to define an inlet loss factor related to the inlet dynamic pressure as follows:

$$P_i + q_i - kq_i = 0. \tag{14}$$

Finally, the propeller thrust is determined, from a control volume enclosing the propeller, as

$$T_P = \left(P_0 - P_i\right)S_P. \tag{15}$$

Considering these relations along with the assumption that $\frac{dS_i}{dS_P} = \frac{S_i}{S_P}$ and $\frac{dT_s}{dT_P} = \frac{T_s}{T_P}$, Equation (13) gives the following relationship:

6

$$\frac{2\pi R^2 x P_{\Phi}}{\frac{dT_P}{dx}} = 1 + \frac{T_s}{T_P}\left(\frac{S_P}{S_i}\right)\left(\frac{k-1}{k+1}\right). \qquad (16)$$

Equation (16) can be substituted into Equation (11) to obtain

$$\frac{V_P}{\Omega R} = \left[\frac{\left(1-x_P^2\right)\frac{dC_T}{dx}\left(\frac{S_P}{S_j}\right)}{x\left[1+\left(\frac{S_P}{S_j}\right)^2\right]}\right]^{\frac{1}{2}} \left[1 + \frac{T_s}{T_P} - \frac{S_j}{S_P}\left(1 + \frac{T_s}{T_P}\left[\frac{S_P}{S_i}\right]\left[\frac{k-1}{k+1}\right]\right)\right]^{\frac{1}{2}}. \qquad (17)$$

For the case of $S_P = S_j = S_i$, Equation (17) reduces to

$$\frac{V_P}{\Omega R} = \left[\frac{\left(1-x_P^2\right)\frac{dC_T}{dx}}{2x}\right]^{\frac{1}{2}} \left[\frac{2\left(\frac{T_s}{T_P}\right)}{k+1}\right]^{\frac{1}{2}}. \qquad (18)$$

An evaluation of the inlet loss factor is given in Section 3.2.4.

1.1.2 Propeller Thrust Coefficient

Propeller thrust can be determined using the blade element theory. Referring to the following nomenclature diagram,

$$\alpha_x = \theta_x - \phi \qquad (19)$$
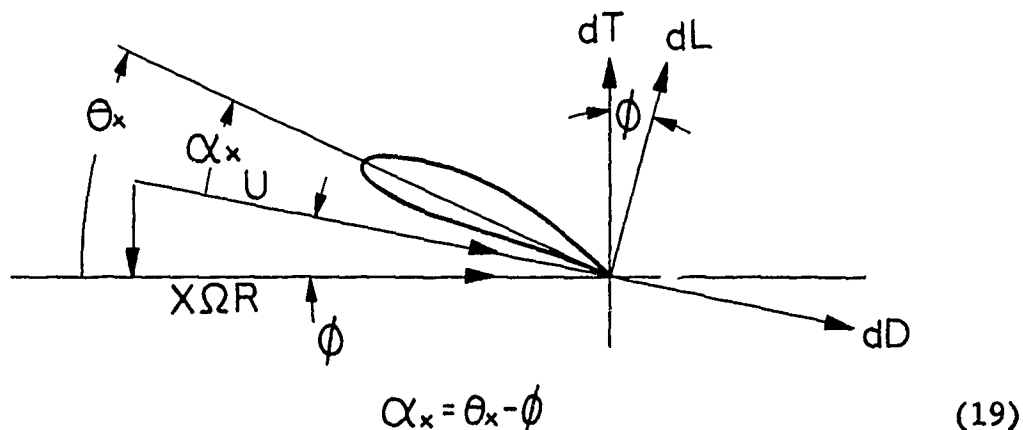
where

$$dT = dL \cos\phi - dD \sin\phi \qquad (20)$$

$$U^2 = V_P^2 + \left(X\Omega R\right)^2 \qquad (21)$$

$$\phi = \tan^{-1}\left(\frac{V_P}{X\Omega R}\right). \qquad (22)$$

Equation (20) can be rewritten as

$$\frac{dC_T}{dx} = \frac{\sigma_x}{2}\frac{X^2}{\left(1-X_P^2\right)}\left[\frac{1}{X^2}\left(\frac{V_P}{\Omega R}\right)^2+1\right]^{\frac{1}{2}}\left[C_l-C_d\left(\frac{V_P}{X\Omega R}\right)\right] \qquad (23)$$

and also

$$C_T = \int_{X=X_P}^{X=1}\frac{dC_T}{dx}\,dx. \qquad (24)$$

1.1.3 Propeller Power Coefficient

Propeller power can be written referring to the nomenclature diagram as follows:

$$dP = \Omega dQ \qquad (25)$$

or

$$dP = \Omega r\left(dD\cos\phi + dL\sin\phi\right). \qquad (26)$$

Similar to the development of propeller thrust coefficient, the power coefficient can be written as follows:

$$\frac{dC_P}{dx} = \frac{\sigma_x}{2}\frac{X^3}{\left(1-X_P^2\right)}\left[\frac{1}{X^2}\left(\frac{V}{\Omega R}\right)^2+1\right]^{\frac{1}{2}}\left[C_d+C_l\left(\frac{V_P}{X\Omega R}\right)\right] \qquad (27)$$

8

and
$$C_P = \int\limits_{X=X_P}^{x=1} \frac{dC_P}{dx}\, dx \cdot$$

(28)

1.2 Determination of the Performance of a Propeller of Arbitrary Planform and Twist

The following procedure can be used to determine the performance of an arbitrary propeller at any operating condition. Section 1.1 presents the propeller power and thrust coefficient performance equations along with the axial velocity prediction. The form of the equations presented is such that they can best be solved through the use of numerical integration across the span of the propeller. The numerical integration involves solving Equations (17), (23), and (27) at various positions on the blade span, then summing the result to obtain power, thrust, and velocity. This process can be carried out in tabular form. The equations can be set up in a column form and the summation process can be carried out. The procedure is as follows:

1.2.1 Select Radial Stations

Divide the propeller span into convenient radial stations for the calculation process. The number of radial stations required depends upon the accuracy desired. A minimum number of five radial stations was found to be adequate to obtain reliable results for this program.

1.2.2 Use Design Characteristics as Input Data

The following propeller parameters are to be obtained for use as input data:

Number of blades

Diameter

Chord (at each radial station)

9

Pitch (at each radial station)

Airfoil Section of blades

Propeller tip speed

A desired propeller r.p.m. is generally available. If
there is no specification for r.p.m., select a value.
The lowest r.p.m. which will produce the desired pressure
without blade stall generally results in the best per-
formance. As a first approximation, a value of r.p.m.
may be selected which will give a tip speed of 550 feet/
second.

1.2.3 Assume Axial Velocity Ratio, $V_p/\Omega R$

The performance equations developed in Section 1
require an iterative process for the solution of $V_p/\Omega R$ at
each radial station. This process begins with the assumption
of the axial velocity ratio at the first radial station
chosen closest to the propeller hub. It is suggested that
a value of 0.15 be chosen to keep the iteration process to
a minimum. This value was found to be a satisfactory
starting value for most conditions.

1.2.4 Calculate Local Inflow Angle, ϕ

The inflow angle can be calculated from
Equation (22),

$$\phi = \tan^{-1}\left(\frac{V_P}{X\Omega R}\right)$$

where x and $V_p/\Omega R$ are the values used in the previous steps.

1.2.5 Calculate Local Blade Angle of Attack, α_x

The angle of attack is given from Equation (19)
as

$$\alpha_x = \theta_x - \phi$$

10

where Θ_x is the local blade pitch.

1.2.6 Calculate Mach Number at Each Blade Radial Station, M_x

The Mach number at each radial station chosen from 1.2.1 can be calculated as

$$M_x = \frac{X \Omega R}{1120} \tag{29}$$

for standard atmospheric conditions.

1.2.7 Obtain Section Airfoil Lift and Drag Coefficients, C_l and C_d

Consult wind-tunnel data for the propeller airfoil sections. Lift and drag coefficients can be obtained from these data for the given angle of attack and Mach number.

1.2.8 Obtain the Value of the Ratio of Inlet Ring Thrust to Propeller Thrust, T_s/T_p

The value of T_s/T_p can be determined from Section 3.2.4.

1.2.9 Perform Iterative Digital Process

The information collected up to this point can now be used to calculate performance. The velocity ratio assumed in 1.2.3 and the resulting blade section lift coefficient are substituted into Equation (23) to obtain dC_T/dx at the blade hub station chosen in 1.2.1. This value of dC_T/dx is then substituted into the axial velocity Equation (17). The solution of Equation (17) represents the value of the calculated axial velocity ratio. This value is now compared with the assumed value of 1.2.3. If the values agree, continue to the next radial station and repent the process with 1.2.3; if the values do not agree, introduce the calculated value of $V_p/\Omega R$ from 1.2.9 into 1.2.3. This iterative process should continue until the difference

11

between the assumed value of $V_p/\Omega R$ and the calculated value is less than 0.001. After satisfying this requirement, continue to the next radial station and start with 1.2.3. This iterative process is continued until complete radial coverage of the propeller is reached, i.e., from $X = X_p$ to $X = 1.0$.

1.2.10 Calculate Propeller Thrust

Propeller thrust coefficient is obtained by adding the incremental thrust coefficients, dC_T/dx, obtained from 1.2.9 according to the equation,

$$C_T = \sum_{X=X_P}^{x=1} \frac{dC_T}{dx} \triangle x \qquad (30)$$

where

$\triangle X$ = non dimensional distance between each of the radial stations chosen.

The propeller thrust can be obtained as

$$T_P = C_T \, \rho \, (\Omega R)^2 \, S_P \cdot \qquad (31)$$

1.2.11 Calculate Propeller Power

Propeller power coefficient is obtained through calculation of Equation (27), dC_p/dx, and numerically integrating these values according to the following equation:

$$C_P = \sum_{X=X_P}^{x=1} \frac{dC_P}{dx} \triangle x \cdot \qquad (32)$$

12

The propeller shaft horsepower is given as

$$SHP = \frac{C_P \rho (\Omega R)^3 S_P}{550} .$$

(33)

1.2.12 Calculate Propeller Axial Velocity Distribution

The results of 1.2.9 give the exial velocity ratio at each radial station. The velocity distribution can be obtained by multiplying the axial velocity ratio by the propeller tip speed, ΩR.

13

2. DEVELOPMENT OF AN OPTIMIZED PROPELLER

2.1 Propeller Optimization

2.1.1 General Considerations

There are three general considerations to be made in the optimizing of a propeller for a GEM. These considerations are:

a. The propeller should produce the required air power for the least shaft power input.

b. The propeller should produce nearly uniform velocity at the jet nozzle of the GEM.

c. The propeller should be of the proper size to result in a minimum weight of the propeller, duct, and propeller drive system.

This type of propeller would lead to a GEM with the largest payload for a given mission.

2.1.2 Specific Considerations

The optimum propeller requirement for production of a given air power for the least shaft power input can be expressed as a propeller efficiency as follows:

$$\eta = \frac{\text{Air Horsepower}}{\text{Shaft Horsepower}} \cdot \qquad (34)$$

This can be related to the propeller since

$$\eta = \frac{T_p V_p}{550 \ \text{IHP}} \qquad (35)$$

14

or, in non dimensional form,

$$\eta = \frac{V_p}{\Omega R} \frac{C_T}{C_p} .$$

(36)

This efficiency can also be expressed as a propeller blade section efficiency as follows:

$$\eta_x = \frac{\left|\frac{V_P}{\Omega R}\right| x \frac{dC_T}{dx}}{\frac{dC_P}{dx}} .$$

(37)

If it is assumed that

$$C_d \left| V_P / X\Omega R \right| \lll C_\ell$$

$$\left(V_P / X\Omega R \right)^2 \lll 1.0$$

and $\qquad\qquad S_P = S_j = S_i$

then substituting Equations (18), (23), and (27) of Section 1.1 into Equation (37) of this section, it is found that

$$\eta_x = \frac{C_\ell}{C_d}^{\frac{3}{2}} \left[\frac{1}{\left[\frac{\sigma x}{2x} \left(\frac{T_s}{T_P(1+k)} \right) \right]^{\frac{1}{2}}} + \frac{C_\ell}{C_d}^{\frac{3}{2}} \right]$$

(38)

This equation indicates that if the ratio $C_\ell^{3/2}/C_d$, which will be defined as the airfoil section efficiency parameter, is increased, the propeller section efficiency will increase. This increase occurs in a fairly complicated manner, and therefore the following typical values were assumed to evaluate this relation:

15

$$\sigma_x = 0.22$$

$$x = 0.80$$

$$T_s/T_p = 0.20$$

$$k = -0.53$$

The blade section efficiency, calculated for various values of the airfoil section efficiency parameter, is shown in Figure 2. It should be noted from this figure that a small increase in efficiency results from a large increase in $C_\ell^{3/2}/C_d$ when this parameter is above a value of 40.

It may also be noted from the relation for blade section efficiency that the blade section solidity, σ_x and T_s/T_p, should be increased for an increase in efficiency. Also, the inlet loss factor, k should be small.

The optimum propeller requirement for production of uniform velocity to produce best GEM performance was not analyzed further in this program. However, it should be noted that the analysis presented in Reference 1 showed that GEM performance was not significantly reduced unless the velocity differed greatly from that which is uniform. This result was substantiated by the test program as noted later in this report. As a consequence it may be found that, in the evaluation of an optimum propeller, other considerations, such as weight or cost, may be more significant than the effect of producing a uniform velocity. These factors were not considered in this program.

To satisfy the requirement for a propeller, duct, and drive system of minimum weight requires a design study of the specific configuration. Therefore, it is not possible to generalize as to the size of the propeller. However, the requirement for compact ducting with small diffusion loss indicates that a propeller area of about the

16

same size as the GEM nozzle area is required. Also, the
propeller size which results in an adequate propeller tip
speed without a transmission between the engine and propeller
is attractive. On the other hand, large-area propellers
tend to occupy the usable space on the GEM. These consider-
ations are beyond the scope of the present program.

2.2 Optimized Propeller Design Procedure and Considerations

The design procedure for an optimized propeller is out-
lined in this section, along with information which is
believed to be pertinent to the design considerations. This
design procedure is enumerated in detail with the design of
the optimized propeller used in the test program as an
example in Appendix III.

It is to be noted that some of the procedures presented
in this section are interchangeable. That is, should one
part of the design of the propeller characteristics be
already established (for example, the propeller diameter),
it is possible to incorporate this design feature with the
remaining design steps.

The performance equations developed in Section 1.1 are
used for determining the characteristics of the optimized
propeller. Thus, the procedure is similar to the develop-
ment of Section 1.2, which presents the method of determin-
ing arbitrary propeller performance. As was mentioned in
Section 1.2, the form of the equations presented is such
that they can best be solved through the use of a numerical
integration across the span of the propeller.

The first part of the design procedure involves
obtaining an optimum blade airfoil section. An optimum
airfoil as described in Section 2.1 is one which produces
$C_l^{3/2}/C_d$ maximum for the expected operating conditions.
Thus, a study of airfoil data is required to reveal such an
airfoil. The angle of attack corresponding to $C_l^{3/2}/C_d$
maximum can then be obtained for the airfoil selected
at various Mach numbers.

17

Propeller tip speed, ΩR, is then chosen to insure operation compatible with Mach number and structural considerations. Propeller tip speed variation up to 600 f.p.s. was noted to have little effect upon performance and the optimization process. The lower limit to tip speed results from structural considerations and from the large coning angle which must be built into the propeller as explained in Appendix II. The high limit to practical tip speeds is caused by compressibility effects. For thin airfoil sections at low angles of attack, satisfactory performance can be achieved up to about 900 f.p.s. However, the range of tip speeds from 400 to 600 f.p.s. is recommended for initial design purposes.

The following area parameters are to be obtained:

a. <u>Propeller to inlet area ratio, S_P/S_i</u>

The effect of this parameter upon the optimization process was not studied during this program. It is believed, however, that an inlet area smaller than the propeller area would reduce inlet losses, since the smaller inlet area would tend to increase inlet dynamic pressure, thus preventing separation.

b. <u>Propeller to jet area ratio, S_P/S_j</u>

Tests indicated that the best GEM performance was obtained for the case in which the propeller area was equal to the jet area for the range of h/d from 0.05 to 0.30. Also, the smallest inlet losses occurred for the case in which $S_P/S_j = 1.0$

Propeller axial velocity can be obtained through the use of GEM design parameters as follows:

a. An intial design study will usually lead to such parameters as vehicle gross weight, size, and maximum operating height required.

18

b. The average base pressure required to support the given weight for this vehicle is

$$P_b = \frac{W}{S} . \qquad (39)$$

c. GEM nozzle geometry, such as jet area and inclination angle, is to be obtained. Reference 2 presents the effects of jet turning angle upon performance.

d. The ratio of base pressure to jet total pressure, P_b/P_{t_j}, and the ratio of the static pressure to the total pressure at the jet, P_j/P_{t_j}, can be obtained for the given nozzle geometry and operating height from various sources. In Reference 1, a compilation of some of the theoretical analysis along with test data is presented.

e. The jet velocity can be calculated from the given ratios as

$$q_j = P_{t_j} - P_j . \qquad (40)$$

This equation can be reduced in terms of the data previously obtained as

$$q_j = \frac{P_b}{\frac{P_b}{P_{t_j}}} - P_b \left(\frac{P_j}{P_{t_j}}\right)\left(\frac{P_{t_j}}{P_b}\right) \qquad (41)$$

and also

$$V_j = \sqrt{\frac{2}{\rho} q_j} . \qquad (42)$$

f. Propeller axial velocity can be calculated from the continuity equation as

19

$$V_P = V_j \left(\frac{S_j}{S_P} \right) .$$

(43)

The condition of constant propeller axial velocity ratio, $V_p/\Omega R$, can be imposed as a condition to solve the performance equations.

The local blade pitch as a function of blade radius (that is, the blade twist) can be determined by adding the optimum airfoil section angle of attack to the local inflow angle.

Thus

$$\Theta_P = |\alpha| \text{ optimum} + \phi$$

(44)

where

$$\phi = \tan^{-1} \left(\frac{V_P}{X\Omega R} \right) .$$

The local propeller solidity can be obtained through the elimination of dC_T/dx in Equation (17) through the use of Equation (23) to give

$$\sigma_x = \frac{2 \left(\dfrac{V_P}{\Omega R} \right)^2 \left[1 + \left(\dfrac{S_P}{S_j} \right)^2 \right]}{XC_\ell \dfrac{S_P}{S_j} \left[1 + \dfrac{T_s}{T_P} - \dfrac{S_j}{S_P} \left\{ 1 + \dfrac{T_s}{T_P} \left(\dfrac{S_P}{S_i} \right) \left(\dfrac{k-1}{k+1} \right) \right\} \right]}$$

(45)

where the values of T_s/T_p and K are discussed in Section 3.2.2.

The solidity, σ_x , varies as the product of the chord and number of blades for a fixed propeller diameter. Thus, when establishing the number of blades, consideration must be given to satisfying the solidity with practical values of the chord. This requirement is generally a structural problem. Aerodynamic efficiency usually will be slightly improved with

20

a larger number of blades. However, the advantages of having a minimum of blades are brought out in the simplicity of both hub and control design.

The number of blades is related to the local solidity and the local chord of the blades by the following relation:

$$C_x = \frac{\sigma_x \pi R}{b} .\qquad (46)$$

If it is found that the local chords of the propeller are such that the relation $\frac{2\pi r}{bc}$ is less than the value 2, cascade effects will be significant. These cascade effects influence the aerodynamic performance of the blade sections and may result in a poor prediction of performance. Cascade correction factors are presented in Reference 3, which appears to be applicable for these conditions.

3. TEST RESULTS

In this section the results of the test program are presented. The analysis has been utilized to isolate the performance components; however, the comparison of test results with predicted performance is presented in Section 4.

3.1 Propeller Performance

The thrust and power coefficients of a propeller define the performance of that propeller for given operating conditions. The thrust coefficient is a measure of the increase in pressure which the propeller causes. Since the air (or useful power) caused by the propeller is a function of the 3/2 power of the thrust coefficient, an expression for the propeller efficiency can be obtained from the performance coefficients. The propeller data obtained in this program are presented in this section. A comparison of these data with the analysis of Section 1 is presented in Section 4.

3.1.1 Propeller Efficiency

The propeller efficiency can be expressed as follows:

$$\eta_P = \left(\frac{C_T}{C_P}\right)^{\frac{3}{2}} \left(\frac{S_i}{S_P}\right) \sqrt{2\left(\frac{P_{tj}}{\frac{T_P}{S_P}}\right)\left(1 - \frac{P_j}{P_{tj}}\right)} \quad .$$

(47)

This relation can also be expressed as

$$\eta_P = \frac{C_T}{C_P}^{\frac{3}{2}} \sqrt{\frac{S_i}{S_P}\left(\frac{2\frac{T_s}{T_P}}{k+1}\right)} \quad .$$

(48)

Propeller efficiencies calculated with this relation are given in Figure 3 for the straight bladed propeller and for the optimized propeller at two pitch settings. Maximum efficiencies on the order of 80-percent are reached at $\frac{\pi d h}{S_j}$ of 1.75. It can be seen from this figure that the optimized propeller gave better performance

22

at low values of $\frac{\pi dh}{S_j}$, however, the straight-bladed propeller showed better values at $\frac{\pi dh}{S_j}$ larger than 0.70.

The performance of the optimized propeller with an increased pitch of 2 degrees ($\theta_0 = 19.4$ degrees) shows improvement at large values of $\frac{\pi dh}{S_j}$, at the expense of poorer performance at low $\frac{\pi dh}{S_j}$.

3.1.2 Thrust Coefficient

Propeller thrust coefficient data for the various jet area configurations are shown in Figure 4. The configuration with $\frac{S_j}{S}$ of 0.8 is seen to show the lowest C_T for the heights tested; also, the thrust coefficient is sensitive to small changes in height, while with S_j/S of 0.3, C_T is almost independent of $\frac{\pi dh}{S_j}$

3.1.3 Power Coefficient

Propeller power coefficient test data are shown in Figure 5 for the various jet area configurations tested. It may be noted that the variation of this parameter with height is similar to the thrust coefficient data in that power coefficient is independent of height for the small jet area configurations.

3.2 Duct Performance

The GEM duct system can be divided into two parts for the purpose of analysis. The first portion of the system in front of the propeller consists of an inlet ring and an inlet duct; the second part of the system contains the duct from the propeller to the exit nozzles. In this section, the performance of the complete duct system is considered and then the inlet performance is discussed separately.

3.2.1 Duct Efficiency and Loss Factor

The efficiency of the duct system of the GEM test

23

unit is defined to be the ratio of nozzle air power to the
air power produced by the propeller,

$$\eta_D = \frac{P_{tj} \, S_j \, V_j}{T_P V_P} \tag{49}$$

or, by use of the continuity equation, $S_j \, V_j = S_P V_P$,

$$\eta_D = \frac{P_{tj}}{\dfrac{T_P}{S_P}} \; . \tag{50}$$

The duct efficiency was calculated with the
measurement of total jet pressure, P_{t_j}, and propeller thrust,
T_p, according to Equation (50). Figure 6 gives η_D for various
configurations for the optimized and the straight-bladed
propeller. The average efficiency of 76-percent is seen to
be practically independent of configuration and nozzle height
for the optimized propeller. The duct efficiency with the
straight-bladed propeller is 4 to 6-percent higher than the
duct efficiency with the optimized propeller. This increased
efficiency is caused by the increase in the inlet efficiency.
The straight-bladed propeller produced a velocity distribution
which increased toward the blade tip. This increased velocity
near the duct wall prevented inlet ring flow separation, thus
increasing inlet efficiency and, hence, duct efficiency.

The efficiency of a duct system downstream of
the propeller can also be defined in terms of dynamic pres-
sure losses. A duct loss factor k_2 is defined by the follow-
ing relation:

$$P_0 + q_0 \left(1 - k_2 \right) = P_j + q_j \; . \tag{51}$$

The duct efficiency of Equation (49) can be expressed in terms
of the GEM nozzle static total pressure ratio with the use
of Equation (51) and the continuity equation as follows:

$$\eta_D = 1 + \frac{\dfrac{T_s}{T_P}}{1 + \left(1 - \dfrac{P_j}{P_{tj}}\right)\left(1 + k_2\right)\left(\dfrac{S_j}{S_P}\right)^2} \quad . \tag{52}$$

The parameter $\dfrac{T_s}{T_P}$ can be obtained from the data of Section 3.2.2 and the pressure data from Section 3.3. The duct loss factor, k_2, was calculated from Equation (52) for the various $\dfrac{S_j}{S_P}$ configurations tested and is shown in Figure 7.

The duct loss factor is shown to approach infinity as $\dfrac{\pi d h}{S_j}$ approaches zero. This is due to the fact that the jet static pressure becomes equal to the jet total pressure at zero height. The large values of the duct loss factor increasing with decreasing height and decreasing jet area are believed to be caused by the inlet losses.

3.2.2 Inlet Thrust and Inlet Loss Factor

Inlet thrust is produced by the negative static pressure acting on the inlet ring area. The magnitude of the inlet static pressure is dependent upon GEM height. This inlet thrust was determined through the use of measured surface static pressures and by use of strain gages as described in Appendix I.

The ratio of inlet ring thrust to propeller thrust for the straight-bladed and the optimized propeller is shown in Figure 8 as a function of $\dfrac{\pi d h}{S_j}$. The two propellers show a similar $\dfrac{T_s}{T_P}$ variation for values of $\dfrac{\pi d h}{S_j}$ below 3.0. The parameter S_j/S is seen to have a pronounced effect upon $\dfrac{T_s}{T_P}$.

As discussed in Section 1.1.1, an inlet loss factor can be defined as

$$P_i + q_i = k q_i \; . \tag{53}$$

25

The relation between inlet ring thrust and propeller thrust can thus be written in terms of duct pressures and the inlet loss factor as follows:

$$\frac{T_s}{T_P} = \frac{\dfrac{P_\Phi}{\dfrac{T_P}{S_P}} - 1 + k\left(1 + \dfrac{P_\Phi}{\dfrac{T_P}{S_P}}\right)}{(k-1)}$$

(54)

The loss factor, k, is available from the literature in some cases. Values of k were determined with the use of Equation (54) and from the test data. The inlet loss factor would be equal to zero for a 100-percent efficient inlet. Figure 9 presents the inlet loss factor for various jet-to-base-area ratios. It is seen from this figure that the factor approaches zero with increasing values of $\frac{S_j}{S}$. The larger jet-area configurations thus increase the inlet efficiency by increasing the GEM volume flow at the same $\frac{\pi\,d\,h}{S_j}$.

3.3 GEM Performance

One of the main topics of study in this program was the determination of the effect of the optimized propeller on GEM performance. It was noted from the analysis of Reference 1 that the uniform nozzle velocity caused by the optimum propeller would result in improved performance as compared with the straight bladed propeller. The GEM performance test data obtained with these two propellers are compared in the following discussion.

The effect on GEM performance of varying the ratio of the GEM nozzle (jet) area to the base area is also discussed in this section.

It should be noted that GEM performance (that is, lift and nozzle air power required) can be determined if P_b/P_{t_j} and P_j/P_{t_j} are known.

3.3.1 Base Pressure - Nozzle Total Pressure Ratio

The data obtained on the base pressure nozzle

26

total pressure ratio are shown in Figure 10. It may be noted in these data that there is no effect of the propeller configurations on these data. The effect of $\frac{S_j}{S}$ on this ratio at a given value of $\frac{\pi d h}{S_j}$ is small, but a slight increase in $\frac{P_b}{P_{tj}}$ may be noted for S_j/S of 0.8.

For comparison purposes, the test data of Reference 4 are also shown on Figure 10. The GEM tested in this reference had an S_j/S of 0.13 and a design nozzle inclination of 30 degrees. These data show a higher base pressure to nozzle pressure ratio than the configurations tested in this program due to the inclination of the nozzles.

3.3.2 Nozzle Static - Total Pressure Ratio

The ratio of jet static pressure to jet total pressure is shown in Figure 11 as a function of $\frac{\pi d h}{S_j}$. The curves show only slight variation with S_j/S.

3.4 Overall Performance of Propeller and GEM

The combined performance of the GEM with the propeller and duct system is discussed in this section. Performance data are presented in dimensional form as measured on the test unit. The internal efficiency of the unit, including propeller and duct efficiencies, is discussed. Overall performance of the unit as a GEM is presented in the form of the nondimensional power factor, Z.

3.4.1 Dimensional Performance Data

The performance of the GEM test unit is given as the total lift divided by input shaft horsepower, L/IHP, for various heights in Figure 12. Power loadings are shown for the straight-bladed propeller and for the optimized propeller with various nozzle configurations. The optimized propeller test data show a considerable increase in the pounds per horsepower for similar GEM lift-total area loadings, L/S, for a range of h/d from 0.010 to 0.10 over the straight-bladed propeller.

27

A power loading of 21.5 pounds/horsepower produced by the optimized propeller at an h/d of 0.02 is seen to be almost double that of the straight-bladed propeller. The improvement in performance due to the change in the propellers is due to an increased resistance to stalling of the optimized propeller.

Figure 12 also shows the effect of the nozzle area to total base area parameter, S_j/S, upon performance for the optimized propeller. Similar performance for S_j/S of 0.8 and 0.6 is noted for the range of h/d tested, while lower power loadings are noted for S_j/S of 0.3 and 0.10.

3.4.2 Internal Efficiency

The internal efficiency, defined as the ratio of nozzle air horsepower to input shaft horsepower expressed as a percentage, includes the efficiencies of the propeller and the duct. Figure 13 presents the internal efficiency for the straight-bladed propeller as well as for the optimized propeller for various duct configurations. The straight-bladed propeller shows higher internal efficiencies for h/d greater than 0.10, while the optimized propeller indicates improved performance for h/d less than 0.10. The internal efficiency decreases with decreasing jet area; however, it is noted that for the case of S_j/S equal to 0.6, the internal efficiency is higher for h/d greater than 0.15 than for the data obtained with S_j/S of 0.8. This slight improvement is due to the increased propeller efficiency at h/d greater than 0.15.

3.4.3 GEM Power Factor, $\bar{Z}$

In order to evaluate the effect of the propeller combination and the jet area relation on GEM performance, it is appropriate to define an overall power factor as the ratio of input shaft horsepower to the horsepower required by an ideal ducted fan hovering out of ground effect, with a disc loading equal to W/S, or in equation form,

$$Z = \frac{550 \text{ IHP}}{\frac{L}{2\sqrt{\rho}} \sqrt{\frac{L}{S}}} \quad . \tag{55}$$

28

This equation can also be expressed in terms of the measured
internal efficiencies of Section 3.4.2 and the calculated
volume flows as

$$Z = \frac{2P_{tj} F}{\dfrac{\eta_i \, L^{\frac{3}{2}}}{\sqrt{\rho s}}} \quad .$$

(56)

Figure 14 presents this factor as a function of the nozzle
height parameter for various values of S_j/S. It should be
noted that the GEM performance increases with decreasing
values of the overall power factor. The optimized propeller
shows improved performance over the straight-bladed propeller
for values of h/d less than 0.3. It is also noted that the
jet-base area ratio of 0.6 configuration shows increased
performance over jet-base area ratio of 0.8 configuration
for h/d values greater than 0.10.

4. COMPARISON OF PREDICTED PERFORMANCE WITH TEST RESULTS

In this section, the performance predicted by the analysis of Section 1 is compared to the test data presented in Section 3. An analysis of these results is made to determine why the theory does not give a better prediction of performance.

4.1 Thrust and Power Coefficients

predicted and experimental thrust and power coefficients are compared in Figures 15, 16, 17, and 18 for the four S_j configurations tested. These data show that the inlet loss theory of Section 1 gives a good prediction of the thrust coefficient and power coefficient for S_j/S of 0.8. The predicted power coefficient differs from the experimental values at low height; however, the prediction is within 12-percent of the experimental values, even at $\frac{\pi d h}{S_j}$ of 0.4. As shown in Figure 15, the inlet loss theory from Section 1 predicts the experimental data with more accuracy than the theory of Reference 1. The predicted power and thrust coefficient for the smaller jet area configurations are not in agreement with the experimental data as seen from Figures 16, 17, and 18.

The difference between experimental data and predicted values is due to the poor prediction of the propeller blade section angle of attack and blade stall effects, as will be discussed in the next section.

4.2 Propeller Section Angle of Attack

An estimate of the angle of attack of the propeller blades can be made by assuming that the velocity at the propeller is uniform. With this assumption, the nozzle flow data from Figures 6 and 11 were utilized to prepare estimated angles of attack at the root of the optimized propeller for various configurations. These data are compared with the angles of attack predicted by the inlet loss theory of Section 1 in Figure 19. The root angles of attack are shown since root stall occurs before blade tip stall,

30

due to the blade twist of the optimized propeller. Blade
stall angle of attack which was determined from the data
of Reference 6 occurs at the angle of attack at which the
lift curve fails to increase with an increase in angle of
attack. This angle was found to be 9 degrees. It may be
noted in Figure 19 that the root of the propeller blade
was stalled for S_j/S of 0.3 and 0.1 for all of the heights
tested. The theory predicted that there would not be stall
for these conditions. The accuracy of the prediction of
blade section angles of attack has been studied in more
detail, and the results are shown in Figures 20 and 21. The
radial distribution of angle of attack for S_j/S of 0.8 is
shown in Figure 20 for two heights. A very good prediction
of angle of attack is indicated by these data, especially
for the inlet loss theory. In Figure 21, similar data are
shown for the S_j/S of 0.6. It may be noted that due to
stalling, very large angles of attack were measured at the
root section of the blade at a $\frac{\pi d h}{S_j}$ of 0.34. The theory
predicted small angles of attack and no blade stall for
this condition.

REFERENCES

1. Pruyn, R. R., Perlmutter, A. A., Miller, N. J., On the Aerodynamic Design of Propellers and Duct Systems for Ground Effect Vehicles, Kellett Aircraft Corporation Report No. 208A90-1, Willow Grove, Pennsylvania, January 1962, ASTIA AD-274159.

2. Carmichael, B. H., et al, State of the Art Summary Air Cushion Vehicles, Aeronutronics Division of Ford Motor Company, Report No. U-926, Newport Beach, California, June 1960.

3. Cockshutt, E. P. and Galizzine, N., Powerplants For VTOL Aircraft. Appendix A, Theory of Wing - Immersed Fans for VTOL. National Research Council of Canada A.RLR-265, Ottawa, Canada, October 1959.

4. Anon., Results of Full Scale Air Flow Tests of the Gyrodyne Model 55 Annular Jet Type of Ground Effect Machine, Gyrodyne Company of America, Report No. X55-313310-2, St. James, Long Island, New York, June 1961.

5. Marks, L. S., Mechanical Engineers' Handbook, Mc'Graw Hill Book Company, Inc., New York City, New York, 1951.

6. Lindsey, W. F., Stevenson, D. B., Daley, B. N., Aerodynamic Characteristics of 24 NACA 16-Series Airfoils at Mach Numbers Between 0.3 and 0.8, NACA TN-1546, Washington, D. C., September 1948.

7. Jacobs, E. N., Ward, K. E., Pinkerton, R. M., The Characteristics of 78 Related Airfoil Sections From Tests in the Variable-Density Wind Tunnel, NACA TR-460, Washington, D. C., 1933.

8. Zimmerman, C. H., Characteristics of Clark Y Airfoils of Small Aspect Ratios, NACA TR 431, Washington, D.C., 1932.

9.   Pinkerton, R. M., Greenberg, H., <u>Aerodynamic Character-</u>
       <u>istics of a Large Number of Airfoils Tested in the</u>
       <u>Variable-Density Wind Tunnel</u>, NACA TR628, Washington,
       D.C., 1938.

APPENDIX I

THE TEST PROGRAM

1.0 SCOPE AND PURPOSE

The purpose of this program was to determine the
extent of applicability of the analysis of Reference 1
in the determination of an optimum propeller for Ground
Effect Machines. A propeller (herein referred to as the
optimized propeller) was designed using this analysis and
was tested at various GEM nozzle-to-ground heights and at
two propeller disc loadings. Additional tests were also
made with the straight-bladed propeller tested in Reference
1 to insure that the data obtained were comparable. The
optimized propeller was tested at two pitch settings. The
effect of the ratio of the base area to jet area upon the
optimization process was also investigated.

2.0 DESCRIPTION OF TEST APPARATUS

The GEM test device, shown in Figures 22 and 23, con-
sisted of a propeller and drive system, an inlet ring, a
duct, and a ground board. Instrumentation was provided to
measure GEM performance and flow parameters.

2.1 Propellers

The characteristics of the propellers tested in
this program are shown in Figures 24 and 25. The straight-
bladed propeller had a constant chord and a 0012 airfoil
section. The optimized propeller shown in Figure 25 was
twisted and tapered and had a 16-709 airfoil section.
Both propellers had four blades, were of wooden construc-
tion, and had a solidity of 0.22. As noted in Figure 25,
the optimized propeller was tested at root pitch settings
of 17.5 and 19.4 degrees.

34

2.2 Drive System

Power was delivered to the propeller by a hydraulic drive system which was driven by a 20-horsepower electric motor. The hydraulic drive permitted a wide range of adjustment of the propeller speed to produce the required propeller disc loadings.

Propeller thrust, r.p.m., and torque instrumentation were provided in the drive system.

2.3 Inlet Ring

The inlet ring had a semicircular cross section with a 2.25-inch radius, and an inside diameter of 2.90 feet to match the diameter of the duct system. This inlet is shown on the test device in Figures 22 and 23.

2.4 Duct System

The duct consisted of a circular straight duct 2.90 feet in diameter by 4.50 feet long, mounted concentric to various centerbodies which housed the drive unit. The centerbody was supported by four struts which were of 20-percent thickness and 13-inch chord, as shown in Figure 23. The exit nozzle area of the system was varied by changing the centerbody. Figure 23 shows the duct configuration for the four centerbodies tested. The parameters of the duct system are listed in Table 1.

2.5 Ground Board

A 9-foot-diameter disc was used to simulate the ground. This disc was suspended normal to the duct axis on three cantilever beam assemblies, permitting the measurement of differential axial force. Variation of the angles of pitch and roll as well as the distance from the duct exit plane was accomplished by means of screw adjustments. Tests were performed at duct exit heights ranging from 0.062 inch to 10 feet and with roll and pitch

angles of $\pm$ 10 degrees.

2.6 Instrumentation

2.6.1 Pressure Data

Pressure data were obtained at various stations throughout the test unit. Pressure probes and rakes sensed total and static pressure. The probes were connected by plastic tubing to four banks of multiple tube manometers. Pressure data were recorded at the following locations:

2.6.1.1 Inlet Ring

The axial distribution of static pressure along the inlet surface was measured at four azimuth positions of the inlet ring.

2.6.1.2 Duct Pressures

Static and total pressures were usually measured at four azimuthal and nine radial positions and at one station before the propeller and at two stations downstream of the propeller plane. Duct surface static pressures were measured along the duct wall and along the centerbody. During certain tests a calibrated pressure probe was used to obtain data concerning the propeller swirl angle.

2.6.1.3 Base Pressures

The radial variation of static pressure across one diameter of the bases of the center-bodies was measured.

2.6.1.4 Pressure Surveys

To supplement the duct pressure probes, pitot tube surveys were made in certain areas. In

particular, the flow pattern near the inlet and also near
the exit nozzle was studied at various azimuthal and radial
positions.

2.6.2 Performance Data

In addition to pressure data, the follow-
ing performance data were obtained:

2.6.2.1 Propeller Thrust

The propeller thrust was measured
with strain gages on a tension link attachment of the drive
shaft. A four-arm, temperature-compensated strain-gage
bridge circuit was utilized. The signal was fed through a
bridge balance and calibrating unit, and subsequently was
measured by a millivoltmeter.

2.6.2.2 Propeller Torque

The propeller torque was measured
using strain gages on a cantilever beam system mounted in
the drive shaft. A circuit similar to that of the propeller
thrust measuring device was used with the signal being
measured by a microammeter.

The propeller torque was also
obtained by using a calibrated hydraulic pressure gage
mounted on the drive unit.

2.6.2.3 Propeller Rotational Speed

A magnetic pickup which sensed the
passage of a propeller-shaft-mounted gear was used in re-
cording the propeller r.p.m. A stroboscope was also used to
obtain a second measurement of r.p.m.

2.6.2.4 Total GEM Lift

The ground board was instrumented
on the three flexures, mentioned previously, using strain-

gage bridge circuits similar to those used for propeller torque and thrust measurements. From the three reaction loads obtained, the total GEM lift and the center of pressure of lift were determined.

2.7 Evaluation of Test Results

In order to evaluate the performance of the GEM and propeller, certain parameters are needed. The following sections present methods of calculating some of the important parameters.

2.7.1 Performance Data

The following data were obtained directly from recorded data:

Propeller thrust, T_p, pounds
Total lift, L, pounds (Total ground board reaction)
Propeller speed, N, r.p.m.
Propeller torque, Q, foot-pounds

Utilizing the recorded data, the shaft horsepower was calculated as

$$IHP = \frac{QN}{5250} \cdot \tag{1}$$

Also, the power loading, L/IHP, was calculated.

2.7.2 Pressure Data

To present the pressure data in a more usable form, these data were evaluated by using the following relations:

2.7.2.1 Internal Efficiency, η_i

The internal efficiency is defined

as the ratio between the air horsepower at the duct exit, AHP, and the propeller shaft power input, IHP. That is,

$$\eta_i = \frac{AHP}{IHP} \, . \tag{2}$$

2.7.2.2 Duct Exit Air Power

The duct exit (or jet) air horsepower is defined by the following equation:

$$AHP = \frac{F_j \, P_{tj}}{550} \, . \tag{3}$$

Since F_j and P_{tj} vary locally over the duct exit, this calculation was accomplished by a numerical integration of the product of the area total pressure and velocity over the duct annulus at the nozzle. Total pressure was obtained directly from the pressure data at the nozzle. The local velocities were calculated from the static and total pressures using the Bernoulli equation.

$$q_j = P_{tj} - P_j = \tfrac{1}{2} \rho V_j^2 \tag{4}$$

Solving for velocity,

$$V_j = \sqrt{\frac{2}{\rho}\left(P_{tj} - P_j\right)} \, . \tag{5}$$

The resulting equation to be solved by numerical integration is

$$AHP = \frac{2\pi R^2}{550} \int_{x=x_H}^{x=1} \sqrt{\frac{2}{\rho}\left(P_{tj} - P_j\right)} \, P_{tj} \, x \, dx \, . \tag{6}$$

The air density, ρ, was corrected for duct temperature before use in this relation.

2.7.2.3 Volume Flow, F

Volume flow was calculated by performing a numerical integration of the velocity over the annular duct area,

$$F_j = \overline{V}_j A_j \cdot$$

(7)

Using Equation (5), the integral form of Equation (7) becomes

$$F = 2\pi R^2 \int_{x=x_H}^{x=1} \sqrt{\frac{2}{\rho}\left(P_{tj} - P_j\right)} \, x \, dx \cdot$$

(8)

2.7.2.4 Jet Momentum, T_j

The momentum of the jet is calculated by

$$T_j = m_j \overline{V}_j$$

(9)

where m_j is the mass flow at the jet is

$$m_j = \rho A_j \overline{V}_j \cdot$$

(10)

Using Equation (5) and the integral form of Equation (10), the jet momentum becomes

$$T_j = 4\pi R^2 \int_{x=x_H}^{x=1} \left(P_{tj} - P_j\right) x \, dx \cdot$$

(11)

Table 2 is a sample of the data reduction sheets which were used to calculate the efficiency, mass flow, and jet momentum for this program.

40

2.7.2.5 Augmentation Ratio, A

The augmentation ratio is defined as the total lift divided by the jet momentum,

$$A = \frac{L}{m\,V_j} \tag{12}$$

2.7.2.6 Inlet Ring Thrust, T_s

The inlet ring thrust was obtained by a numerical integration of the axial component of the static pressure times the cross-sectional area of the inlet ring. Thus,

$$T_s = 2\pi \int_{R_{s1}}^{R_{s2}} P_s\, r\, dr \tag{13}$$

where R_{s1} and R_{s2} are the inner and outer radii of the inlet ring respectively. The static pressures utilized for this calculation were the average of pressures measured at four azimuth positions on the ring.

This measurement of inlet ring thrust was checked by determining the loads on the three fixed-beam assemblies supporting the inlet ring. These data were found to agree with the pressure thrust measurement if the pressure in the seal between the duct and the inlet ring was included. Due to the additional complication of evaluating the pressure in the seal, the inlet thrust measurements presented in this report are from the inlet pressure measurements.

41

APPENDIX II

ANALYSIS OF THE LOADS AND MOMENTS ON A TWISTED AND

TAPERED PROPELLER BLADE OPERATING IN A DUCT WITH

AZIMUTHALLY UNIFORM FLOW

This appendix presents an analysis for the determination of loads and moments developed in a twisted, tapered, and cambered blade, as well as a sample calculation for the blade used in this program. It is assumed that this analysis is performed following the performance analysis discussed in Section 1.2 so that the distribution of the aerodynamic loading parameters with blade radius are available.

The forces and moments on the blade which are of principal interest are:

1. Centrifugal Force

The three orthogonal components of the force acting on the propeller blade which are parallel and perpendicular to the axis of rotation are called the thrust, the drag, and the centrifugal force. The thrust load is parallel to the axis of rotation and may be calculated by dividing the propeller thrust, T_p, obtained from the performance calculations by the number of blades. This thrust load will usually be small for GEM propellers. The drag force is very small and may be neglected for most designs. Centrifugal force is usually by far the largest of the forces on the propeller blade. This force is therefore required to determine the stress on the blade root and attachment.

2. Out-of-Plane Bending Moment

The out-of-plane moment due to aerodynamic loading can be balanced by coning the blades in the direction of the thrust. This causes a moment due to the centrifugal loading

42

which is in opposition to the aerodynamic moment. Proper
selection of the coning angle will result in a significant
reduction of blade root stresses.

3. In-Plane Moments

These are moments on the blade and root attach-
ment in the plane of rotation due to the torque required
and possibly due to a component of the centrifugal force.
Again, these moments may be in opposition and can be balanced
to reduce blade attachment stresses.

4. Torsional Moments

Blade torsional moments result from:

a. Airfoil section pitching moments.
b. Moment due to the location of the airfoil
     section aerodynamic centers.
c. Moment due to the component of centrifugal
     force which results from blade twist.
     (This moment is sometimes referred to as
     the tennis racket or the dumbbell effect.)

By proper location of the blade section aero-
dynamic centers, the torsional moment can also be made small.

When the loads and moments on the blade and the
root connection are established, standard stress analysis
procedures may be applied for material selection, determin-
ation of bolt sizes, retention fitting geometry, etc. These
considerations are not discussed in this section.

The notation used in this section is illustrated
in Figures 26 and 27.

1.0   ANALYSIS

The equations required to determine the significant
loads and moments on a GEM propeller blade are presented
in the following subsections. The methods used for
making the moments small are also given. It is assumed

43

that the blades are rigid for this analysis.

1.1 Centrifugal Force

The centrifugal force, F_{cF} , is given by

$$F_{cF} = \int_{r}^{R} \frac{dm}{dr} \, \Omega^2 r \, dr \tag{1}$$

$$F_{cF} = (\Omega R)^2 \int_{x=x_{r_A}}^{x=1} \frac{dm}{dr} \, x \, dx \tag{2}$$

where dm/dr is defined as the change in blade section mass with radius.

1.2 Out-Of-Plane Bending Moments

The out-of-plane bending moment is due to the aerodynamic loading and due to the centrifugal loading on the blades which are inclined at the coning angle, a_0 . The moment due to aerodynamic loading is

$$M_{OA} = \int_{R_H}^{R} r \, dT \tag{3}$$

or, in a form more suited for calculation,

$$M_{OA} = \frac{R A_P \rho (\Omega R)^2}{b} \int_{x_r}^{1} \frac{dC_T}{dx} \, x \, dx \, . \tag{4}$$

The moment due to centrifugal loading is

$$M_{OC} = \int_{R_H}^{R} \left(\frac{dm}{dr} \right) \Omega^2 r \bar{z} \, dr \tag{5}$$

44

where $\overline{Z}$ is the distance from the blade section centroids
to a plane which is perpendicular to the axis of rotation
and through the reference center of the root attachment.
If the variation of $\overline{Z}$ with blade radius is linear and the
resulting coning angle is small,

$$\overline{Z} = r a_0 \cdot \tag{6}$$

Substituting this relation into Equation (5) and writing
in terms of x,

$$M_{oc} = (\Omega R)^2 R a_0 \int_{xr}^{1} \left(\frac{dm}{dr}\right) x^2 dx \cdot \tag{7}$$

Equating the aerodynamic moment to the moment due
to centrifugal force, for zero banding at the root attach-
ment, the angle a can be found.

$$a_0 = \frac{S_P \rho \int_{xH}^{1} \frac{dC_T}{dx} x \, dx}{b \int_{xr_A}^{1} \frac{dm}{dr} x^2 dx} \tag{8}$$

If the variation of $\overline{Z}$ with r cannot be approximated
by Equation (6), the following iterative procedure should
be followed:

a. Select $\overline{Z}$ at the tip of the blade, $\overline{Z}t$.
b. Locate the blade section centroid at each
   radial station for the required pitch setting
   and twist angle in reference to $\overline{Z}t$.
c. Determine the distance from the blade section
   centroid to the plane of the root attachment.
d. The moment contribution of the centrifugal
   force on each blade section can then be
   determined. If the total flapping moment
   due to centrifugal force is found to differ
   from the aerodynamic moment, a new value
   of $\overline{Z}t$ is assumed and the calculation pro-
   cess is repeated.

45

1.3 In-Plane Moments

The in-plane moments on the blade are due to
propeller torque from aerodynamic loading and from the effect
of centrifugal force on the lateral offset of the blade
section centroids.

1.3.1 In-Plane Moment Due to Torque

The moment due to propeller torque acts
opposite to the direction of rotation and is calculated
as follows:

$$M_{IQ} = \frac{HP(550)}{\Omega} \, . \tag{9}$$

1.3.2 In-Plane Moment Due to Centrifugal Force

The component of the centrifugal force
acting in the plane of rotation causes a moment as follows:

$$M_{IC} = \int_{X=X_{rA}}^{X=1} \left(F_{CF} \right)_X \overline{y}_X \tag{10}$$

where $\overline{y}_X$ is the lateral distance from the blade section
centroids to the vertical projection of the root attach-
ment centroid.

1.4 Airfoil Pitching Moment

The torsional moments on the blade are evaluated
as follows:

1.4.1 Airfoil Pitching Moment

The pitching moment at the aerodynamic
center of the blade sections causes a blade torsion moment.

46

This moment can be evaluated from airfoil section test data. Airfoil section pitching moment data are usually presented in nondimensional form as $Cm_{\frac{c}{4}}$. Utilizing these data, the torsional moment spanwise across the blade about the 25-percent chord is

$$M_{T\frac{c}{4}} = R \int_{X=X_H}^{X=1} \left(Cm_{\frac{c}{4}}\right)_x q_x C_x^2 \, dx . \tag{11}$$

Substituting $\sigma_x = \dfrac{bC_x}{\pi R}$ into Equation (11),

$$M_{T\frac{c}{4}} = \frac{\pi^2 R^3}{b^2} \int_{X=X_H}^{X=1} \sigma_x^2 \left(Cm_{\frac{c}{4}}\right)_x q_x \, dx . \tag{12}$$

Then, substituting for

$$q_x = \frac{1}{2} \rho V_x^2$$

and

$$V_x = \left[V_P^2 + \left(\Omega R X\right)^2\right]^{\frac{1}{2}}$$

$$\frac{V_x}{\Omega R} = \left[\left(\frac{V_P}{\Omega R}\right)^2 + X^2\right]^{\frac{1}{2}} .$$

Equation (12) becomes

$$M_{T\frac{c}{4}} = \frac{\rho \pi^2 R^3 \left(\Omega^2 R^2\right)}{2 b^2} \int_{X=X_H}^{X=1} \sigma_x^2 \left(Cm_{\frac{c}{4}}\right)_x \left[\left(\frac{V_P}{\Omega R}\right)^2 + X^2\right] dx . \tag{13}$$

If the centroid of the root attachment is at any point other than the 25-percent chord, then the resulting torsional moment must also be considered;

47

$$\left(M_T\right)_{THRUST} = \frac{T}{b}\,\bar{y} \tag{14}$$

where $\bar{y}$ is the lateral distance from the centroid of the root attachment to the 25-percent chord.

1.4.2 Torsional Moment Due to Centrifugal Force and Blade Twist

Because of twist and taper, the centrifugal force acting through the centroids of each blade section generates a torsional moment.

The centrifugal force of element (dydr) is

$$dF_{cF} = d_e\,dx\,dr\,h_y\,\Omega^2\left(r^2 + y^2\right)^{\frac{1}{2}} \tag{15}$$

where de = Mass Density of Material.

The component of that force in the tangential direction is

$$dF_{cF} = \left[d_e\,dy\,dr\,h_y\,\Omega^2\left(r^2 + y^2\right)^{\frac{1}{2}}\right]\sin\phi_y \cdot \tag{16}$$

The torsional moment is the double integral of the sine component of this tangential force across the limits of the blade leading to trailing edges and root to tip respectively:

$$M_{TC} = \int_{r_{rA}}^{R}\int_{Yte}^{Yle} y\sin\phi_y\sin\theta_x\left[d_e\,dy\,dr\,h_y\,\Omega^2\left(r^2 + y^2\right)^{\frac{1}{2}}\right]\cdot \tag{17}$$

48

Substituting for $\sin\phi_y = \dfrac{y}{(r^2+y^2)^{\frac{1}{2}}}$ into Equation (17) and collecting terms,

$$M_{TC} = d_e \Omega^2 R \int_{x=x_{rA}}^{x=1} \int_{Y_{te}}^{Y_{le}} h_y y^2 \sin\theta_x \, dy \, dx \cdot$$

$$(18)$$

After solving for the loads and moments as indicated, one may apply standard stress analysis procedures for material selection, bolt sizes, retention fitting geometry, etc.

2.0   SAMPLE CALCULATIONS

This section presents the stress calculations used in the design of the optimum propeller.

The design conditions of the optimum blade are presented in Table 3. The blade chord and twist are given in Figure 25.

The blade tip speed, ΩR, varies with nozzle height and was obtained from performance calculations for 18 p.s.f. disc loading and

$$\Omega R = \sqrt{\frac{T_P}{S_P}\left(\frac{1}{C_T \rho}\right)} \cdot$$

$$(19)$$

For this analysis, however, we will consider a design condition of $h/d = 0.27$. This is the maximum height at which the test unit will operate for any length of time. The design values selected were for an h/d of 0.27 and $\Omega R = 552$ f.p.s., HP = 14.9 horsepower, D.L. = 18 p.s.f.

It may be seen from Figure 28 that the blade can be conveniently analyzed in two segments:

49

Segment I - Twist and Taper Airfoil Section from
$X=X_H$ to $X=1$.

Segment II - Tapered Root Section from $X = X_{ra}$ to $X = X_H$.

Numerical integrations were used in the solution of equations.
For this purpose, Segment I was divided into five equal sect-
ions as shown in Figure 28.

Figure 28 also indicates the sections of Segment II.
This segment is treated as a rectangular prism and two
triangular pyramids. The centroids of these sections are
located at radial locations X_a and X_b respectively.

2.1 Centrifugal Force

The numerical integration of Equation (1) is

$$F_{cF} = \left(\Omega R\right)^2 \sum_{X=X_{r_A}}^{x=1} x\left(\frac{\Delta m}{\Delta r}\right)_x \Delta x \cdot$$

(20)

By definition, $\frac{\Delta m}{\Delta r}$ = (Mass Density) (Cross-Sectional
Area), slugs/foot.

2.1.1 Centrifugal Force for Segment I

The cross-sectional area, S_x, for a given
airfoil is proportional to the square of the chord. There-
fore, for a blade with constant airfoil section, the area
at any station X may be written as

$$S_x = k_s C_x^2 \cdot$$

The area of a 16-709 airfoil section with a 10-inch chord
was determined with a planimeter to be 7.0 square inches.
Therefore,

$$k_s = \frac{S_x}{C_x^2}$$

$$= 0.07 \cdot$$

50

With the chord values of Figure 25, the area of airfoil
sections at each station was calculated, and the results
are summarized in Table 4.

From Reference 6, the density of white ash
= 42 pounds/cubic foot

$$\left(\frac{\Delta m}{\Delta r}\right)_x = \frac{42}{32.2}\left(S_x\right) = 1.304\,A_x$$

The calculated values for $\frac{\Delta m}{\Delta r}$ at each station are also

presented in Table 4.

From Table 4, $\displaystyle\sum_{x=x_H}^{1} \frac{\Delta m}{\Delta r} \times \Delta x = 0.00264$.

2.1.2 Centrifugal Force for Segment II

The following values are needed for the
rectangular prism portion:

$$x = \frac{4.9}{17.34} = 0.282$$

$$\Delta x = \frac{6.1}{17.34} = 0.352$$

$$\frac{\Delta m}{\Delta r} = 1.304\,S_x = 1.304\left(\frac{0.88}{12}\right)\left(\frac{3.0}{12}\right) = 0.0119\,\frac{slug}{ft.}\ .$$

For the triangular pyramid portions of Segment II,

$$x = \frac{6.8}{17.34} = 0.39$$

$$\Delta x = \frac{3.3}{17.34} = 0.19$$

$$\frac{\Delta m}{\Delta r} = 1.304\,S_x = 1.304\left(\frac{2}{3}\cdot\frac{0.88}{12}\right)\left(\frac{2}{3}\cdot\frac{1.03}{12}\right) = 0.0035\,\frac{slug}{ft.}\ .$$

51

The summation of $x \Delta x \dfrac{\Delta m}{\Delta r}$ for Segment

II is
$$\sum_{x=x_{rA}}^{x=x_H} x \Delta x \frac{\Delta m}{\Delta r} = 0.282(0.352)0.0119 + 2(0.39)(0.19)(0.0035)$$

$$= 0.00116 + 0.00052$$

$$= 0.00168$$

The total centrifugal force may now be calculated by substituting the above values into Equation (20):

$$F_{CF} = (552)^2 \left[0.00264 + 0.00168 \right]$$

$$= 1320 \text{ lb.}$$

2.2   Out-of-Plane Moment Due to Aerodynamic Loading

Equation (4) may be written as

$$M_{OA} = \frac{RS_P \rho (\Omega R)^2}{b} \sum_{x=x_H}^{x=1} \frac{\Delta C_T}{\Delta x} x \Delta x$$

obtaining $\dfrac{\Delta C_T}{\Delta x}$ from performance calculations.

From Table 4, $\displaystyle\sum_{x=x_H}^{x=1} \frac{\Delta C_T}{\Delta x} x \Delta x = 0.0187$

$$M_{OA} = \frac{1.445(5.21)(0.00238)(552)^2}{4} (0.0187)$$

$$= 25.5 \text{ ft.-lb.}$$

52

2.3 Blade Coning Angle for Zero Out-of-Plane Bending

Assuming the coning angle is small and rewriting
Equation (8),

$$a_0 = \frac{\frac{1}{b}A_p\rho\sum\limits_{x=x_H}^{x=1}\frac{\Delta C_T}{\Delta x}x\Delta x}{\sum\limits_{x_{rA}}^{x_H}\Delta x(x^2)\frac{\Delta m}{\Delta r} + \sum\limits_{x_H}^{1}x^2\Delta x\frac{\Delta m}{\Delta r}}$$

From Table 4,

$$\sum_{x_H}^{1}\frac{\Delta C_T}{\Delta x}x\Delta x = 0.0187$$

$$\sum_{x=x_H}^{x=1}x^2\Delta x\frac{\Delta m}{\Delta r} = 0.001676$$

From centrifugal force calculations,

$$\sum_{x=x_{rA}}^{x=x_H}\frac{\Delta m}{\Delta r}\Delta x x^2 = 0.0119 \cdot 0.35(0.28)^2 + 2(0.0035)(0.19)0.39^2$$

$$= 0.00035 + 0.000203$$

$$= 0.000528$$

$$a_0 = \frac{\frac{1}{4}(5.21)0.00238(0.0187)}{0.001676 + 0.000528}$$

$$= 0.263 \text{ rad.}$$

$$= 1.51 \text{ degrees} \cdot$$

53

With the above value for a_o , the distance, $\overline{Z}_x$, was obtained by using the method described in Section 1.2 of this appendix. The resulting moment due to centrifugal force was found to be in close agreement with the aerodynamic moment.

2.4 In-Plane Moment Due to Torque

As mentioned previously, the design maximum power required for this propeller, obtained from performance calculations, is 14.9 horsepower at a tip speed of 552 f.p.s.

Substituting these values into Equation (9),

$$M_{rq} = \frac{HP(550)}{\Omega}$$
$$= \frac{14.9(550)}{\frac{552}{1445}}$$

$$= 20.9 \, ft\text{-}lb. \text{ or per blade} \quad = 5.24 \, ft\text{-}lb.$$

Since the rotation is counterclockwise, the moment due to torque acts clockwise.

2.5 In-Plane Moment Due to Centrifugal Force

The only contribution to the in-plane moment is from Segment I, since Segment II is symmetrical about the root attachment centroid. The distance, $\overline{y}_x$, was

obtained by first determining the centroid of each blade section by the standard area moment method. The centroids for each blade section were found to lie on the airfoil mean line at the 50-percent chord. Values for $\overline{y}_x$ were

then measured from a layout of the blade and are presented in Table 4.

The contribution of each blade section can now be determined. Combining Equations (2) and (10) in a form for numerical integration,

54

$$M_{Ic} = (\Omega R)^2 \sum x \frac{\Delta m}{\Delta r} \Delta x \bar{y}_x \cdot$$

From Table 4,

$$\sum_{x=x_H}^{x=1} x \frac{\Delta m}{\Delta r} \Delta x \bar{y}_x = 0.0000245$$

for $\Omega R = 552$ ft./sec.

$$M_{Ic} = (552)^2 [0.0000245]$$

$$= 7.45 \text{ ft-lb.}$$

This moment acts counterclockwise, since centroids lie ahead of root attachment centroid projection (see Figure 26).

The residual in-plane moment is

$$M_{IQ} = 5.24 \text{ ft-lb} \quad CW$$

$$M_{Ic} = 7.45 \text{ ft-lb} \quad CCW$$

$$M_I = 2.21 \text{ ft-lb} \quad CCW$$

2.6 Torsional Moment

2.6.1 Torsional Moments Due to Airfoil Pitching Moment

Airfoil section pitching moment coefficients were obtained from Reference 6. The ratio of induced velocity to tip speed and the local solidity σ_x were obtained from performance calculations. These data are included in Table 4.

Equation (13) may be written as

$$M_{T\frac{c}{4}} = \frac{(\Omega R)^2 \rho \pi^2 R^3}{2 b^2} \sum_{x=x_H}^{x=1} \sigma_x{}^2 Cm_x \left[\left(\frac{V_P}{\Omega R}\right)^2 + x^2\right] \Delta x \cdot$$

From Table 4, $\displaystyle\sum_{x=x_H}^{x=1} \sigma_x{}^2 Cm_x \left[\left(\frac{V_P}{\Omega R}\right)^2 + x^2\right] \Delta x = -0.00180$

$$M_{T\frac{c}{4}} = \frac{(552)^2 0.00238 \pi^2 (1.445)^3}{2(4)^2} \left[-0.00180\right]$$

$$= -1.22 \text{ ft-lb.} \quad (\text{Nose Down}).$$

2.6.2 Torsional Moment Due to Aerodynamic Lift

For this blade, the centroid of the root attachment is not on the 25-percent chord; hence, a torsional moment arises from the aerodynamic lift.

From blade layout, $\overline{y}$ = 1.27 inches (scaled dimension).

From Equation (14),

$$(M_T)_{THRUST} = \frac{T_P}{b} \overline{y}$$

$$= \frac{93.8}{4} \times \frac{1.27}{12}$$

$$= 2.49 \text{ ft-lb.} \quad (\text{Nose Up}).$$

2.6.3 Torsional Moments Due to Centrifugal Force

2.6.3.1 Torsional Moment Due to Segment I

56

Since both airfoil thickness and length are functions of chord, the values of hy and y from Figure 27 can be written as percent of chord, and hence hy and y remain constant at any x value.

For numerical integration purposes, the airfoil section is assumed to be divided into five segments, each equal to 20-percent of the chord.

The root attachment centroid projection lies along the 50-percent-of-chord line at $x = x_H$. Values of y and hy are obtained from the airfoil ordinates and are also presented in the table below.

STA	$\dfrac{y}{C}$	$\dfrac{h_y}{C}$	$\dfrac{y^2 h}{C^3}$
1	0.4	0.03186	0.0051
2	0.20	0.08126	0.0032
3	0	0.0900	0
4	-0.20	0.07904	0.0031
5	-0.40	0.03776	0.0060

$$\frac{\Delta y}{C} = 0.20$$

$$\sum_{y=t_e}^{y=\ell_e} y^2 h_y \Delta y = 0.00348 \, C_x^4$$

The numerical integration form of Equation (18) for Segment I is

$$M_{TC} = d_e \, \Omega^2 R \sum_{y=t_e}^{y=\ell_e} y^2 h_y \Delta y \sum_{x=x_H}^{x=1} \sin \Theta_x \, \Delta x$$

$$M_{TC} = d_e \, \Omega^2 R \left[0.00348 \sum_{x=x_H}^{x=1} C_x^4 \sin \Theta_x \Delta x \right] .$$

57

From Table 4, $\displaystyle\sum_{X=X_H}^{x=1} C_x \sin\theta_x \, \triangle_x = -0.000986$

$$M_{TC} = 1.304(382)^2 1.445(0.00348)(-0.000986)$$

$$= -0.94 \text{ ft-lb.} \text{ (Nose Down).}$$

2.6.3.2 Torsional Moment Due to Segment II

The numerical equation form of Equation (18) for Segment II is

$$M_{TC} = d_e \Omega^2 R \sum_{y=t_e}^{y=\ell_e} \sum_{x=X_H}^{x=1} h_y \, y^2 \triangle y \triangle x \, \sin\theta_x$$

θ_x for this segment is constant

$$\text{Sin } \theta_x = -0.301.$$

Using the values for the rectangular prism and the triangular pyramid sections described in Section 2.1. and shown in Figure 32, the torsional moment is

$$M_{TC} = 1.304(382)^2(1.445)(-0.301)\left[2\left\langle \frac{0.88}{12}\left(\frac{0.75}{12}\right)^2\left(\frac{1.5}{12}\right)\middle|0.46-0.11\right\rangle\right.$$

$$\left.+2\left\langle\frac{2}{3}\left(\frac{0.88}{12}\right)\left(\frac{1.83}{12}\right)^2 \frac{2}{3}\left(\frac{1.0}{12}\right)\frac{2}{3}\middle|0.46-0.27\right\rangle\right]$$

$$= -8280\left[0.000025 + 0.000016\right]$$

$$= -0.34 \text{ ft-lb.} \text{ (Nose Down).}$$

2.6.4 Total Torsional Moments

Summing up torsional moments due to centrifugal force of Segments I and II,

$$M_{TC} = 1.28 \text{ foot-pounds (nose down).}$$

The total torsional moment acting on the root attachment fitting is the summation of

$$M_{TC} = M_{TC \frac{c}{4}} + M_{T_{THRUST}} + M_{TC}$$

$$= -1.22 + 2.49 - 1.28$$

$$M_T \cong 0 \text{ ft.-lb.}$$

3.0 <u>BLADE DESIGN LOADS</u>

In summation, the following results were obtained:

Centrifugal Force	1320 pounds
Out-of-Plane Moments	0 foot-pounds
Coning Angle, a_o	1 degree 30.5 minutes
In-Plane Moment	13.5 foot-pounds
Torsional Moment	0 foot-pounds

These loads were used to design the root attachment and hub of the optimized propeller tested in this program.

59

APPENDIX III

PROPELLER OPTIMIZATION PROCESS

AS APPLIED IN THIS PROGRAM TO THE OPTIMIZED PROPELLER

The following development has a twofold purpose: first, the design considerations and procedures for the propeller used in this program will be given; second, the procedure of Section 2.1 will be followed. Thus, this development can be used as an illustrative example.

It is noted that in some cases the design procedure used deviated from the design procedure of Section 2.1. This occurred since the design of the optimized propeller followed the work of Reference 1.

The diameter of the optimized propeller was made to fit the dimensions of the test duct facility. The local solidity of the optimum propeller was made the same as the straight-bladed propeller at the 0.8-blade radius for the purpose of comparison.

As a result of the work of Reference 1, there was an accumulation of propeller performance and GEM performance data obtained at various test conditions. In particular, some attention was focused at the case where $h/t_e = 1.00$ which represented an $h/d = 0.27$, and $\dfrac{\pi\, d\, h}{S_j} = 1.37$ for the case of $S_j/S = 0.80$. Thus, the newly designed propeller was optimized for operation at this height, With a reduced pitch setting, this propeller also operates at near optimum performance at lower heights.

Step 1: Optimum Airfoil Section Performance

It is necessary to select an airfoil with the best aerodynamic performance and to prepare the characteristics of the selected airfoil section in a form which can be used in the calculations. The procedures used to achieve these results are discussed below.

60

The aerodynamic characteristics of various airfoils were summarized, and a plot of $\dfrac{C_\ell^{\frac{3}{2}}}{C_d}$ versus section lift coefficient for these airfoils is shown in Figure 29.

The maximum value of $\dfrac{C_\ell^{\frac{3}{2}}}{C_d}$ is attained by the airfoil 16-709, and the values of $\dfrac{C_\ell^{\frac{3}{2}}}{C_d}$ on each side of the maximum value $\dfrac{C_\ell^{\frac{3}{2}}}{C_d}$ are seen to be higher than that of the other airfoils investigated. Thus, this airfoil would give the best efficiency of the airfoils investigated, as explained in Section 2.

The lower surface of the 16-709 airfoil is almost a straight line, which makes its fabrication simpler and less costly. This airfoil causes an aerodynamic pitching moment which must be accounted for in the stress calculations as explained in Appendix II.

The airfoil characteristics for the 16-709 airfoil are presented in Figure 30. These data are presented in the form $\dfrac{C_\ell^{\frac{3}{2}}}{C_d}$ and plotted against angle of attach for various Mach numbers in Figure 31. The angle of attack at which $\dfrac{C_\ell^{\frac{3}{2}}}{C_d}$ is a maximum was read from the curves of Figure 31 and was plotted against Mach number in Figure 32. This curve is used in the calculations.

Step 2: Propeller Tip Speed

As discussed in Section 1.2.2 of this report, a desired rotational speed is generally available. The nondimensional propeller performance parameters generally do not vary significantly for propeller tip speeds from 400 to 650 f.p.s., and therefore calculations based on any speed in this range will be almost identical. A propeller tip speed of 460 f.p.s. was used for the sample calculation.

61

Step 3: Obtain Propeller and Duct Geometry

The propeller for this program was optimized for a nozzle-area-to-propeller-area ratio, S_j/S_p, of unity. The propeller was assumed to be divided into the radial increments shown in Figure 28. The radial stations at the middle of these increments are listed in Table 5.

Step 4: Axial Velocity Ratio

As was previously mentioned, the propeller solidity of the optimized propeller is equal to the non-twisted propeller solidity at the 0.8 blade radius. Also, the optimized propeller is to produce uniform axial velocity, and therefore the axial velocity ratio will be constant with radius for this propeller. Thus, Equation (45) of Section 2.2 can be solved for the axial velocity ratio for the optimized propeller if the following assumptions are made:

a. The value of $\sqrt{1 + \left(\frac{V_P}{\Omega R X}\right)^2}$ is practically independent of $V_p/\Omega R$. That is,

$$\sqrt{1 + \left(\frac{V_P}{\Omega R X}\right)^2} \approx 1.$$

b. The product of the drag coefficient and the axial velocity ratio is very small as compared to the section lift coefficient. That is,

$$C_d \left(\frac{V_P}{\Omega R X}\right) \langle\langle C_\ell.$$

c. Inlet loss factor is zero. (No data on this factor were available at the time of this analysis. See Figure 9 for a better value for this factor.) With these assumptions,

62

$$\frac{V_P}{\Omega R} = \left(\frac{\sigma_x}{2} \times C_\ell \frac{T_s}{T_P} \right)^{\frac{1}{2}} .$$

To solve this equation, a value for Ts/Tp must be established. It was assumed that there would not be a significant influence of the propeller design on this parameter, and therefore the data obtained with the straight-bladed propeller shown in Figure 9 could be used for the optimized propeller design. As shown in this figure, this assumption was substantiated by the later testing. A value for Ts/Tp of 0.23 was used for the design.

The value for C_ℓ to be used in the equation for $V_p/\Omega R$ is the C_ℓ obtained at the optimum angle of attack. It is first necessary to calculate the section Mach number as

$$M_x = \frac{X \Omega R}{1120}$$

$$= \frac{0.8(460)}{1120}$$

$$= 0.32$$

Then from Figure 32 the optimum angle of attack of the 16-709 airfoil is 3.2 degrees. From Figure 30 the lift coefficient at this angle of attack is seen to be 0.81.

The axial velocity ratio can now be calculated as

$$\frac{V_P}{\Omega R} = \left(\frac{\sigma_x}{2} \times C_\ell \frac{T_s}{T_P} \right)^{\frac{1}{2}}$$

$$= \left(\frac{0.22}{2} (0.8)(0.81)0.23 \right)^{\frac{1}{2}}$$

$$= 0.127 .$$

63

This axial velocity is kept constant at all radial stations as shown in column 3 of Table 5.

Step 5: Blade Section Mach Number

The Mach number at each radial station can be calculated from the given tip speed of 460 f.p.s. as

$$M_x = \frac{x(460)}{1120}$$

and placed in column 4 of Table 5.

Step 6: Optimum Angle of Attack

The optimum angle of attack for each station can be read from Figure 32 for the calculated blade station Mach numbers and placed in column 6 of Table 5.

Step 7: Propeller Inflow Angle

Propeller inflow angle,   , can be calculated as

$$\phi = \tan^{-1}\left(\frac{V_P}{X \Omega R}\right)$$

and placed in column 7 of Table 5.

Step 8: Propeller Blade Pitch

The blade pitch can be obtained from

$$\theta_x = \alpha_{OPT} + \phi .$$

These data are shown in column 8 of Table 5.

Step 9: Airfoil Lift and Drag Coefficients

C_ℓ and C_d can be obtained from Figure 30 for the angles of attack of column 6 of Table 5 at the

64

Mach numbers of column 4. Columns 9 and 10 of this table present C_ℓ and C_d for these conditions.

Step 10: Solidity

For the case of $S_j = S_p$ and $k = 0$, Equation (45) reduces to

$$\frac{\sigma_x}{2} = \frac{\left(\dfrac{V_P}{\Omega R}\right)^2}{\dfrac{T_s}{T_F} C_\ell x} \cdot$$

The values obtained from previous steps are substituted into this equation and the results are shown in column 15 of Table 5.

Step 11: Propeller Thrust and Power Coefficient

The columns of Table 5 are set up according to Equation (23). Column 20 gives the incremental thrust coefficient. Adding this column and multiplying by the incremental span,

$$C_T = \sum \frac{\Delta C_T}{\Delta x} \Delta x$$

$$C_T = (0.324)(0.108) = 0.0350.$$

The thrust produced for this thrust coefficient is

$$T_P = C_T \rho S_P \left(\Omega R\right)^2$$

$$= 0.035(0.00238)(5.21)460^2$$

$$= 91.6 \text{ lb.}$$

Propeller power is calculated similarly to be

$$C_P = \sum \frac{\Delta C_P}{\Delta x} \Delta x$$

$$= 0.0454(0.108)$$

$$= 0.0049 .$$

The horsepower required for this coefficient is

$$SHP = \frac{C_P \rho (\Omega R)^3 S_P}{550}$$

$$= \frac{0.0049(0.00238)460^3(5.21)}{550}$$

$$= 10.7 \ hp .$$

As a result of this analysis, the propeller characteristics are designated. The characteristics of the optimized propeller are shown in Figure 25.

TABLE 1

GEM DUCT-TEST GEOMETRIC PARAMETERS

Total Base plus Jet   6.6   Square feet
     Cross-Sectional Area, S

Inlet Cross-Sectional   5.21   Square feet
     Flow Area, Si

Propeller Plane   5.21   Square feet
     Cross-Sectional Area, Sp

Exit Nozzle Area, Sj

     Configuration 1   5.21   Square feet

     Configuration 2   3.90   Square feet

     Configuration 3   2.00   Square feet

     Configuration 4   0.65   Square feet

Propeller Hub Radius to
     Propeller Tip Radius Ratio, $\dfrac{R_H}{R}$ 0.46

Length from Propeller Plane   4.42   feet
     to Duct Exit Plane, Z

TABLE 2

TYPICAL DATA REDUCTION SHEET

DATE 20 JUL 62	h/d = 0.15	η_i = 62.7 %
TEST NO. 97	2/ρ = 900	T_j = 26.50 lb
D.L. = 16	IHP = 8.70	F = 238.5 C.F.S.

								$\sum\eta_i$	$\sum T_j$	$\sum F$
$P_{T_j}-P_i$	P_{T_j}	X	ΔX	③×④	$\frac{2}{\rho}$①	$\sqrt{⑥}$	⑤×②	⑧×⑦	⑤×①	⑤×⑦
①	②	③	④	⑤	⑥	⑦	⑧	⑨	⑩	⑪
		0.46								
1.10	11.50		0.04	0.018	990	31.5	0.208	6.6	.0198	.567
		0.50								
2.00	12.30		0.10	0.05	1800	42.4	0.615	26.1	0.10	2.120
		0.60								
2.70	12.7		0.10	0.06	2430	49.3	0.762	37.6	0.162	2.948
		0.70								
3.00	12.7		0.10	0.07	2700	52.0	0.889	46.2	0.210	3.640
		0.80								
3.10	12.6		0.10	0.08	2790	52.8	1.008	53.2	0.248	4.224
		0.90								
3.0	12.3		0.10	0.09	2700	52.0	1.107	57.6	0.270	4.680
		1.00								
								227.3	1.0098	18.179
								.024$\sum$⑨	26.238$\sum$⑩	13.12$\sum$⑪

INTERNAL EFFICIENCY, $\eta_i = \dfrac{1}{IHP}\left[\dfrac{2\pi R^2}{550}\sum ⑨\right]$

VOLUME FLOW, $\qquad F = 2\pi R^2 \sum ⑪$

MOMENTUM, $\qquad T_j = 4\pi R^2 \sum ⑩$

TABLE 3

OPTIMIZED PROPELLER CHARACTERISTICS

Number of blades, b	4
Outer radius, R	1.445 feet
Hub Radius, R_H	0.665 feet
Centroid root attachment fitting, R_A	0.159 feet
Blade chord, c	function of radius
Blade pitch, Θ_b, (at X = 0.46)	17.50°, 19.4°
Blade twist, Θ_b,	function of radius
Maximum design propeller thrust, T_p	93.8 pounds
Maximum propeller disc loading T_p/S_p	18 p.s.f.
Design tip speed, ΩR	460 f.p.s.
Planform	tapered
Airfoil	NACA 16-709 series

TABLE 4

BLADE PARAMETERS FOR DETERMINATION OF BLADE STRESSES

(f)	X Stations ($\Delta x = 0.108$)					$\sum\limits_{x=x_H}^{x=1}(f)\Delta x$
	0.514	0.622	0.730	0.838	0.948	
$S_x(ft)^2$	0.00969	0.00671	0.00495	0.00377	0.00300	
σ_x	0.330	0.274	0.234	0.204	0.182	
$C_x(ft)$	0.372	0.309	0.266	0.232	0.207	
$\sin\theta_x$	-0.273	-0.234	-0.202	-0.173	-0.154	
$\bar{y}_x$	0.085	0.090	0.135	0.140	0.140	0.140
C_{m_x}	-0.103	-0.107	-0.110	-0.114	-0.118	
$\dfrac{\Delta m}{\Delta r}\left(\dfrac{slug}{ft}\right)$	0.0126	0.00875	0.00645	0.00492	0.00391	
$\dfrac{V_P}{\Omega R}$	0.145	0.145	0.145	0.145	0.145	
$(\Delta m/\Delta r)\,x$	0.00647	0.00544	0.00471	0.00412	0.00370	0.00264
$\Delta C_T/\Delta x$	0.0356	0.0404	0.0466	0.0610	0.0560	
$(\Delta C_T/\Delta x)\,x$	0.0183	0.0251	0.0340	0.0427	0.0530	0.0187
$(\Delta m/\Delta r)\,x^2$	0.00333	0.00260	0.00264	0.00345	0.00350	0.01676
$(\Delta m/\Delta r)\,x\bar{y}_x$	0.0000457	0.0000408	0.0000491	0.0000481	0.0000432	0.0000245
$\left[\left(\dfrac{V_P}{\Omega R}\right)^2+x^2\right]C_{m_x}\sigma_x$	-0.00314	-0.00323	-0.00332	-0.00341	-0.00357	-0.00180
$C_x^4\sin\theta_x$	-0.00519	-0.00215	-0.00101	-0.00050	-0.00028	-0.000986

70

TABLE 5

DIGITAL PROCESS FOR THE DETERMINATION OF PROPELLER THRUST AND POWER COEFFICIENT

① STATION	② RADIAL DISTANCE RATIO r/R	③ AXIAL VELOCITY RATIO $V_P/\Omega R$	④ M ⑤/1120	⑤ $(\frac{V_P}{\Omega R})\frac{1}{x}$	⑥ α_{OPT}	⑦ ϕ_x TAN^{-1}(⑤)	⑧ ϕ_x ⑥+⑦	⑨ C_l	⑩ C_d	⑪ ⑤²	⑫ $[1+⑪]^{\frac{1}{2}}$
I	0.514	0.127	0.22	0.247	3.7	13.39	17.59	0.810	0.0102	0.061	1.03
II	0.622	0.127	0.26	0.204	3.55	11.53	15.08	0.810	0.010	0.0416	1.02
III	0.730	0.127	0.30	0.174	3.40	9.88	13.28	0.810	0.0096	0.0302	1.015
IV	0.838	0.127	0.35	0.1515	3.20	8.62	11.82	0.810	0.0090	0.0229	1.011
V	0.946	0.127	0.39	0.1340	3.00	7.64	10.64	0.808	0.0085	0.0180	1.008

① STATION	⑬ ⑨×②×⑫	⑭ $\frac{T_s}{T_P}$ ⑬×④	⑮ $\frac{\sigma_x/2}{③²/④}$	⑯ $\frac{②²}{(1-X_P^2)}$	⑰ ⑩×⑤	⑱ ⑨-⑰	⑲ ⑮×⑯	⑳ $\frac{dC_T}{d\times j}$ ⑫×⑱×⑲
I	0.429	0.0985	0.1635	0.3358	0.0025	0.810	0.0548	0.0457
II	0.514	0.1179	0.1360	0.4918	0.0020	0.810	0.0668	0.0552
III	-	-	0.1168	0.6774	-	0.810	0.0790	0.0648
IV	-	-	0.102	0.8926	-	0.808	0.0910	0.0743
V	-	-	0.091	1.1376	-	-	0.1035	0.0841

FIGURE 1: NOTATION USED IN THE DETERMINATION OF
PROPELLER VELOCITY

$$\eta_x = \frac{C_l^{3/2}/C_d}{4.1 + C_l^{3/2}/C_d}$$
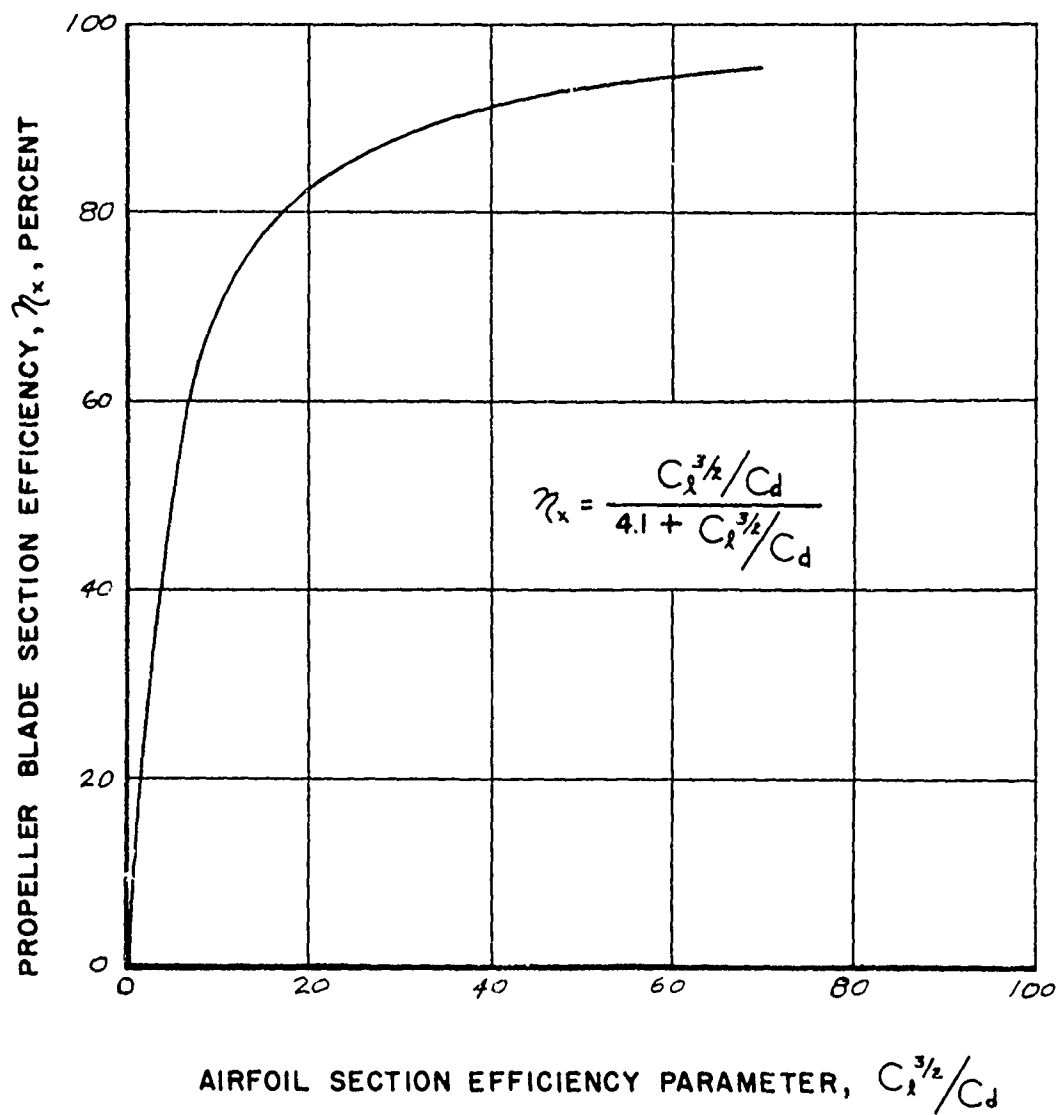
FIGURE 2: EFFECT OF THE AIRFOIL SECTION EFFICIENCY PARAMETER
ON BLADE SECTION EFFICIENCY

73
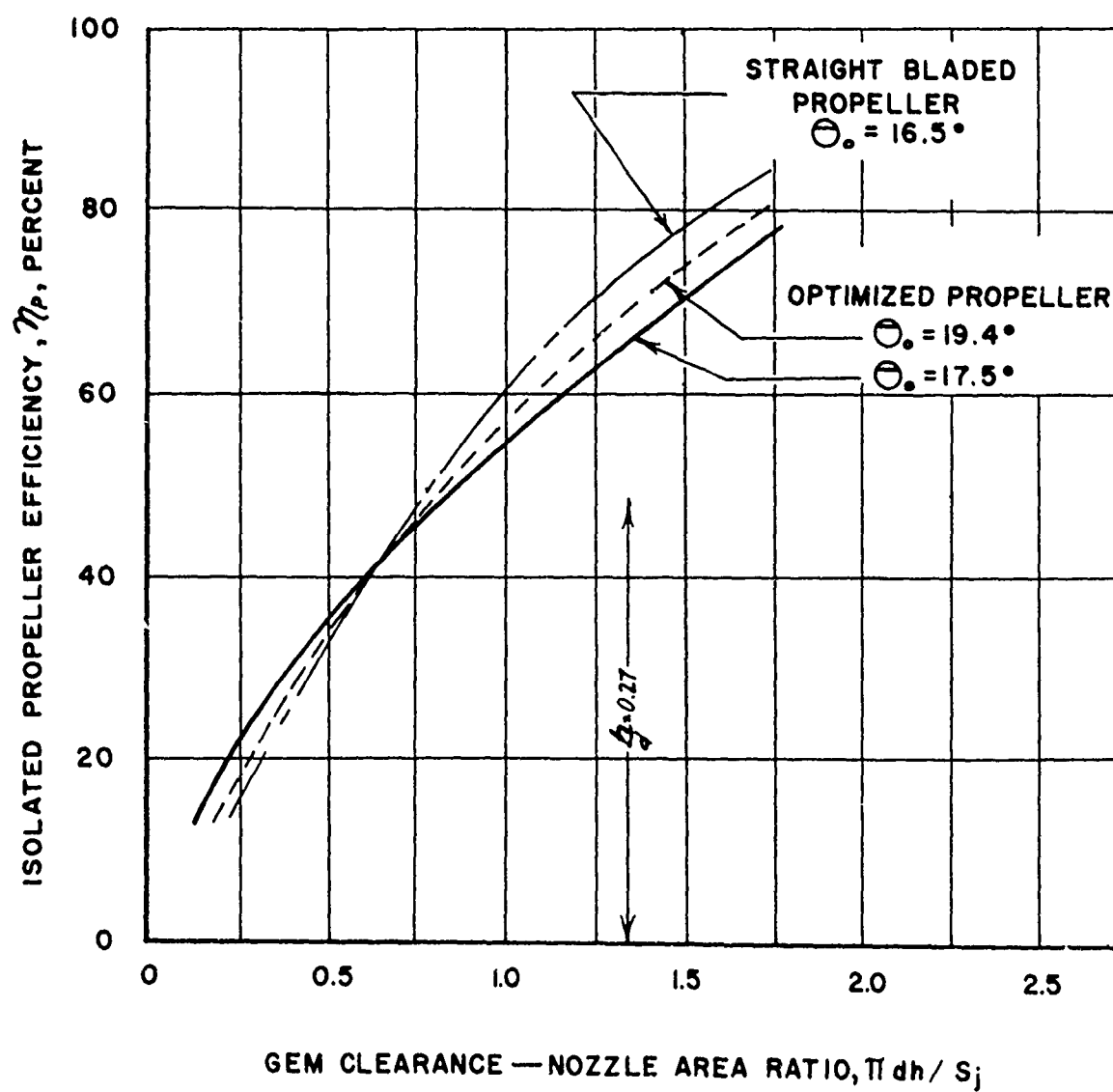
FIGURE 3:   ISOLATED PROPELLER EFFICIENCY BASED ON
NOZZLE PRESSURE DATA
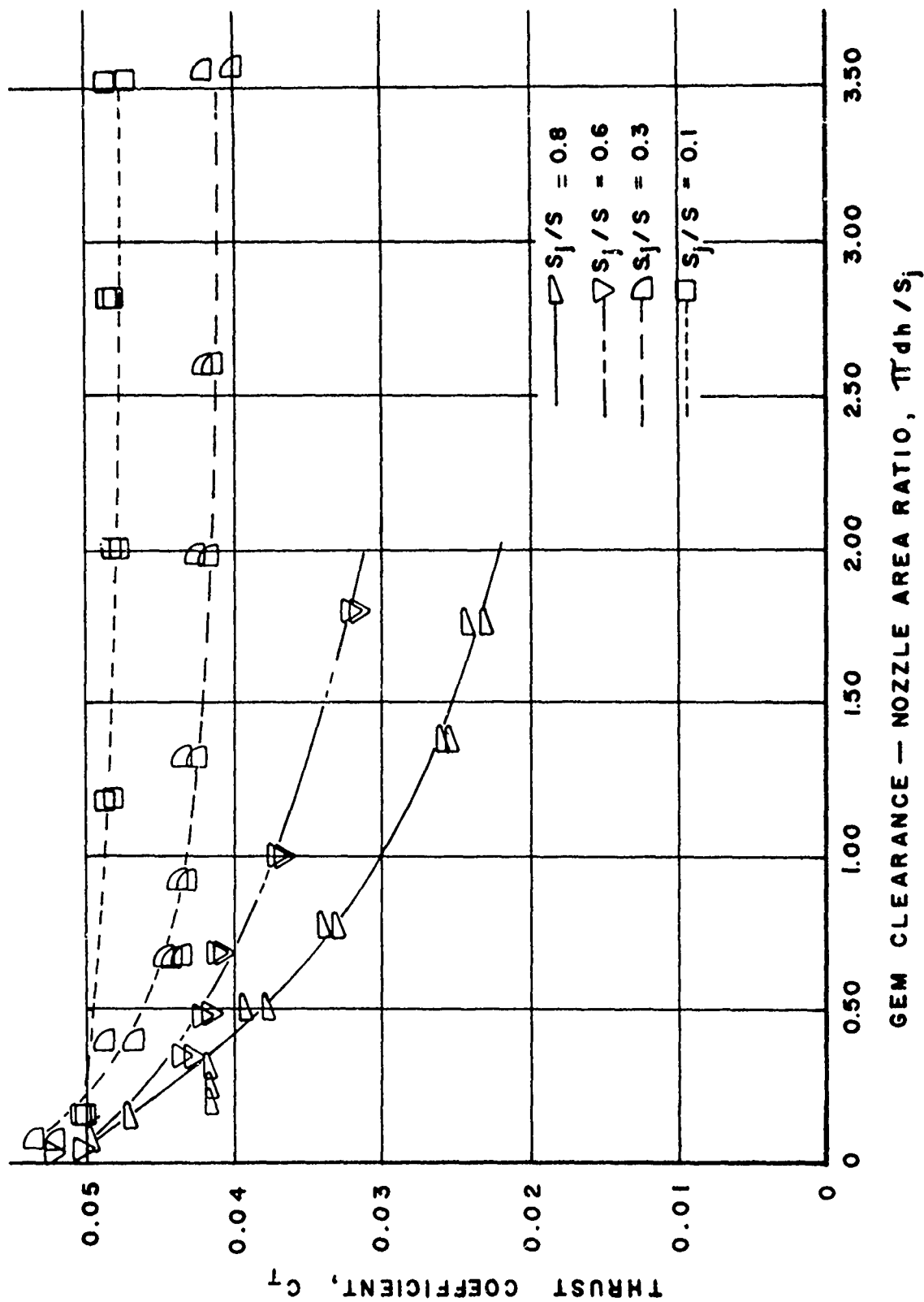
FIGURE 4: PROPELLER THRUST DATA FOR VARIOUS S_j/S CONFIGURATIONS, OPTIMIZED PROPELLER

75
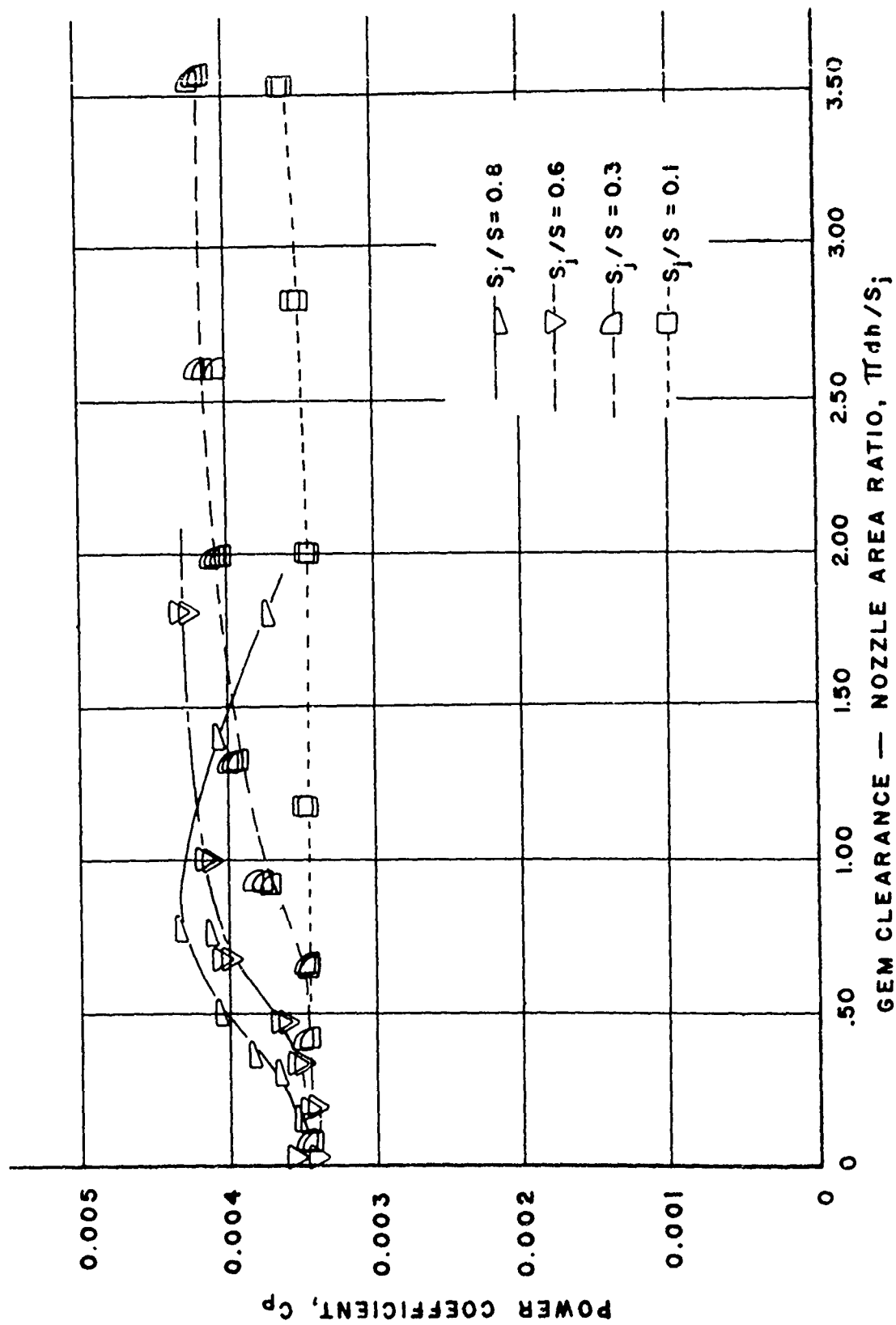
FIGURE 5: PROPELLER POWER DATA FOR VARIOUS S_j/S CONFIGURATIONS, OPTIMIZED PROPELLER

GEM CLEARANCE — NOZZLE AREA RATIO, $\pi dh/S_j$

POWER COEFFICIENT, C_p

$S_j/S = 0.8$
$S_j/S = 0.6$
$S_j/S = 0.3$
$S_j/S = 0.1$
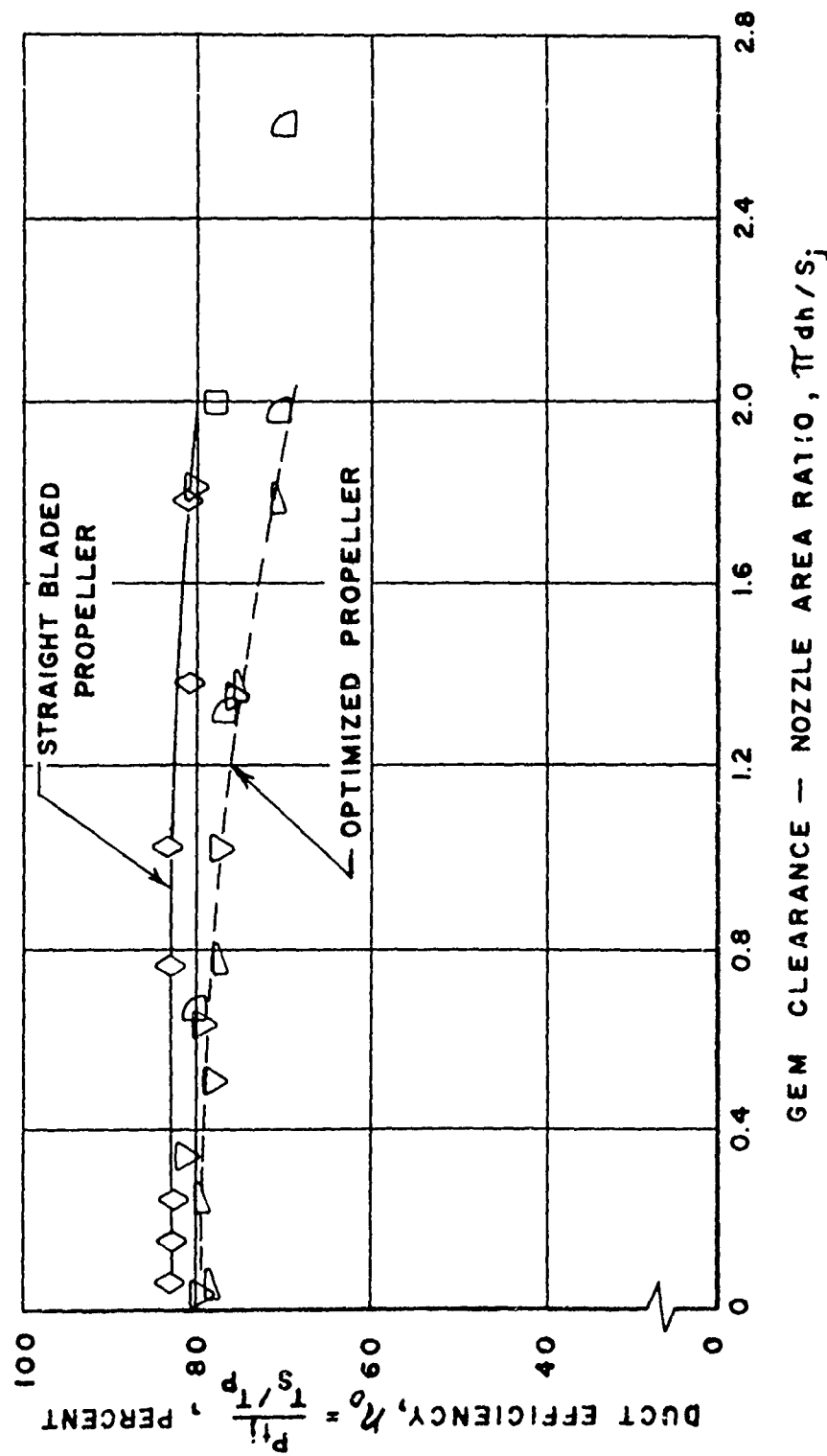
FIGURE 6: DUCT EFFICIENCY FOR STRAIGHT BLADED AND OPTIMIZED PROPELLERS

77
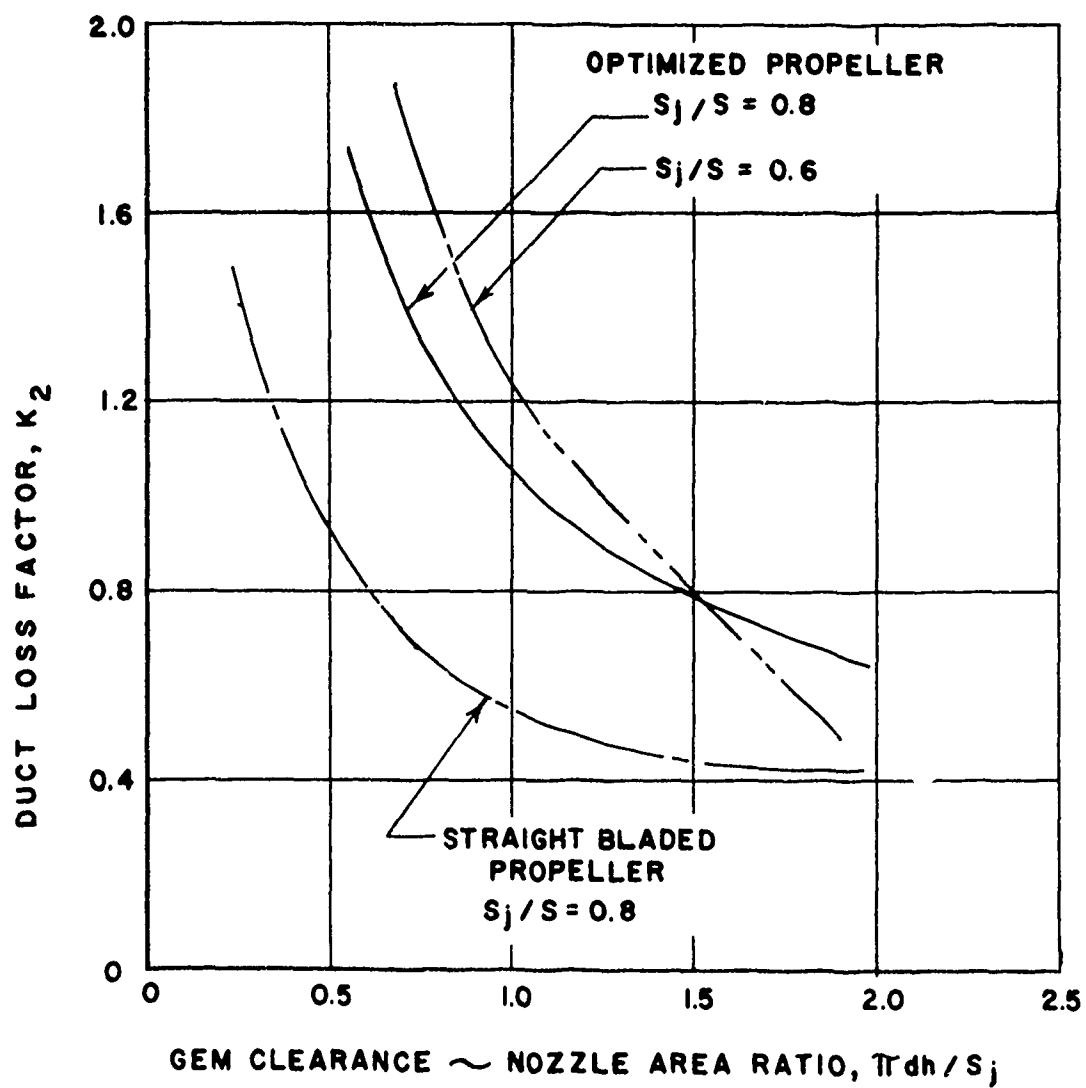
FIGURE 7: DUCT LOSS FACTOR FOR VARIOUS JET AREA CONFIGURATIONS

78
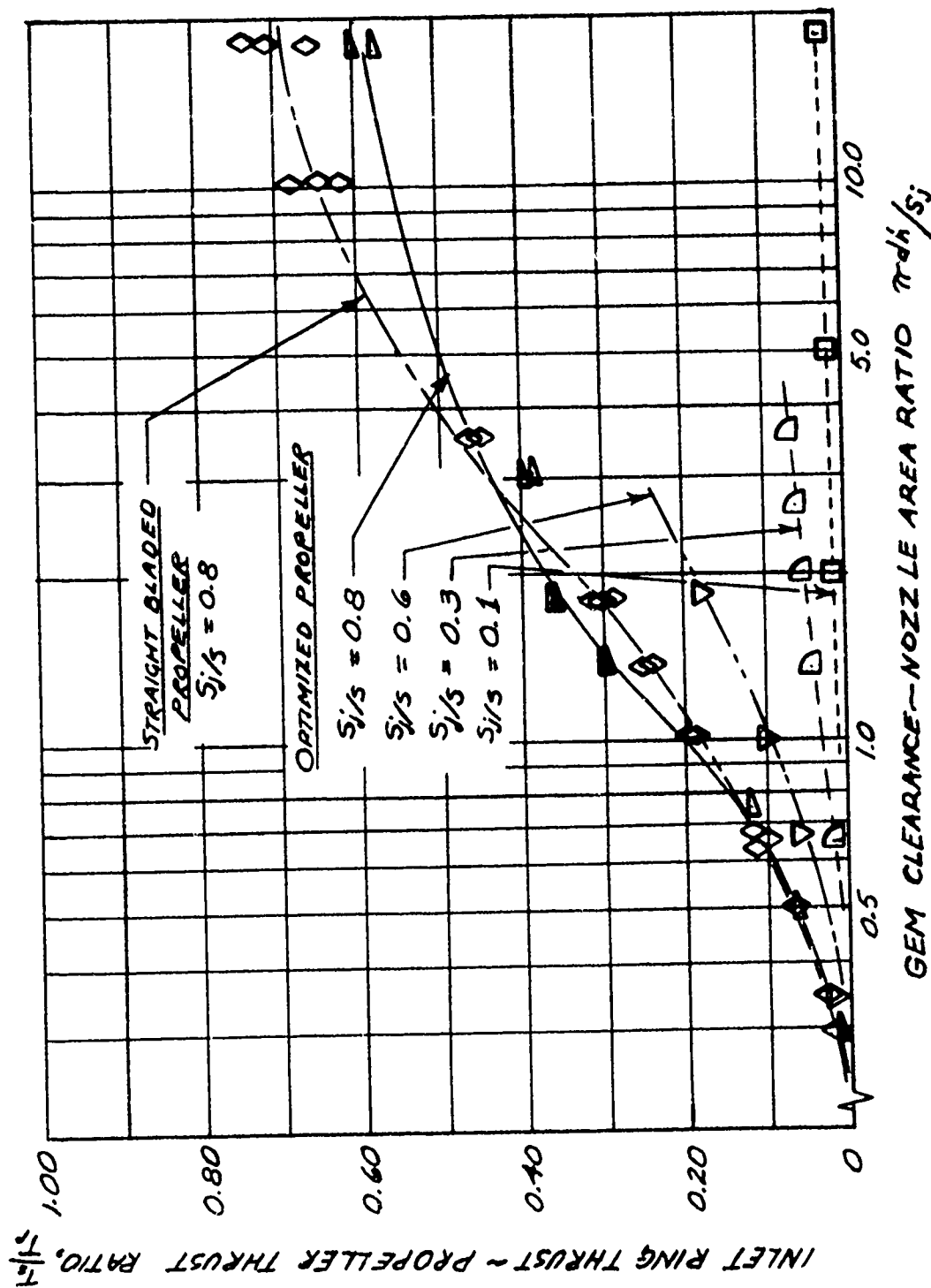
FIGURE 8: INFLUENCE OF NOZZLE HEIGHT ON INLET RING THRUST FOR THE STRAIGHT BLADED AND OPTIMIZED PROPELLERS

79

GEM CLEARANCE — NOZZLE AREA RATIO, $\pi\, dh/S_j$

INLET LOSS FACTOR, K

$S_j/S = 0.10$
$S_j/S = 0.30$
$S_j/S = 0.60$
$S_j/S = 0.60$
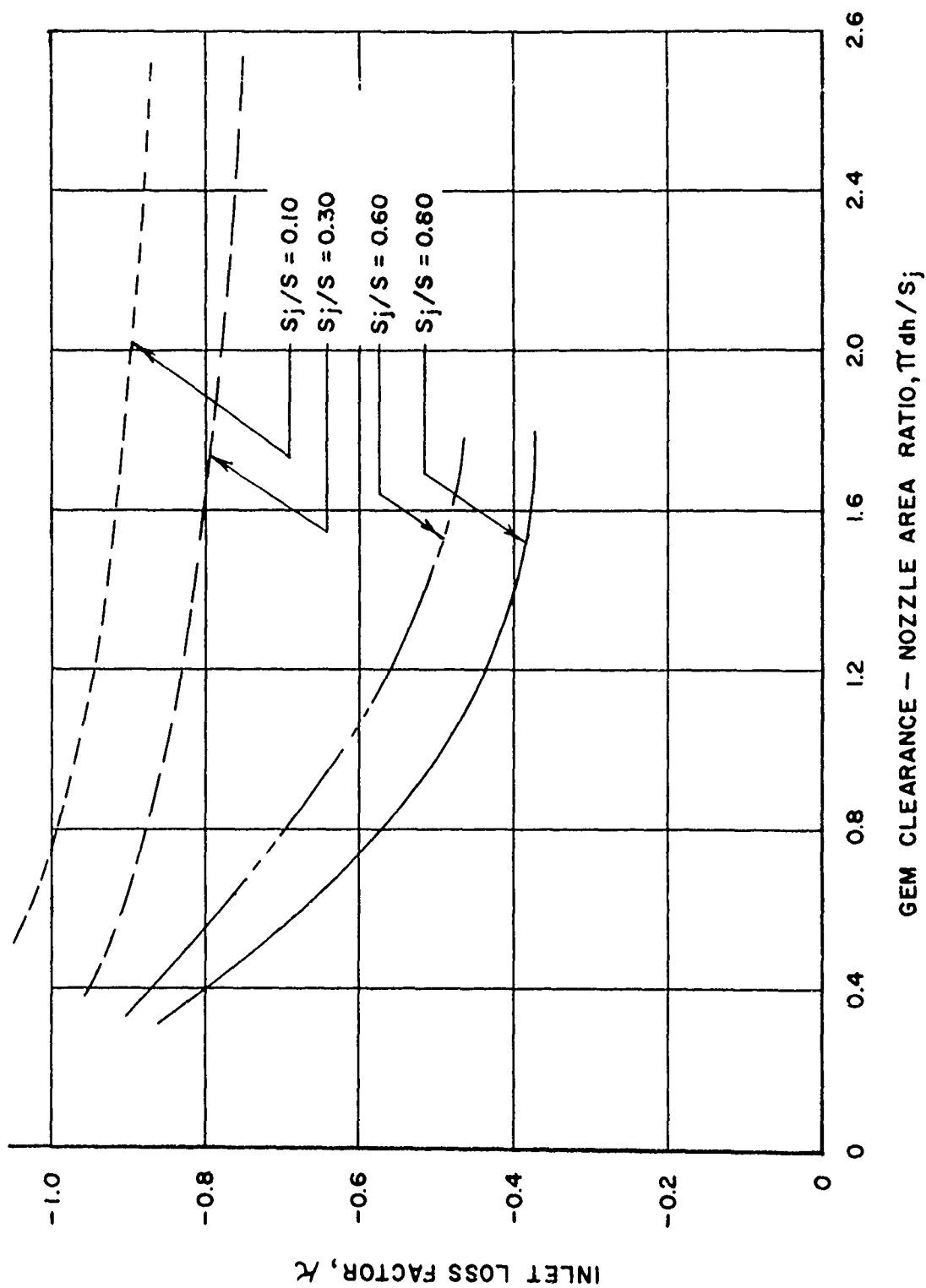
FIGURE 9: INLET LOSS FACTOR FOR VARIOUS JET AREA CONFIGURATIONS

80
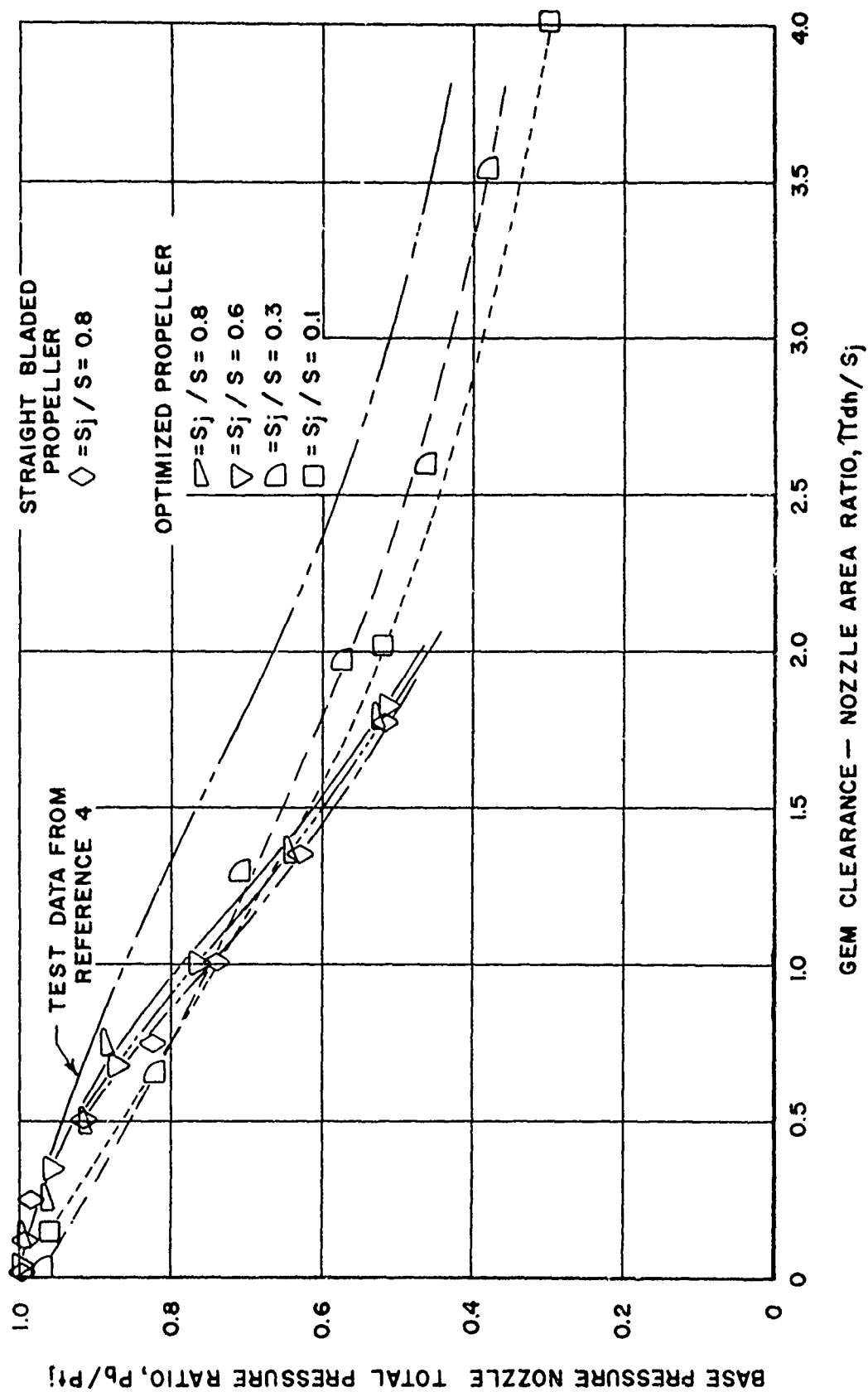
FIGURE 10: COMPARISON OF BASE PRESSURE TO NOZZLE TOTAL PRESSURE RATIO TEST DATA

81
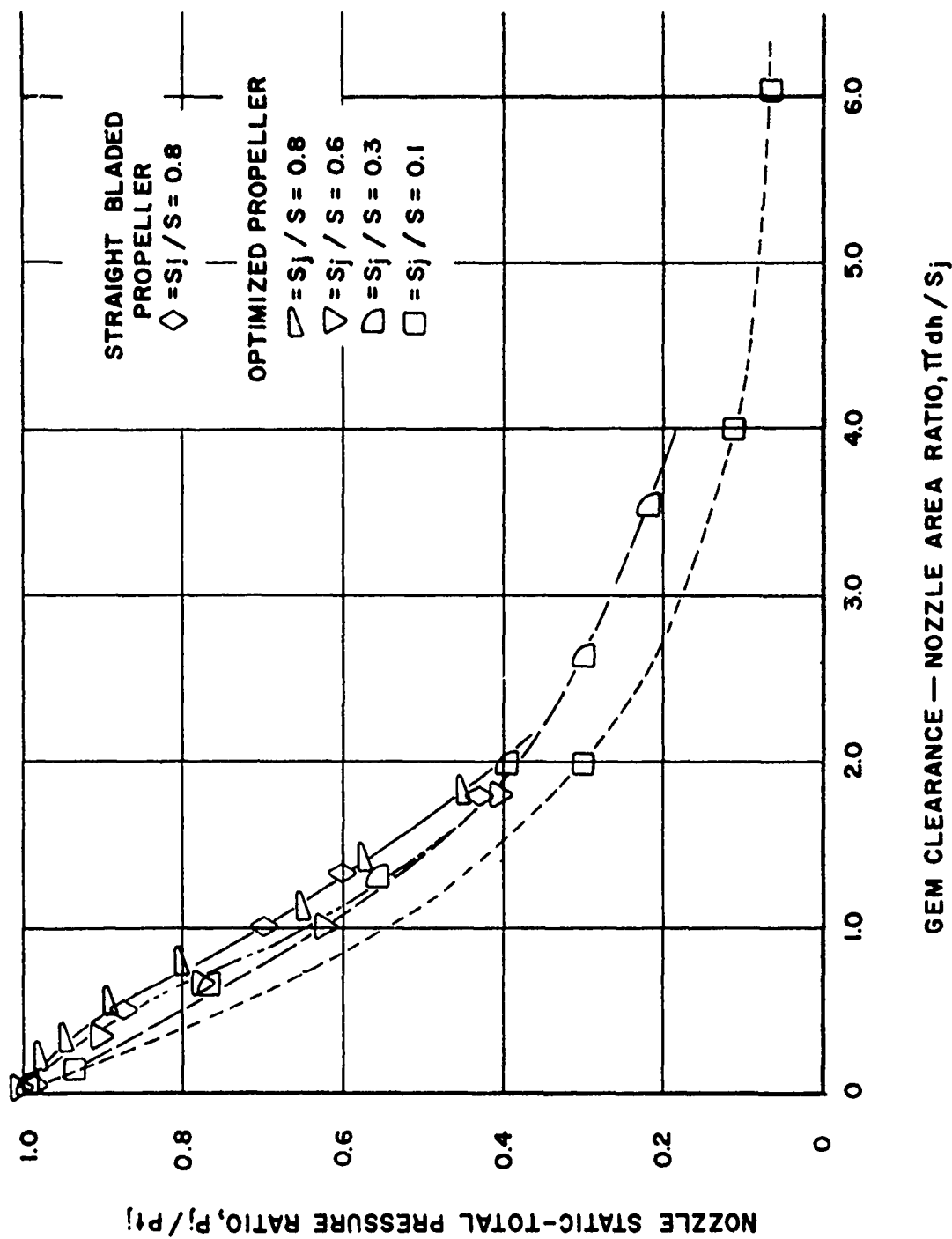
FIGURE 11: ANNULAR JET NOZZLE STATIC PRESSURE TO NOZZLE TOTAL PRESSURE RATIO FOR VARIOUS JET AREA CONFIGURATIONS

82
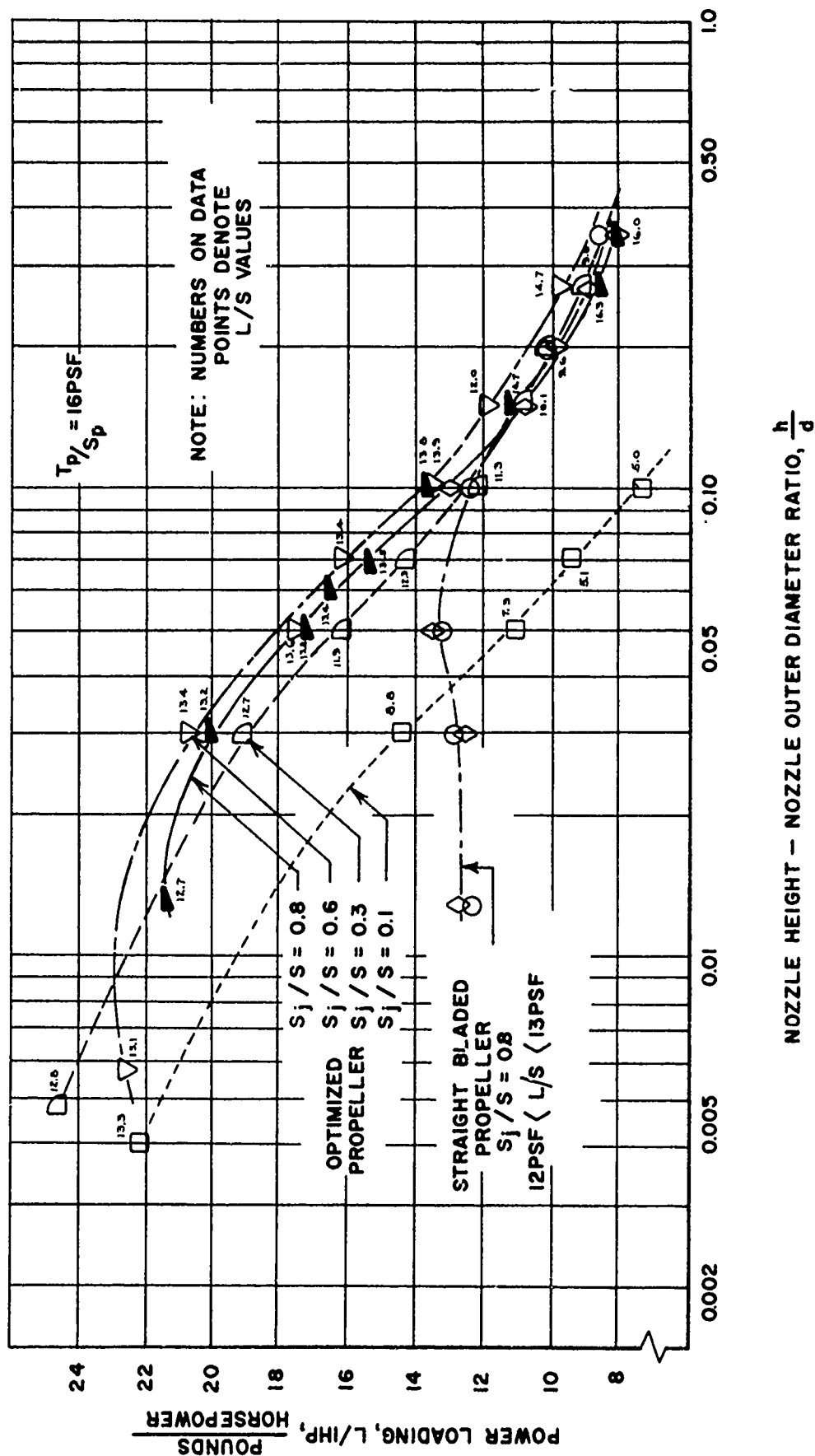
FIGURE 12: POWER LOADING PERFORMANCE OF GEM TEST UNIT AT CONSTANT PROPELLER DISC LOADING
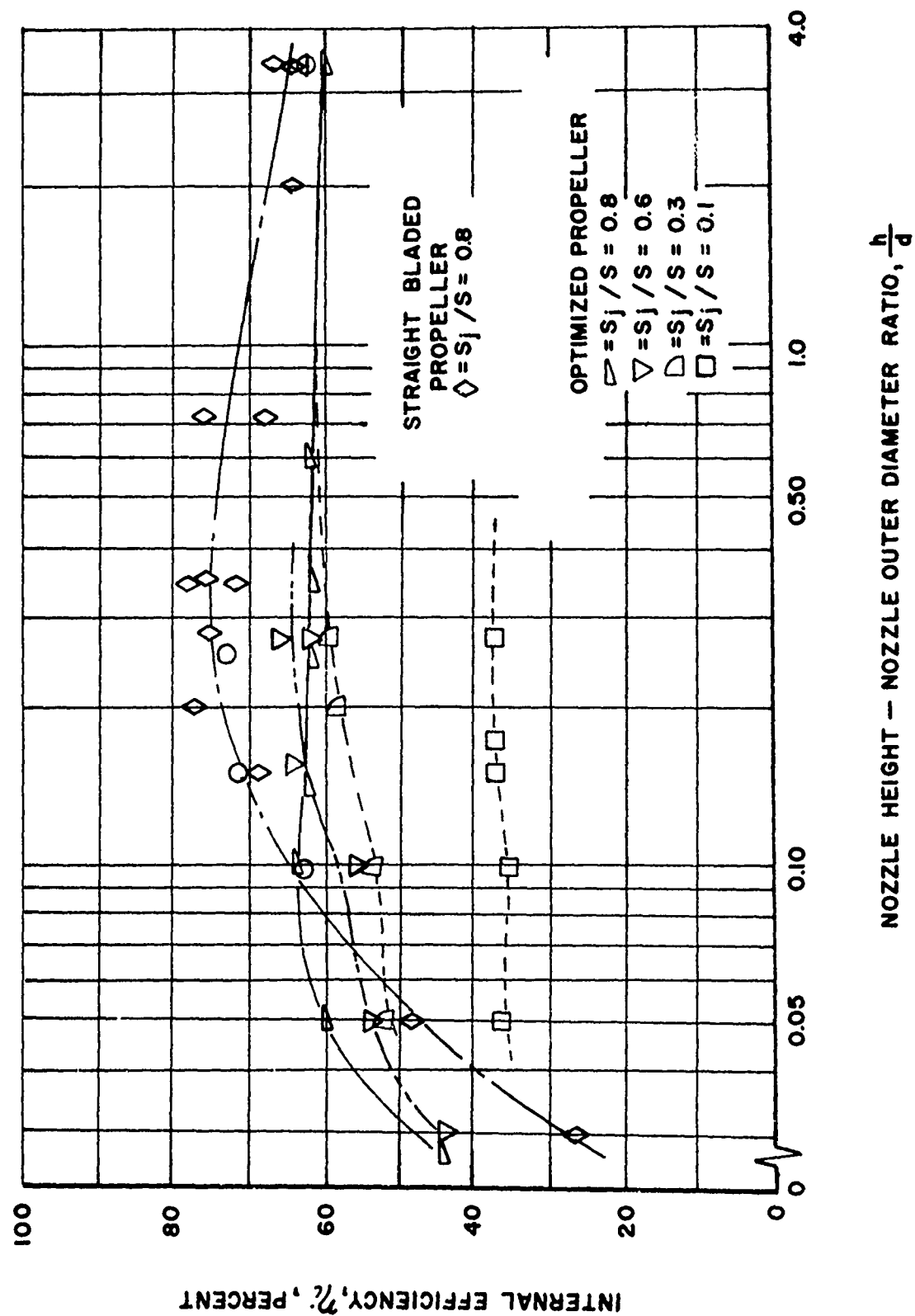
FIGURE 13: INTERNAL EFFICIENCY OF VARIOUS PROPELLER AND DUCT CONFIGURATIONS

84

NOZZLE HEIGHT – NOZZLE OUTER DIAMETER RATIO, h/d
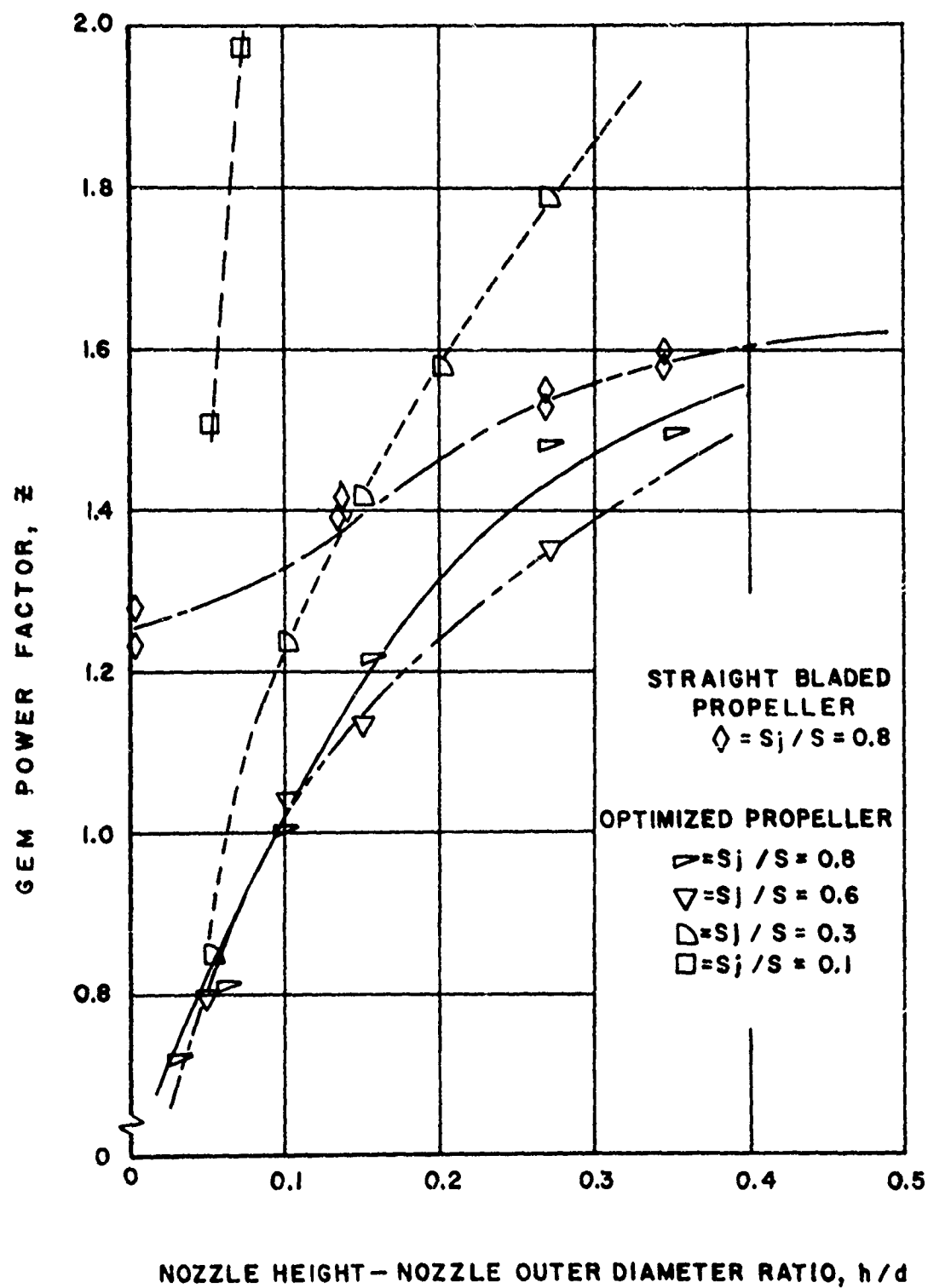
FIGURE 14:   GEM POWER FACTOR PERFORMANCE OF THE TEST UNIT
FOR THE VARIOUS CONFIGURATIONS TESTED

85
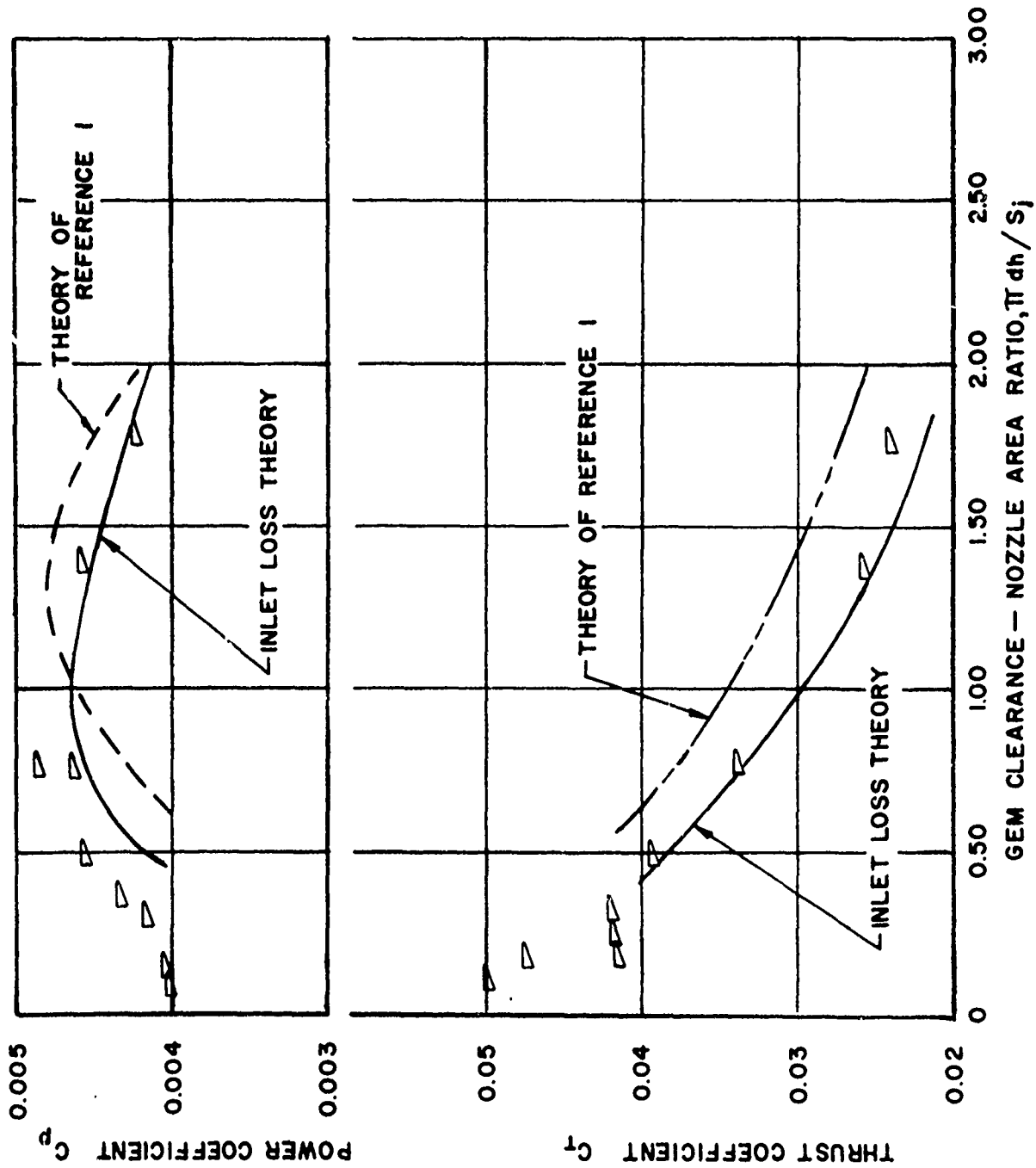
FIGURE 15: COMPARISON OF PREDICTED PERFORMANCE WITH PERFORMANCE TEST DATA, $\frac{S_j}{S} = 0.8$
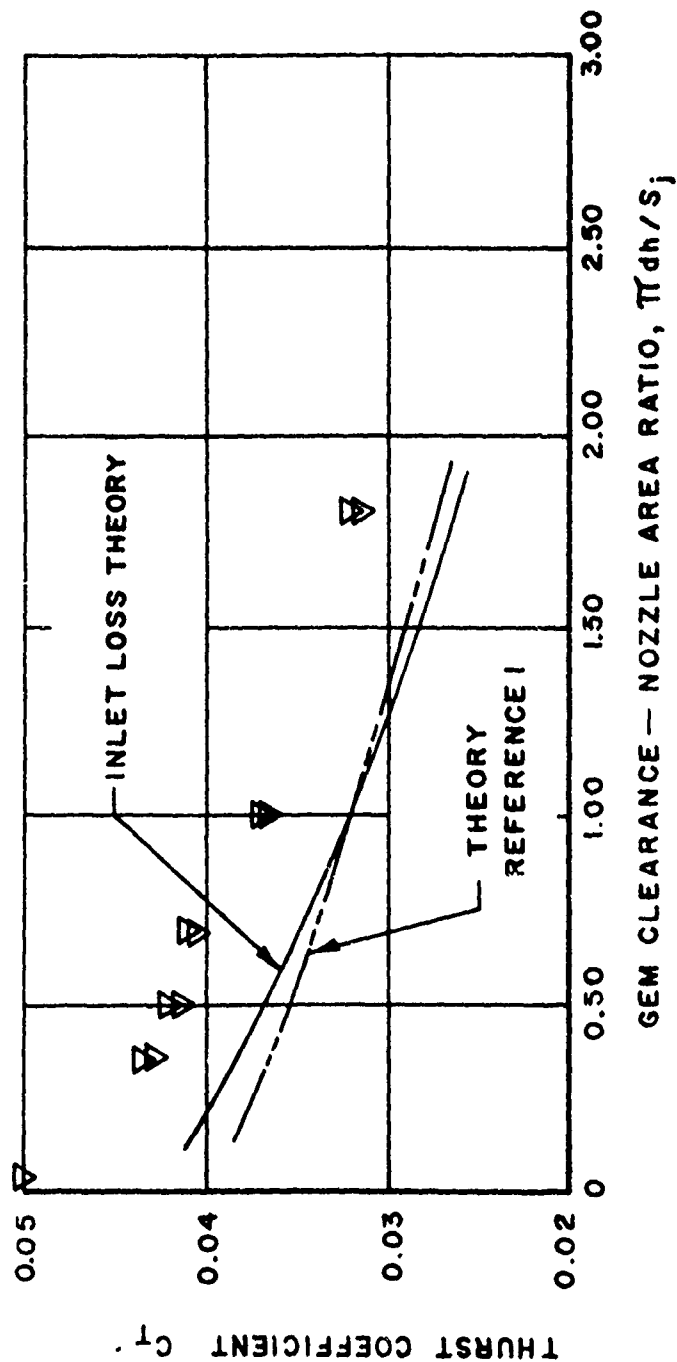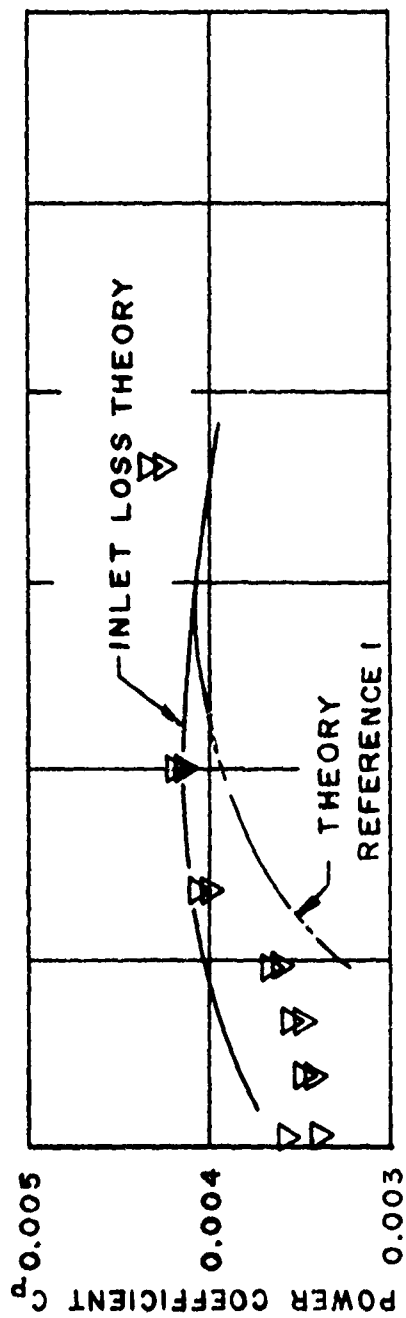
FIGURE 16: COMPARISON OF PREDICTED PERFORMANCE WITH PERFORMANCE TEST DATA, $\frac{S_j}{S} = 0.6$

87
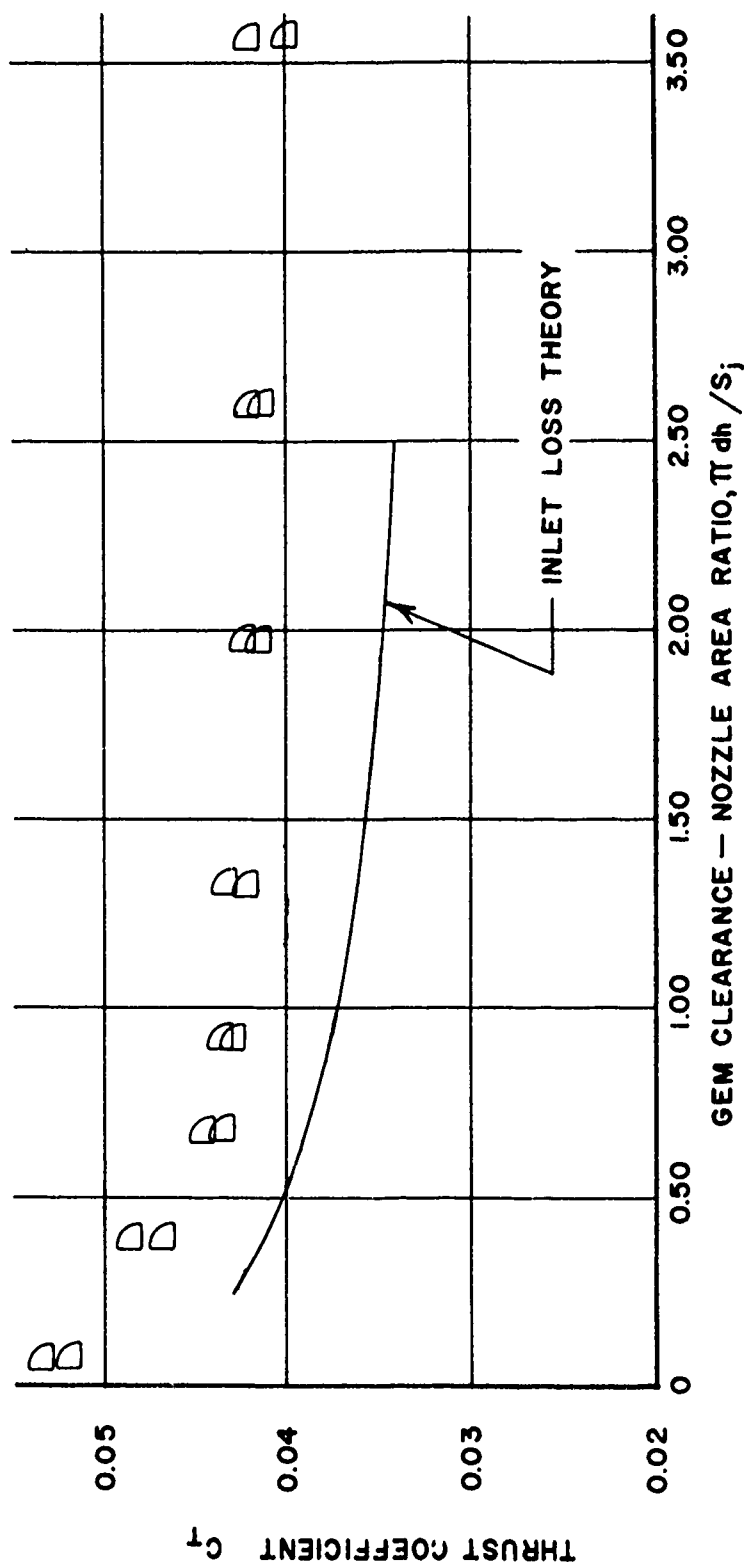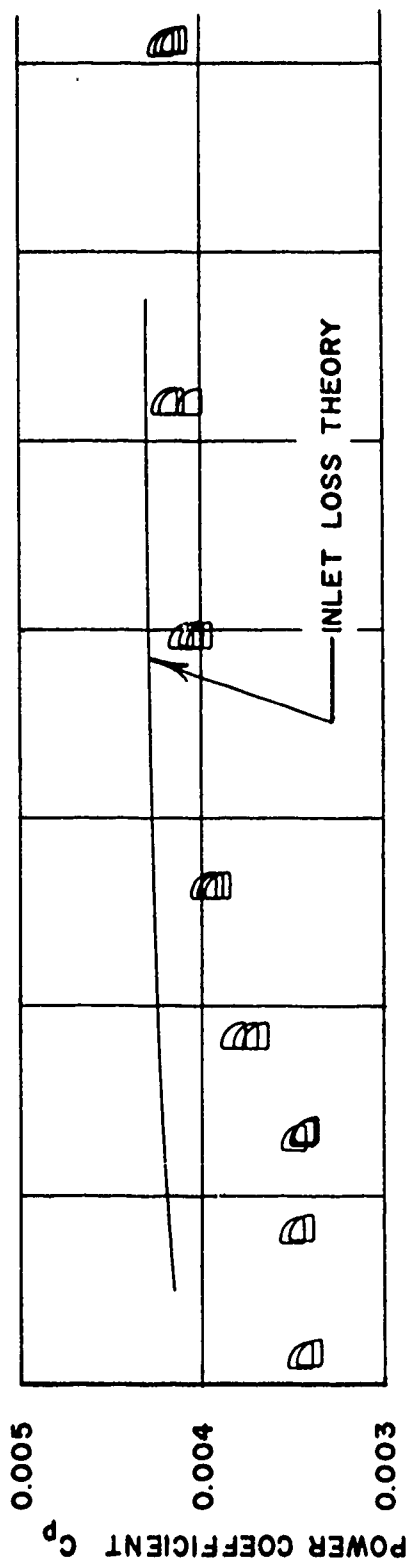
FIGURE 17: COMPARISON OF PREDICTED PERFORMANCE WITH PERFORMANCE TEST DATA, $\frac{S_j}{S} = 0.3$

88
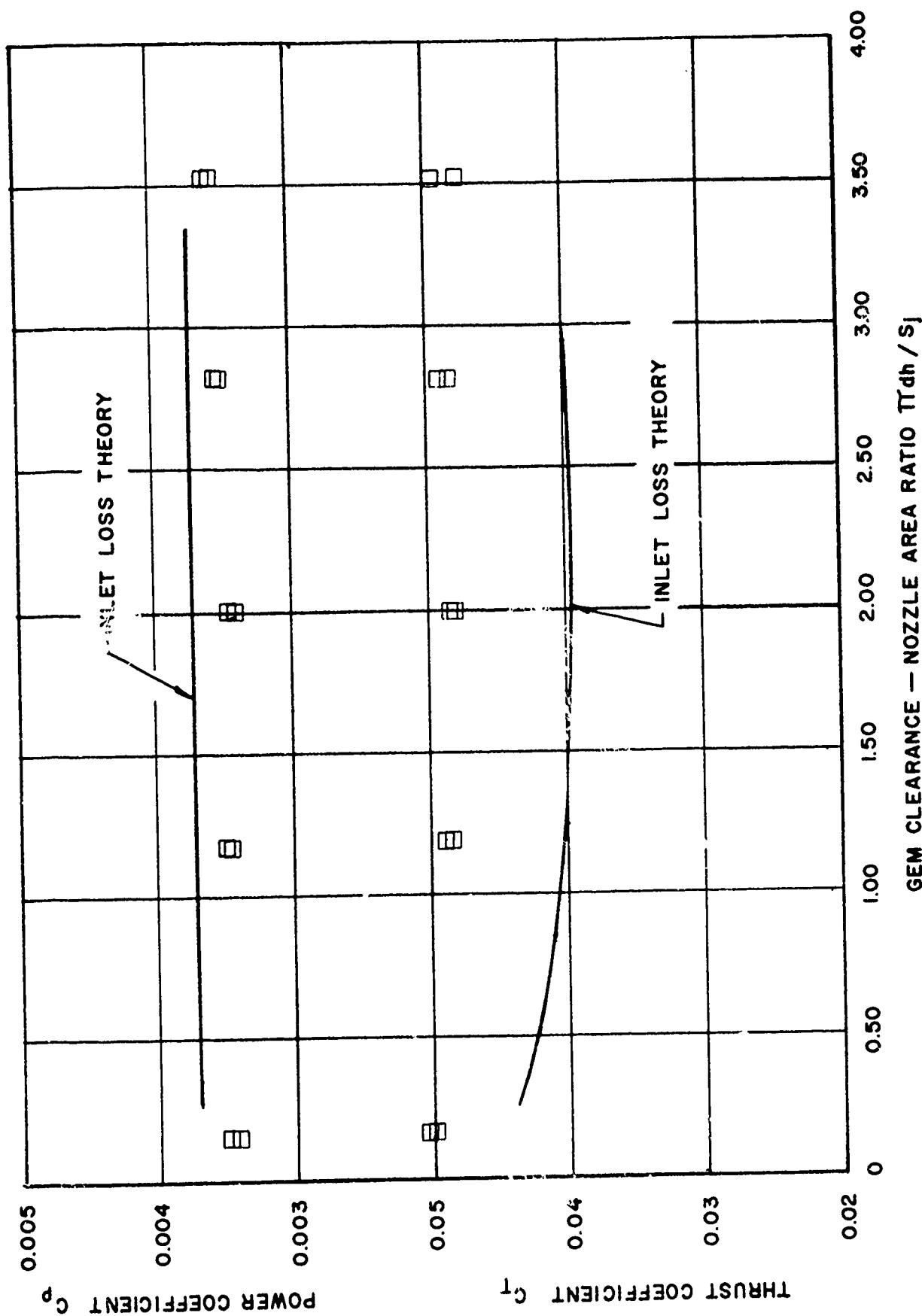
FIGURE 18: COMPARISON OF PREDICTED PERFORMANCE WITH PERFORMANCE TEST DATA, $\dfrac{S_j}{S} = 0.1$
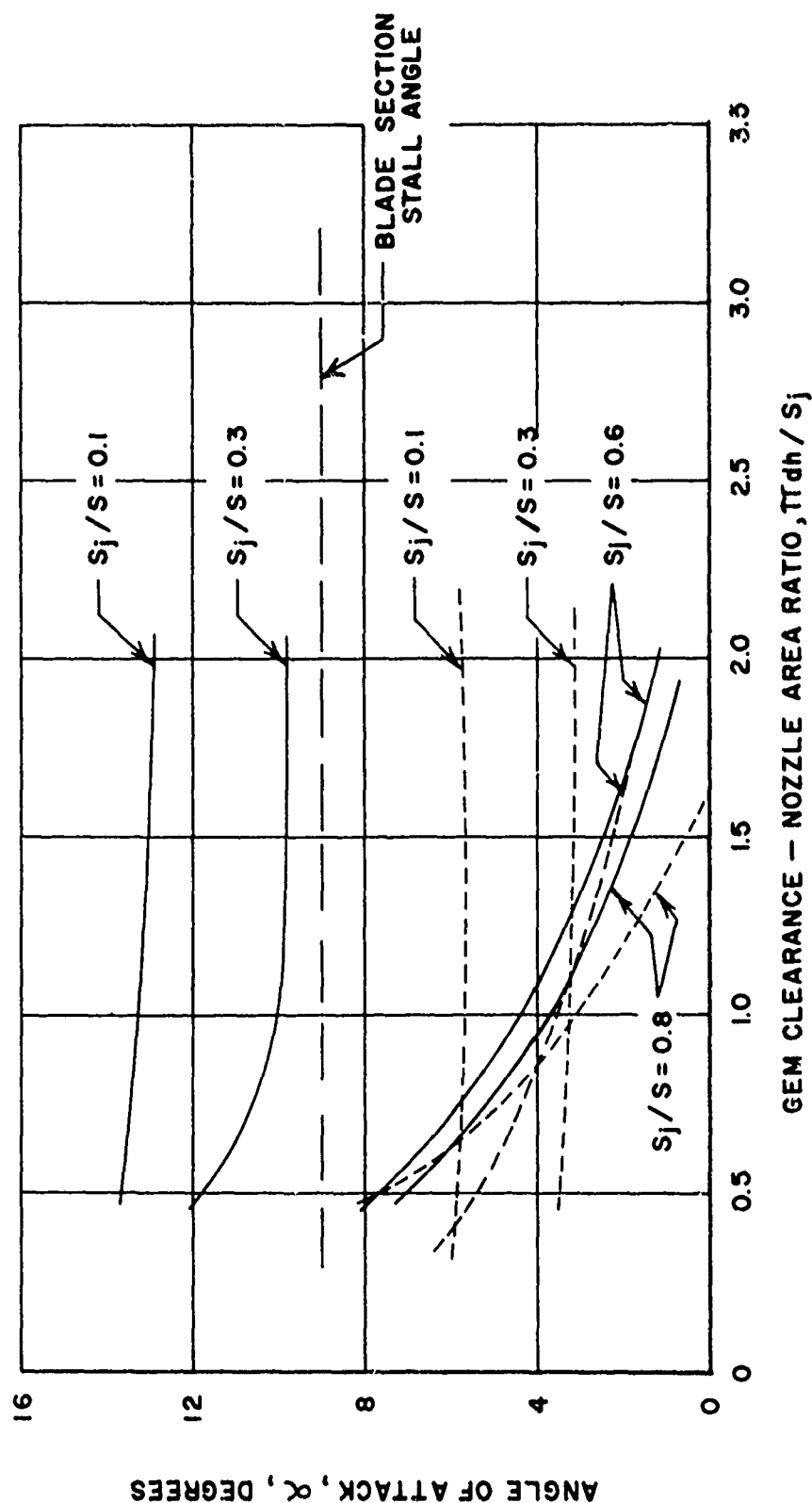
FIGURE 19: COMPARISON OF PREDICTED AND ESTIMATED ANGLE OF ATTACK OF ROOT SECTION (X of 0.51), OPTIMIZED PROPELLER

TEST DATA MEASURED AT Z/R = 0.17

SYMBOL	h/d	$\pi dh/S_j$
--◇---	0.15	0.75
---◯---	0.27	1.37
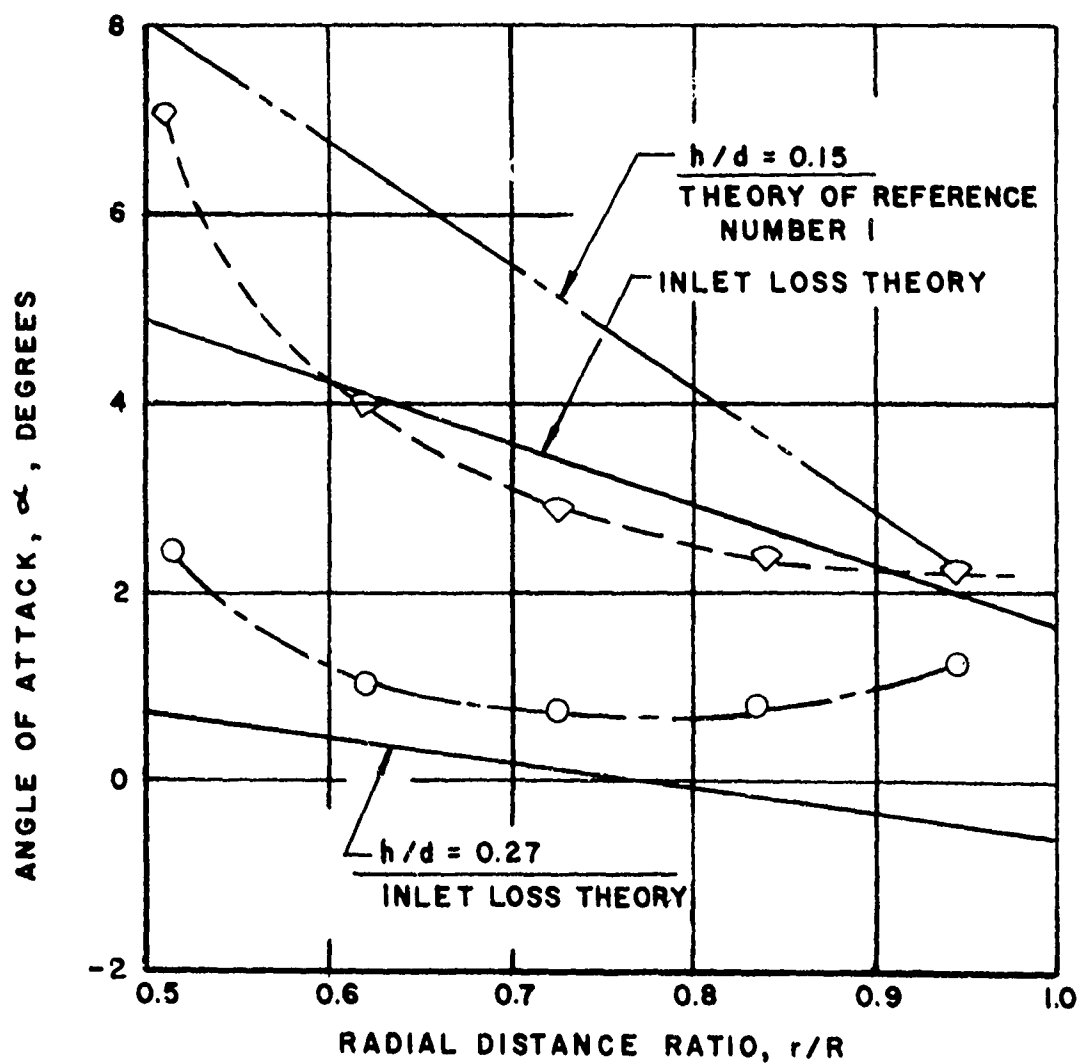
FIGURE 20: COMPARISON OF MEASURED AND CALCULATED ANGLE OF ATTACK DISTRIBUTION FOR $S_j/S = 0.8$, OPTIMIZED PROPELLER

91

SYMBOL	h/d	$\pi dh/S_j$
---□---	0.05	0.34
---◇---	0.15	1.02
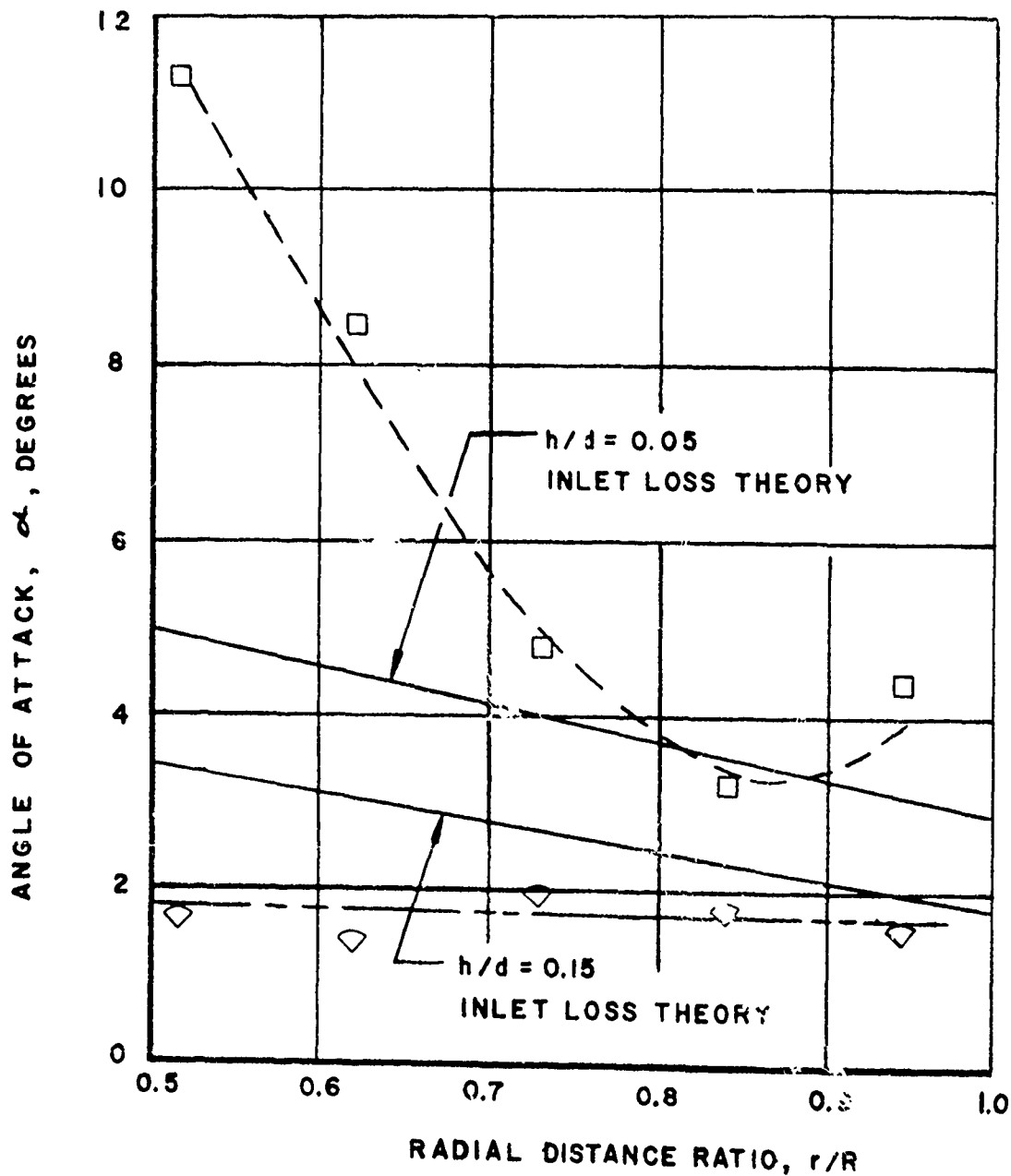
FIGURE 21: COMPARISON OF MEASURED AND CALCULATED ANGLE OF ATTACK DISTRIBUTION FOR $S_j/S = 0.0$, OPTIMIZED PROPELLER

92
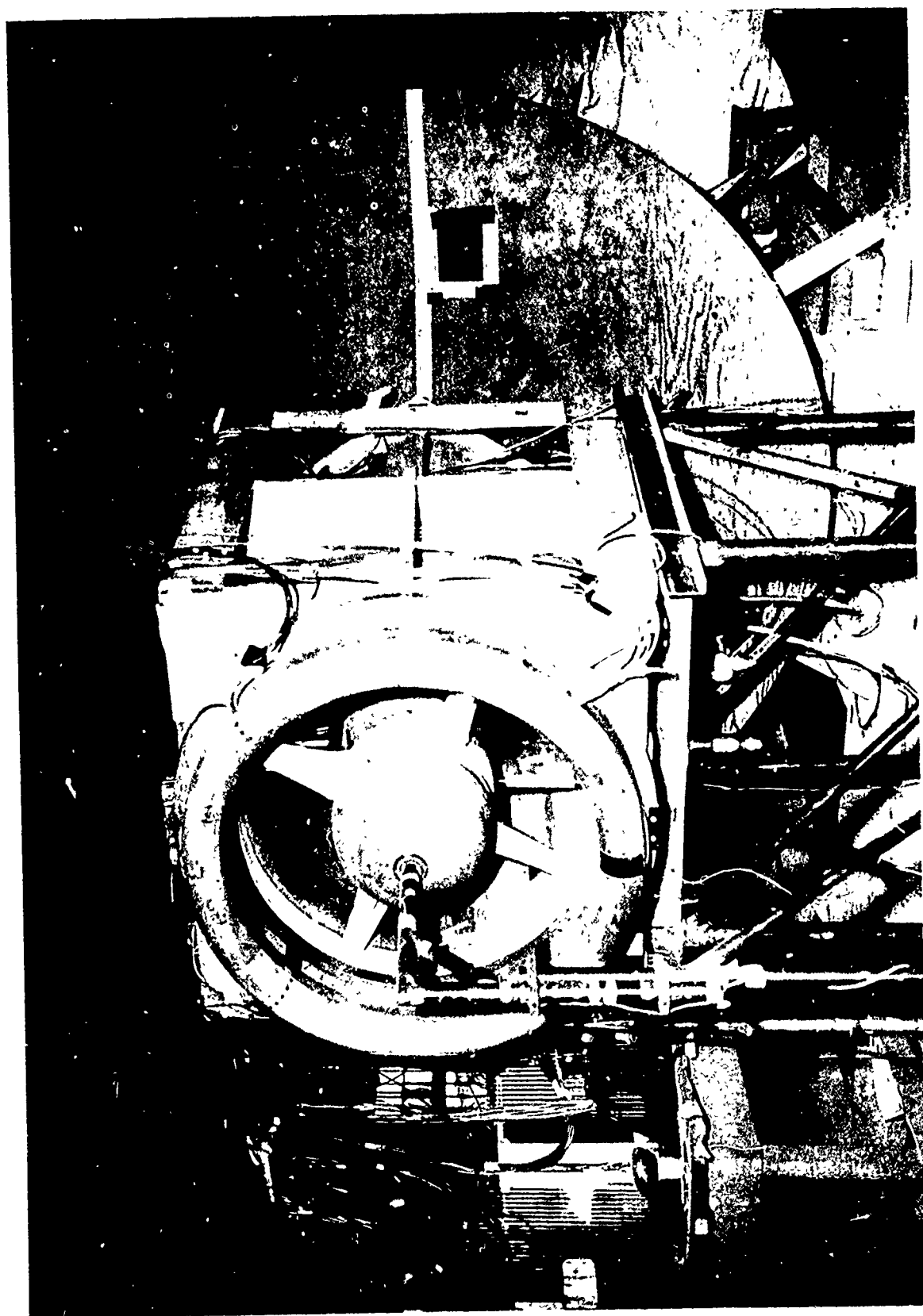
FIGURE 22: GEM TEST DEVICE WITH 4.5-INCH INLET RING AND OPTIMIZED PROPELLER
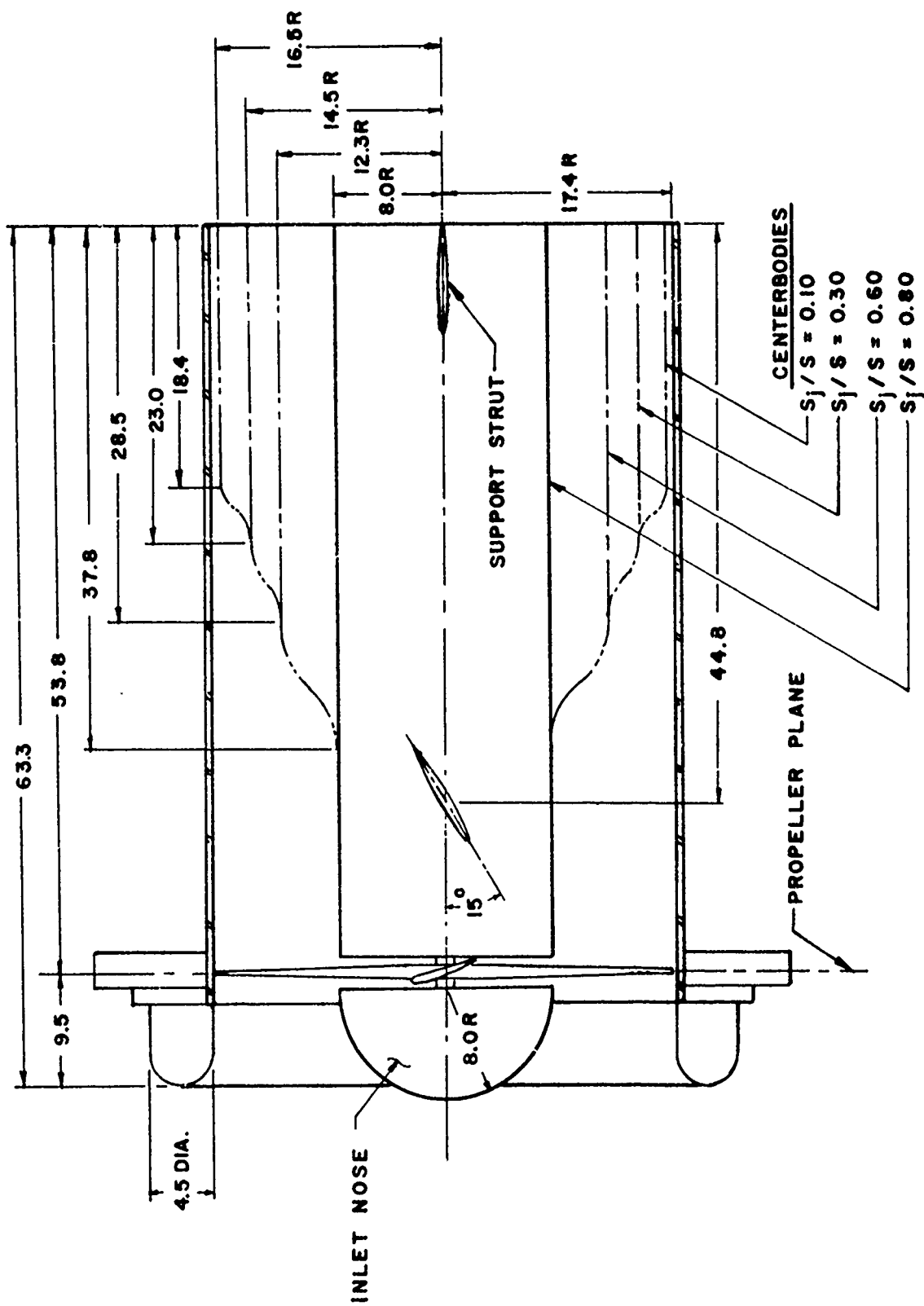
FIGURE 23: STRAIGHT DUCT GEM TEST DEVICE WITH PROVISIONS FOR FOUR CENTERBODY CONFIGURATIONS
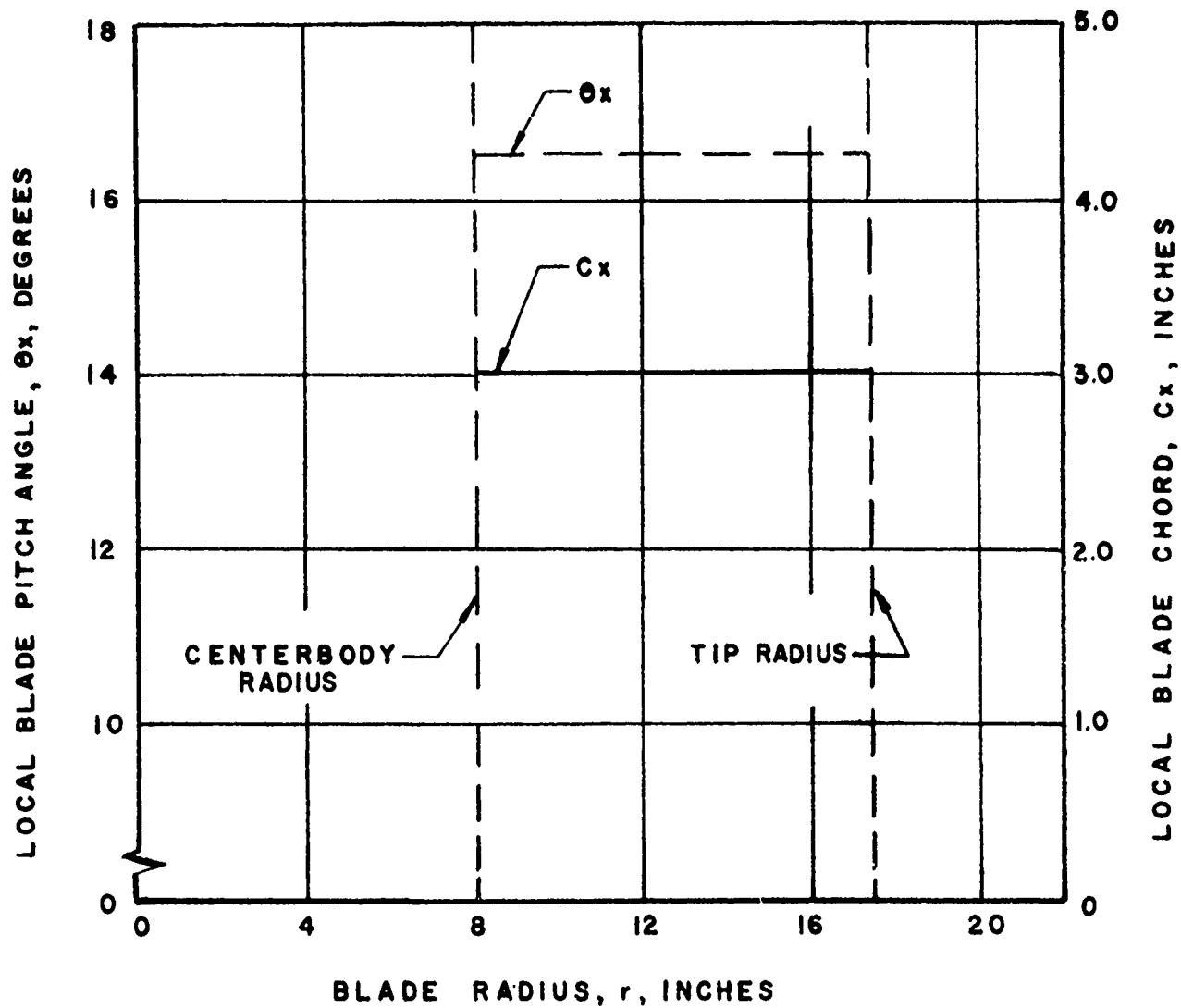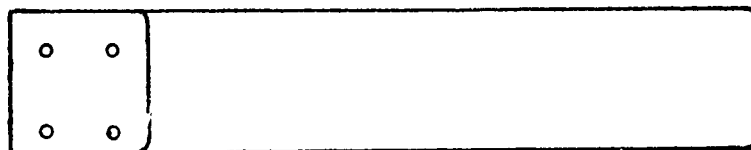
FIGURE 24:   BLADE CHARACTERISTICS OF STRAIGHT BLADED PROPELLER
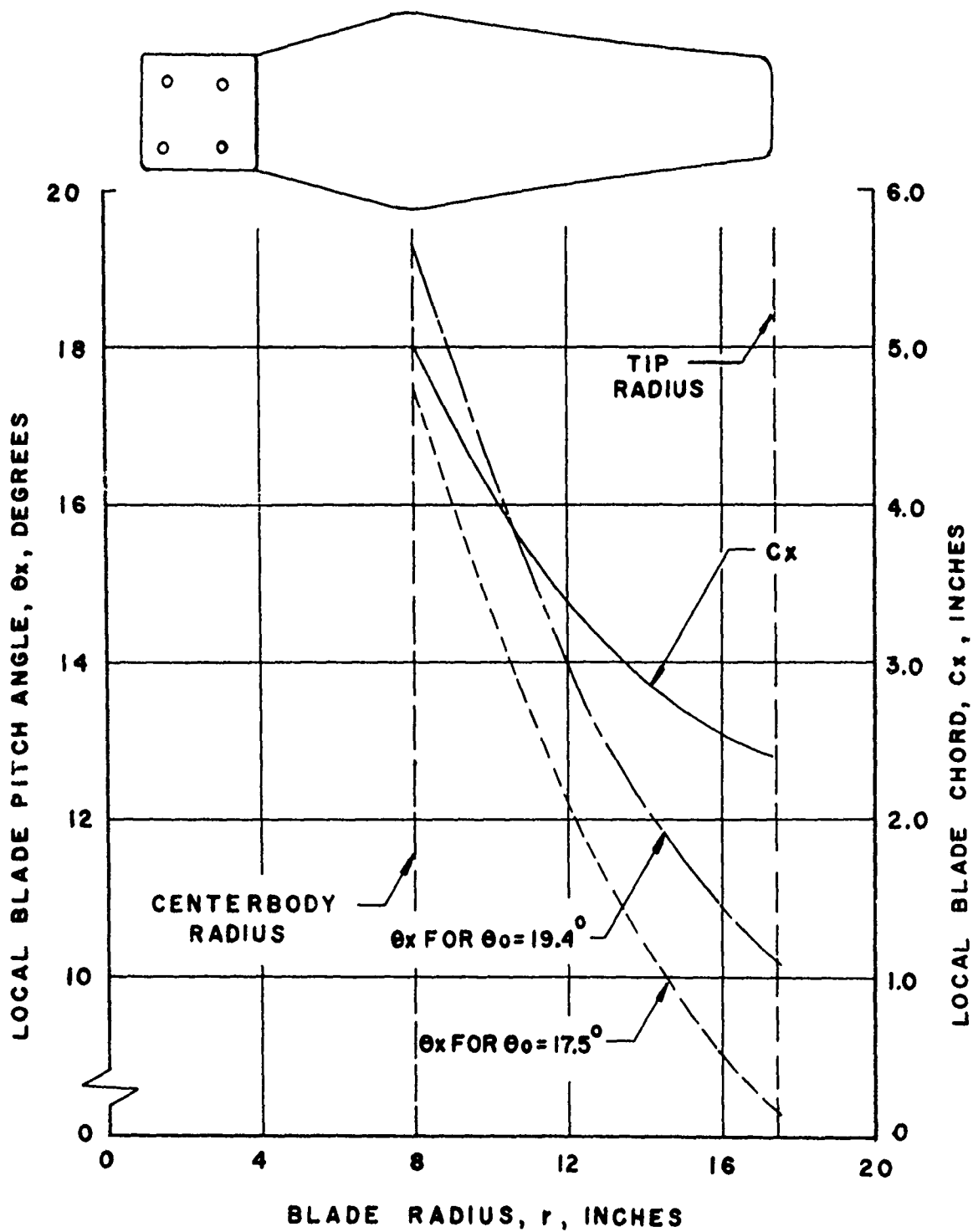
FIGURE 25: BLADE CHARACTERISTICS OF OPTIMIZED PROPELLER

96
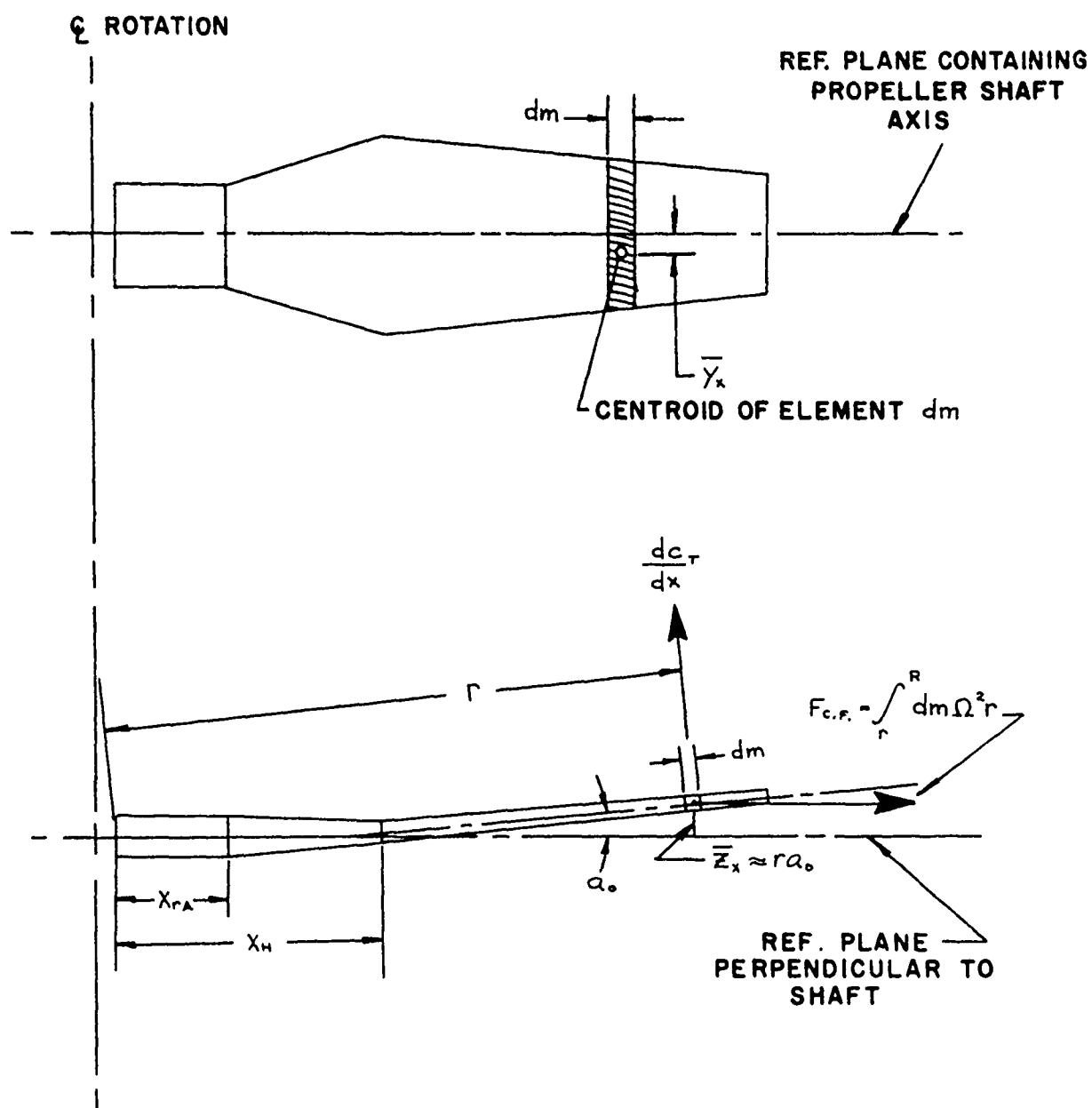
FIGURE 26:   PROPELLER NOTATION
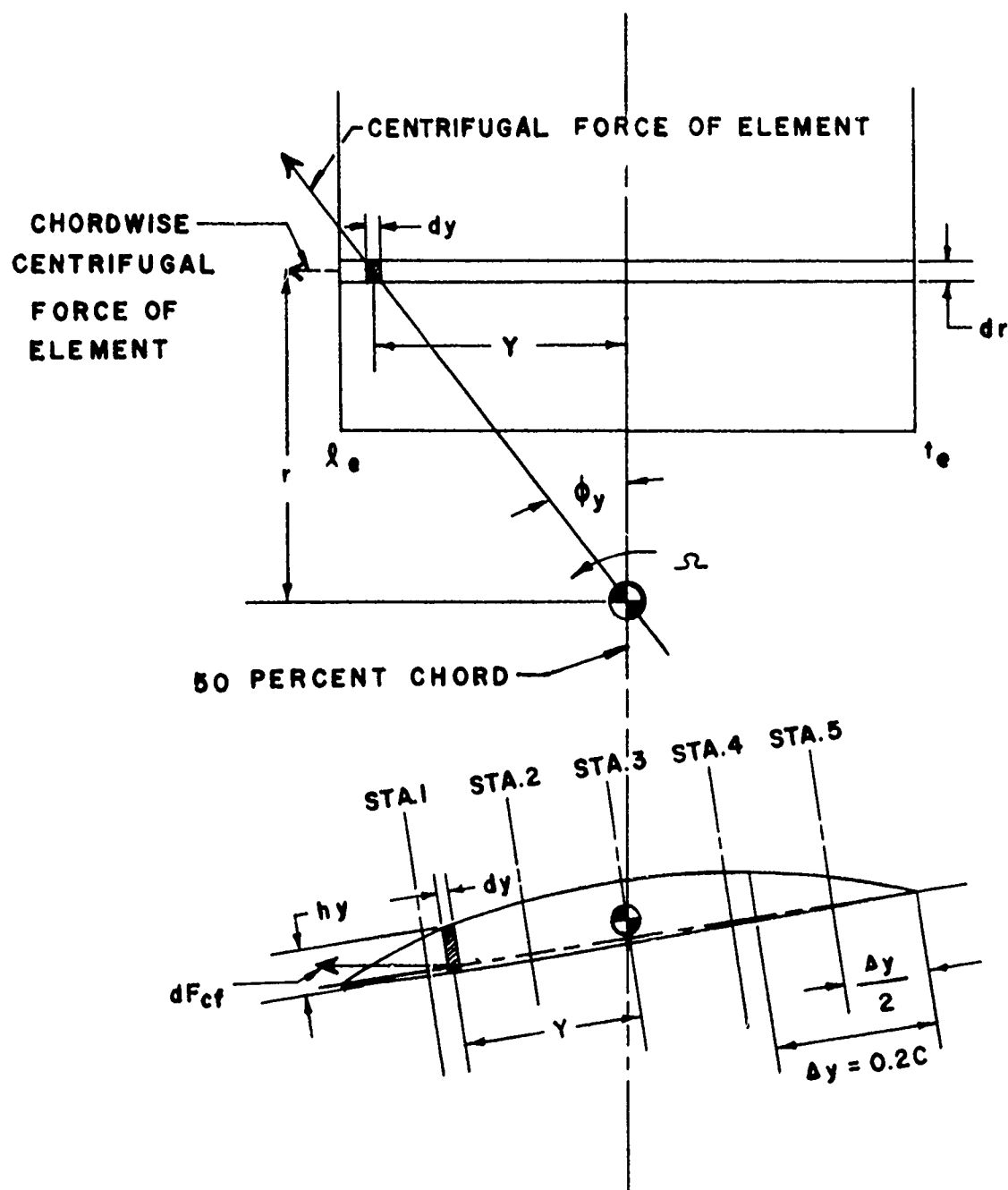
FIGURE 27: NOTATION FOR THE DETERMINATION OF PROPELLER
TORSIONAL MOMENTS

98
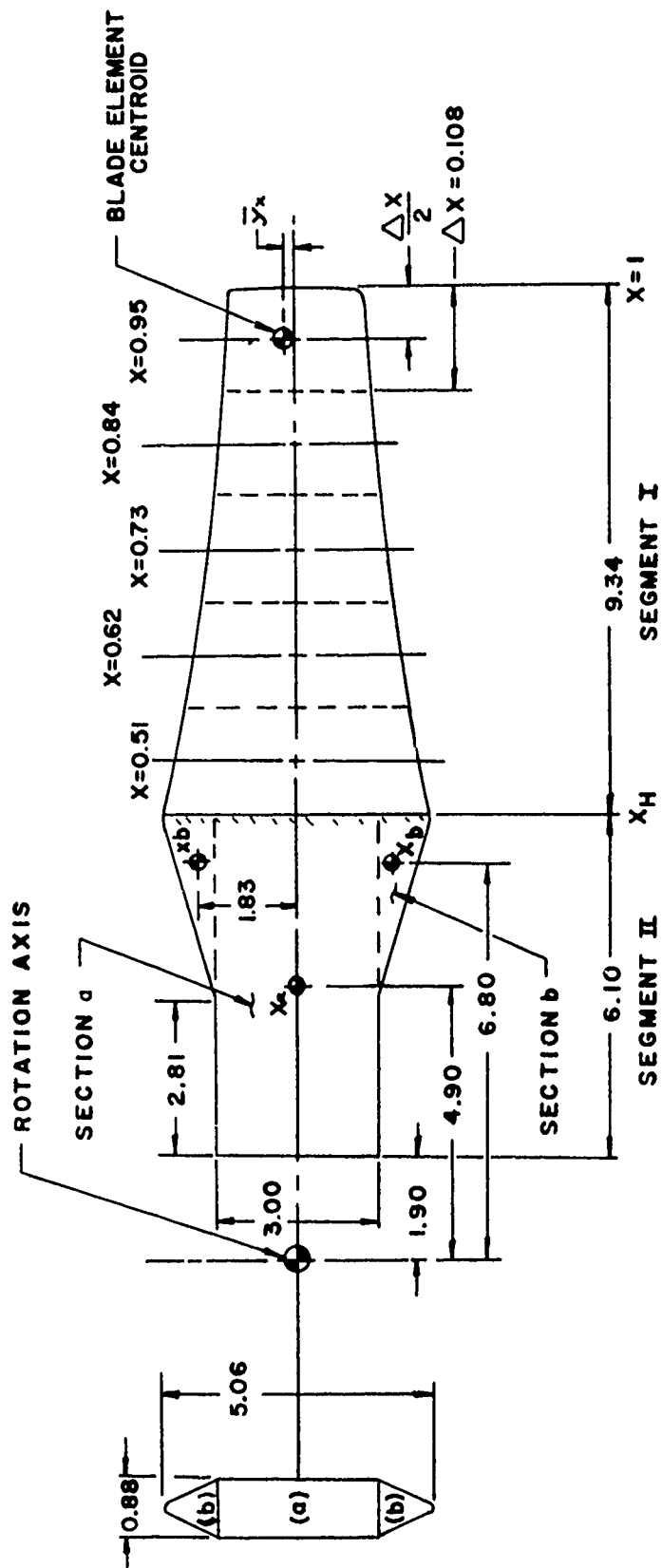
FIGURE 28: PROPELLER PLANFORM GEOMETRY

99

AIRFOILS SHOWN ARE NACA SECTIONS

EXCEPT WHERE NOTED.

DATA FROM REFERENCE 6
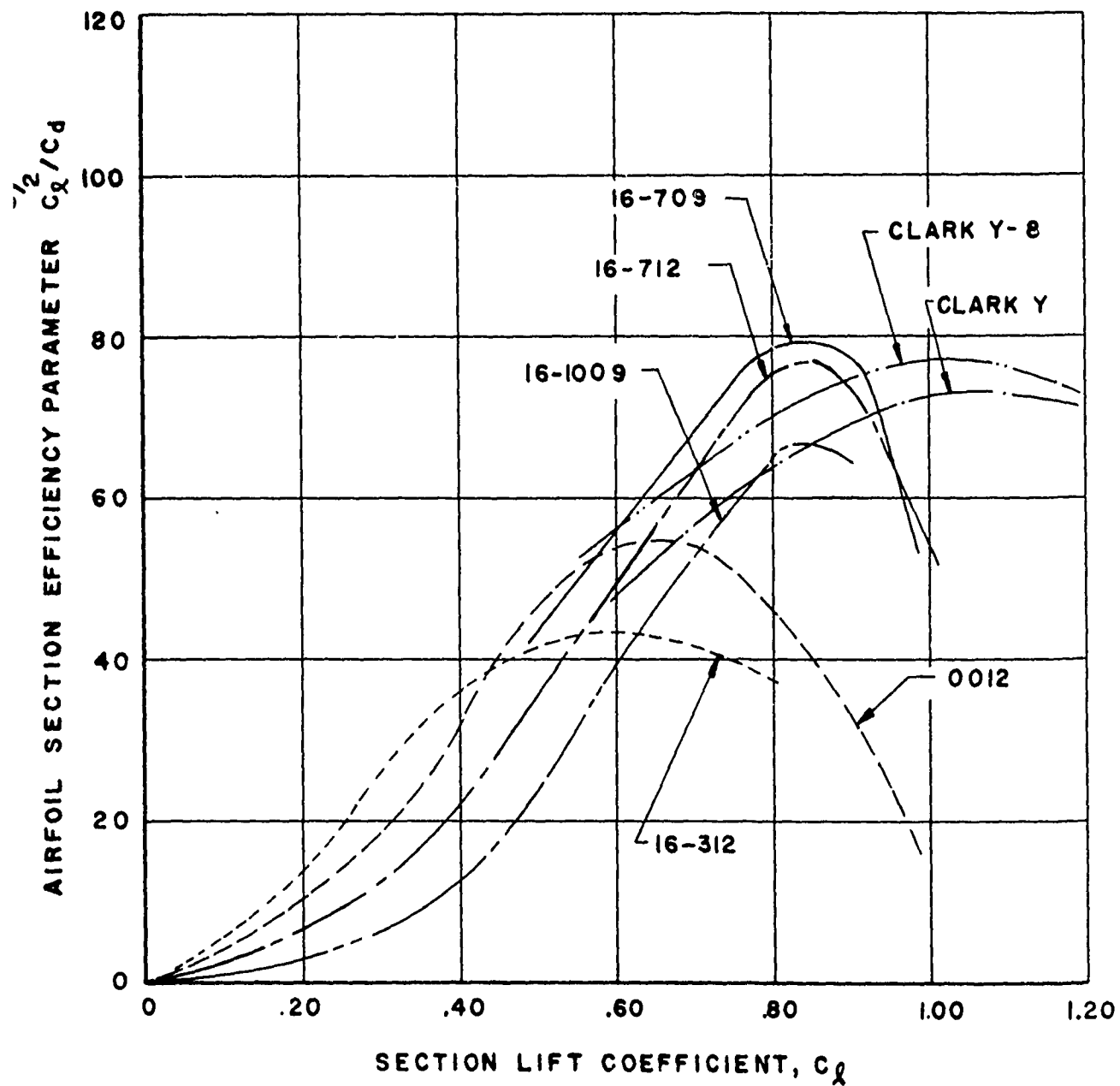
FIGURE 29: AIRFOIL SECTION EFFICIENCY OF SEVERAL AIRFOILS

100
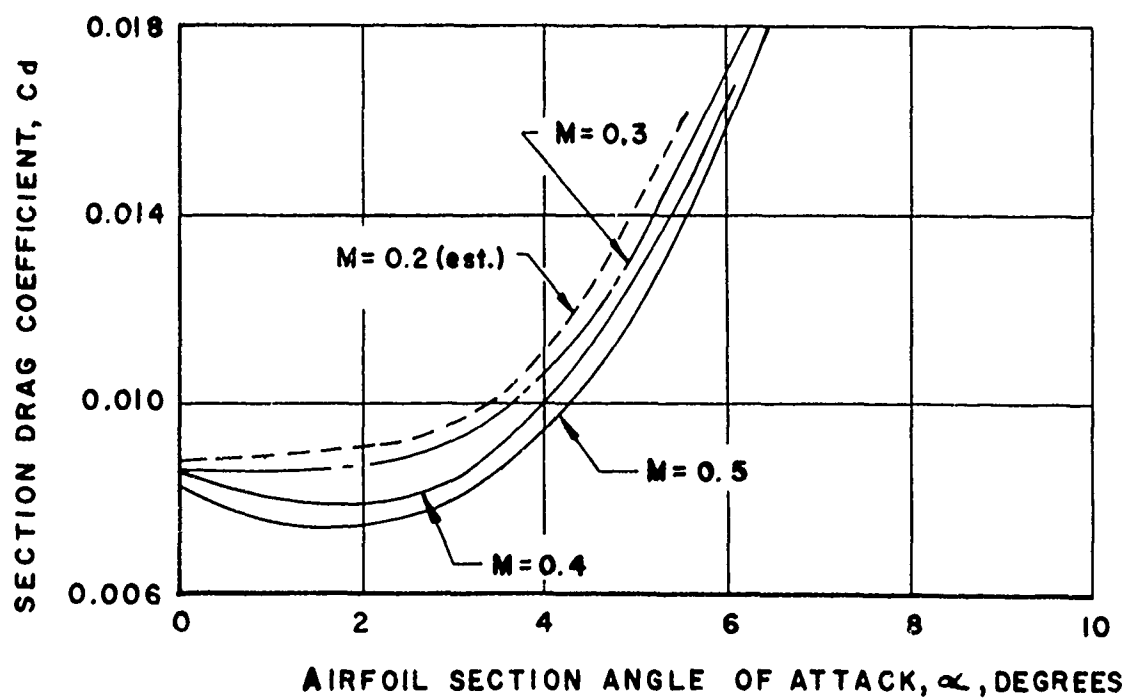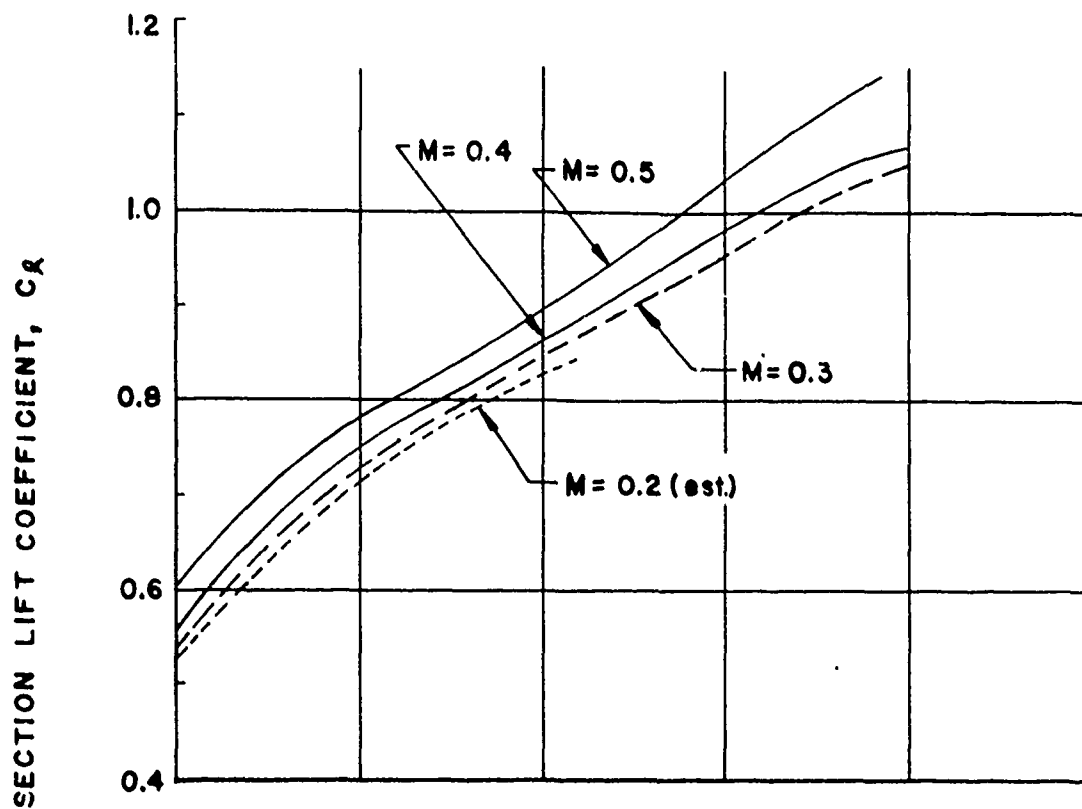
FIGURE 30: NACA 16709 SERIES AIRFOIL CHARACTERISTICS
(FROM REFERENCE 6)
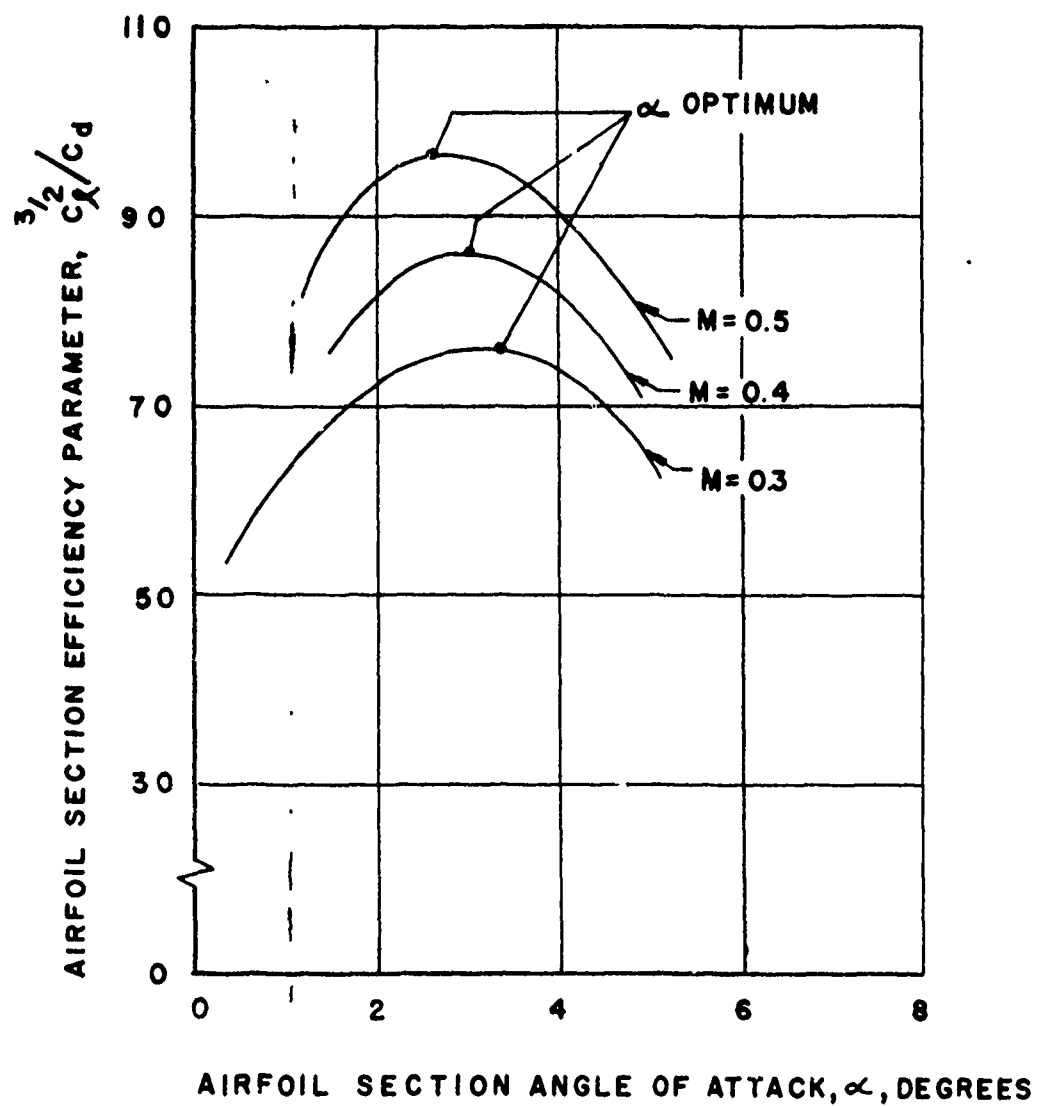
FIGURE 31:   AIRFOIL SECTION EFFICIENCY PARAMETER
FOR 16709 SERIES AIRFOIL

102
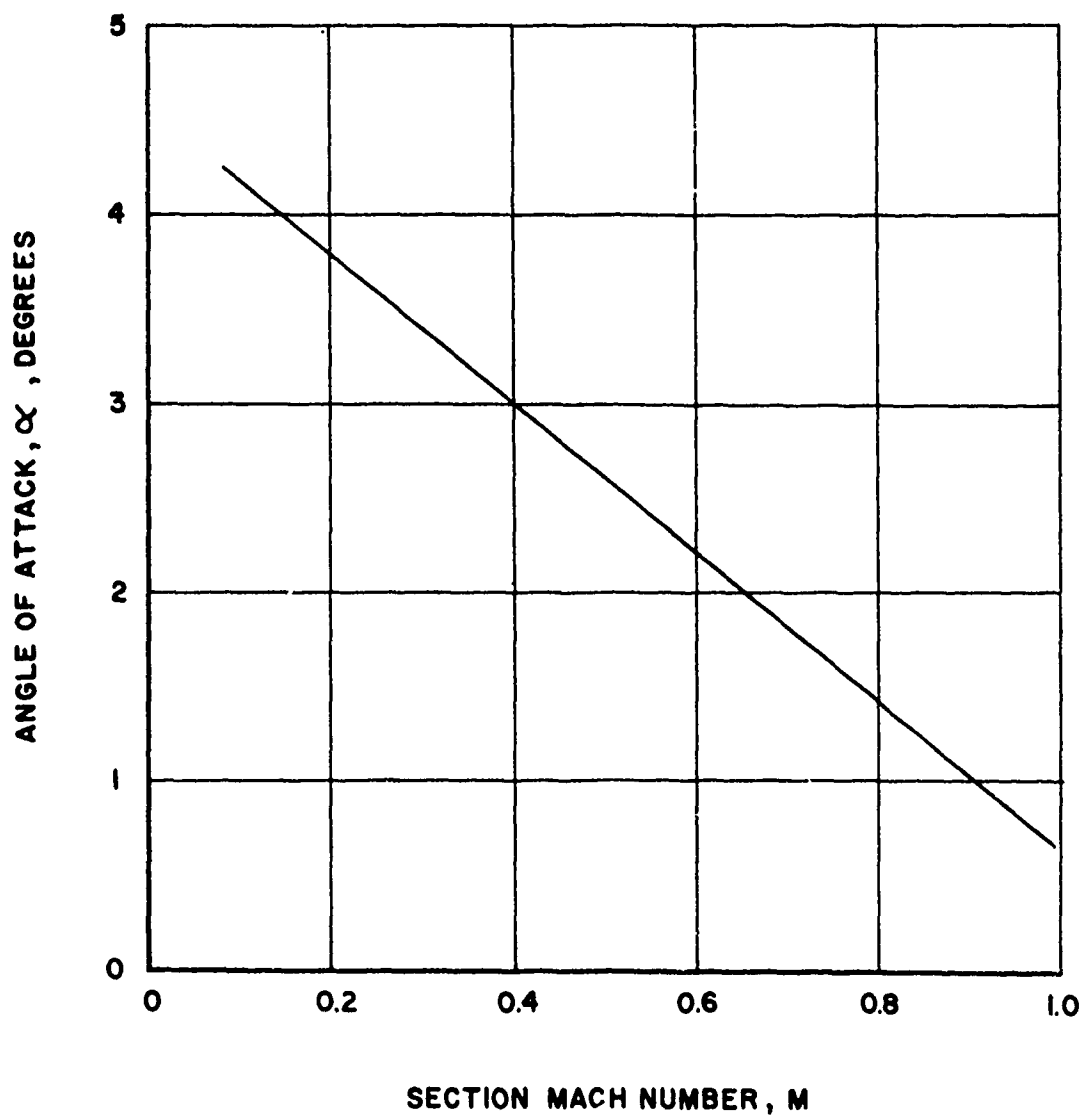
FIGURE 32: VARIATION OF THE OPTIMUM ANGLE OF ATTACK OF THE
16709 SERIES AIRFOIL WITH MACH NUMBER

103

DISTRIBUTION

Army War College	1
Aviation Test Office, Edwards AFB	1
U. S. Army Polar Research and Development Center	1
Deputy Chief of Staff for Logistics, D/A	1
The Research Analysis Corporation	1
Army Research Office, Durham	2
Office of Chief of R&D	2
Naval Air Test Center	1
Army Research Office, OCRD	1
Deputy Chief of Staff for Military Operations, D/A	1
U. S. Army Engineer Research & Development Laboratories	2
U. S. Army Tank-Automotive Center	2
U. S. Army Combat Developments Command, Transportation Agency	1
U. S. Army Aviation and Surface Materiel Command	19
U. S. Army Transportation School	4
U. S. Army Transportation Research Command	66
U. S. Army Airborne, Electronics and Special Warfare Board	1
U. S. Army Research & Development Group (Europe)	2
Chief of Naval Operations	1
Chief of Naval Research	3
Bureau of Naval Weapons	2
Bureau of Supplies and Accounts, D/N	1
U. S. Naval Supply Research and Development Facility	1
U. S. Naval Postgraduate School	1
Bureau of Ships	1
U. S. Naval Ordnance Test Station	1
David Taylor Model Basin	1
Marine Corps Landing Force Development Center	1
Marine Corps Educational Center	1
U. S. Army Standardization Group, Canada	1
Canadian Army Liaison Officer, U. S. Army Transportation School	3
British Army Staff, DAQMG (Mov & Tn)	4
U. S. Army Standardization Group, U. K.	1
Langley Research Center, NASA	2
Ames Research Center, NASA	2
Lewis Research Center, NASA	1

NASA Representative, Scientific and Technical Information Facility	1
U. S. Government Printing Office	1
Defense Documentation Center	10
U. S. Army Medical Research & Development Command	1
Human Resources Research Office	2
Office of the Asst. Sec. of Defense for R&E	1
U. S. Maritime Administration	1
Human Engineering Laboratory	1
U. S. Army Mobility Command	3
U. S. Strike Command	1
U. S. Army Materiel Command	6

Kellett Aircraft Corporation
Willow Grove, Pennsylvania
DETERMINATION OF OPTIMIZED PROPELL-
ERS FOR GROUND EFFECT MACHINES -
N. Miller, M. George, and R. Pruyn
Report 208A90-5, August 1963,
103 pp - illus - tables (Contract
DA44-177-TC-849) Task 1D021701A04813
TCREC Report 63-16.
Unclassified Report

Performance equations have been de-
veloped to predict the lift and the
power required for an arbitrary pro-
peller and Ground Effect Machine
(over)

Kellett Aircraft Corporation
Willow Grove, Pennsylvania
DETERMINATION OF OPTIMIZED PROPELL-
ERS FOR GROUND EFFECT MACHINES -
N. Miller, M. George and R. Pruyn
Report 208A90-5, August 1963,
103 pp - illus - tables (Contract
DA44-177-TC-849) Task 1D021701A04813
TCREC Report 63-16.
Unclassified Report

Performance equations have been de-
veloped to predict the lift and the
power required for an arbitrary pro-
peller and Ground Effect Machine
(over)

(GEM) combination when operating in close proximity to the ground. A method for determining an optimum propeller is presented. A test program was conducted to obtain data for comparison with the analyses. The effect of the ratio of the propeller area to the jet area on performance was also determined. An analysis of the loads and moments produced on a propeller when operating in a duct is presented.